2025

Advanced vibrational microscopy for clinical translation

BOSTON UNIVERSITY

COLLEGE OF ENGINEERING

Dissertation

ADVANCED VIBRATIONAL MICROSCOPY

FOR CLINICAL TRANSLATION

by

HONGLI NI

B.S., Zhejiang University, 2019

Submitted in partial fulfillment of the

requirements for the degree of

Doctor of Philosophy

2025

Approved by

First Reader

Ji-Xin Cheng, Ph.D.
Moustakas Chair Professor in Photonics and Optoelectronics
Professor of Electrical and Computer Engineering
Professor of Biomedical Engineering
Professor of Materials Science and Engineering
Professor of Chemistry
Professor of Physics

Second Reader

Darren Roblyer, Ph.D.
Associate Professor of Biomedical Engineering
Associate Professor of Electrical and Computer Engineering

Third Reader

Jerome C. Mertz, Ph.D.
Professor of Biomedical Engineering
Professor of Electrical and Computer Engineering
Professor of Physics

Fourth Reader

Siddharth Ramachandran, Ph.D.
Distinguished Professor of Engineering
Professor of Electrical and Computer Engineering
Professor of Physics
Professor of Materials Science and Engineering

DEDICATION

I would like to dedicate this work to my mother Aihua Dong.

ACKNOWLEDGMENTS

I would like to express my deepest appreciation to my advisor, Dr. Ji-Xin Cheng, for his guidance and support throughout my Ph.D. study. As a world-class scientist and an insightful mentor, Dr. Cheng has inspired me to strive excellence and set high standards for research. I am also deeply thankful to my committee members, Dr. Darren Roblyer, Dr. Jerome Mertz and Dr. Siddharth Ramachandran for their invaluable advice and support. Their help is indispensable for my dissertation work. I also want to thank Dr. Thomas Bifano, who collaborated with me on my first paper and served as committee member in my qualify exam. Dr. Bifano's encouragement gave me a lot of confidence to pursue my Ph.D. research.

I sincerely thank my colleagues, collaborators and everyone who has helped me during my Ph.D. journey. In particular, I am deeply grateful to my mentor Dr. Peng Lin, who introduced me into the field of vibrational imaging and taught me how to conduct research from every details. I would also appreciate our lab alumni Dr. Lu Lan, Dr. Yeran Bai, Dr. Puting Dong, Dr. Jie Hu, Dr. Yuying Tan, Dr. Jian Zhao, Dr. Le Wang, and Yuewei Zhan. They gave a lot of help to my work and career. I want to thank my labmates, who are brilliant colleagues and warm friends: Dr. Yuhao Yuan, Dr. Haonan Lin, Dr. Yifan Zhu, Dr. Jiaze Yin, Dr. Meng Zhang, Dr., Dr. Qing Xia, Chinmayee Prabhu Dessai, Mingsheng Li, Guo Chen, Guangrui Ding, Zhongyue Guo, Danchen Jia, and Dingcheng Sun. They worked together with me in the meantime brought me a lot of joy in the daily life. A special thank you goes to my closest labmate and best friend, Xiaowei Ge. She cheered me up in my most difficult time. I also want to acknowledge my collaborators Huate Li, Nicholas A. Vickers, Dr. Wei Wang and Dr. Shaoxiong Cheng, for their invaluable contributions to my research.

Finally, I wish to express my deepest appreciation to my family and my boyfriend. To my mother Aihua Dong, my father Weidong Ni and my sister Yinuo Ni, thank you for your everlasting love and support throughout my life. To my boyfriend, Jingan Zhou, thank you for always encouraging me and standing by my side in my important moments of this journey.

ADVANCED VIBRATIONAL MICROSCOPY

FOR CLINICAL TRANSLATION

HONGLI NI

Boston University College of Engineering, 2025

Major Professor: Ji-Xin Cheng, Ph.D., Moustakas Chair Professor in Photonics and Optoelectronics, Professor of Electrical and Computer Engineering, Professor of Biomedical Engineering, Professor of Materials Science and Engineering, Professor of Chemistry, Professor of Physics

ABSTRACT

The label-free chemical imaging capability of vibrational microscopy overcomes the limitations of fluorescence microscopy, which arise from the use of exogenous fluorescent dyes. Advanced vibrational microscopy techniques, including mid-infrared photothermal and coherent Raman scattering, have found broad applications in life sciences and demonstrated great potential for clinical applications. However, clinical translation of vibrational microscopy faces two remaining challenges: the lack of a universally-available, clinical-compatible imaging systems and the challenge of limited imaging depth.

My dissertation made three advances in instrumentation to address these challenges. In the first advance, we developed a clinically-compatible stimulated Raman microscope with a rapid widely-tunable fiber laser. By implementing auto-balanced detection, we improved the imaging signal-to-noise ratio by 23 times and achieved high-quality multi-window chemical imaging. The second advance provided biomarker information in stimulated Raman histology. Utilizing the rich chemical information in the hyperspectral stimulated Raman imaging, we demonstrated high-content mapping of tissue components in human breast cancer sections. With a spectral selective-sampling method, we improved the data

acquisition speed by 9 times. The last advance is to overcome the challenge of limited imaging depth. We invented the short-wave infrared photothermal microscopy (SWIP) to push vibrational imaging depth to millimeter scale for in-vivo measurements. By pumping the overtone transition of carbon–hydrogen bonds and probing the subsequent photothermal lens with shortwave infrared light, SWIP obtained chemical contrast from 1 μm polymer particles located at 800 μm depth in a highly scattering phantom. We further demonstrated that SWIP resolves intracellular lipids across an intact tumor spheroid and the layered structure in thick liver, skin, brain and breast tissues.

Together, my dissertation advances the clinical translation of vibrational microscopy by developing a clinical-compatible system, providing biomarker information, and pushing vibrational imaging depth to millimeter scale. We expect these advances to open new possibilities for a broad range of biomedical applications.

TABLE OF CONTENTS

LIST OF TABLES

LIST OF FIGURES

1. CHAPTER ONE – INTRODUCTION

1.1 Introduction to vibrational microscopy

Optical microscopy has been advancing clinics by facilitating the understanding of illness and health. Optical microscope allows direct observation of cell, which are the building block of the body. The initial brightfield optical microscope only visualizes cell morphology, which is not enough to understand the cell behavior. Fluorescence microscopy is developed to reveal the cellular activity by mapping biomolecule distribution with fluorescence labels. Fluorescence microscopy has become an indispensable tool for the life science, however, there are still several limitations of this technique. Firstly, exogeneous fluorescence labels are commonly toxic and not applicable to human body. Besides, fluorescence dye typically has large molecular weight. When tagging to small molecules, the fluorescence dye will perturb the natural molecular function. In addition, fluorescence labelling process is labor-intensive and time-consuming, which prevents fast analysis of the sample.

Vibrational microscopy can overcome these limitations of fluorescence microscopy with the label-free chemical imaging capability. Vibrational microscopy is based on probing the intrinsic molecular vibration, whose frequency is determined by the chemical bond composition and structure. By detecting signal at different vibrational frequencies, vibrational spectra can be acquired as the ‘fingerprints’ of the sample to map different biomolecules including lipid, protein, carbohydrate and nucleic acid. There are two major methods to probe the molecular vibration. The first method is to detect the mid-infrared absorption, which is established as a versatile molecular analysis tool in 1900s [1]. The representative modality in this category is Fourier transform infrared spectroscopy (FTIR) [2, 3]. While offering strong signal, FTIR has poor spatial resolution at several micrometers due to the long wavelength of infrared light. Besides, FTIR suffers from the strong water absorption and baseline artifacts due to the heterogeneity of the sample [4]. The other approach is based on the Raman scattering, which was discovered by C. V. Raman in 1920s [5]. Raman scattering is an inelastic scattering phenomenon, in which the incident photons change energy with the vibrating molecule. This energy change leads to a frequency shift equals to the vibration frequency in the scattered photon, where the red-shifted photon is called Stokes, and the blue-shifted photon is called anti-Stokes. Spontaneous Raman microscopy offers subcellular spatial resolution and avoids strong water absorption by using visible to near-infrared light source [6]. The major disadvantage of spontaneous Raman microscopy is the very weak signal which is orders of magnitude lower than the infrared-based methods and is vulnerable to the autofluorescence background. These factors result in a long pixel integration time of a few seconds [7], which is not applicable for real-time imaging live organisms.

1.2 Introduction to advanced vibrational microscopy

The emerging advanced vibrational microscopy techniques, mainly include coherent Raman scattering microscopy (CRS) and mid-infrared photothermal (MIP) microscopy [8], have been developed to address the issue of the conventional vibrational microscopes. Other recently-developed advanced vibrational microscopes including near-infrared photoacoustic microscope [9] and vibrational-resonant sum frequency generation [10, 11] can also solve the issues in certain aspects, but they are limited by the detection sensitivity and haven't found wide applications. In this section, I will focus on the introduction of CRS and MIP.

1.2.1 Coherent Raman Scattering (CRS) microscopy

CRS microscopy overcomes the speed limitation of spontaneous Raman microscopy and has significantly extended the scope of applications in the past two decades [8, 12]. CRS utilizes two synchronized ultrafast lasers, named pump at ω_p and Stokes at ω_S, to coherently drive the molecular vibration at the two lasers' beating frequency $\omega_p-\omega_S$. In this way, CRS can enhance the Raman signal by 10^6 times and achieve a pixel integration time in the order of microsecond.

CRS can be further divided into coherent anti-Stokes Raman scattering (CARS) and stimulated Raman scattering (SRS) (Figure 1.1(a)). CARS is a four-wave mixing process, where two input pump photons give rise to the generation of a Stokes output photon and an anti-Stokes photon at the frequency of $2\omega_p-\omega_S$. The generation of anti-Stokes photon is detected as the CARS signal. In SRS, the incident beams exchange energy with the molecules and the signal is manifested as the intensity loss at pump beam (stimulated Raman loss, SRL) and the intensity gain of Stokes (Stimulated Raman gain, SRG).

CARS and SRS has their own advantages and disadvantages. Because the CARS signal is generated at a higher optical frequency than the incident beams, the detection of CARS circumvents the influence of the incident beams and the autofluorescence. However, the CARS signal usually accompanied by a vibrationally non-resonant background (NRB) resulted from the electronic contribution in the nonlinear optical response. The NRB will distort the Raman spectra and cause difficulties in chemical analysis [13]. In the contrast, SRS is free of NRB and offers nearly identical spectral profiles as spontaneous Raman spectroscopy. SRS signal has a linear relationship to the molecule concentration, thus allowing quantitative measurement [14]. Furthermore, SRS is robust to the ambient light, which is preferable for clinical use. Nevertheless, SRS suffers from the cross-phase modulation (XPM) background, which is caused by the Kerr effect [15]. By fully collecting the light transmitted from the sample with high numerical aperture (NA) condenser, XPM can be effectively suppressed. But such collection can hardly be achieved for the back-scattered light, making SRS not suitable for epi-detection.

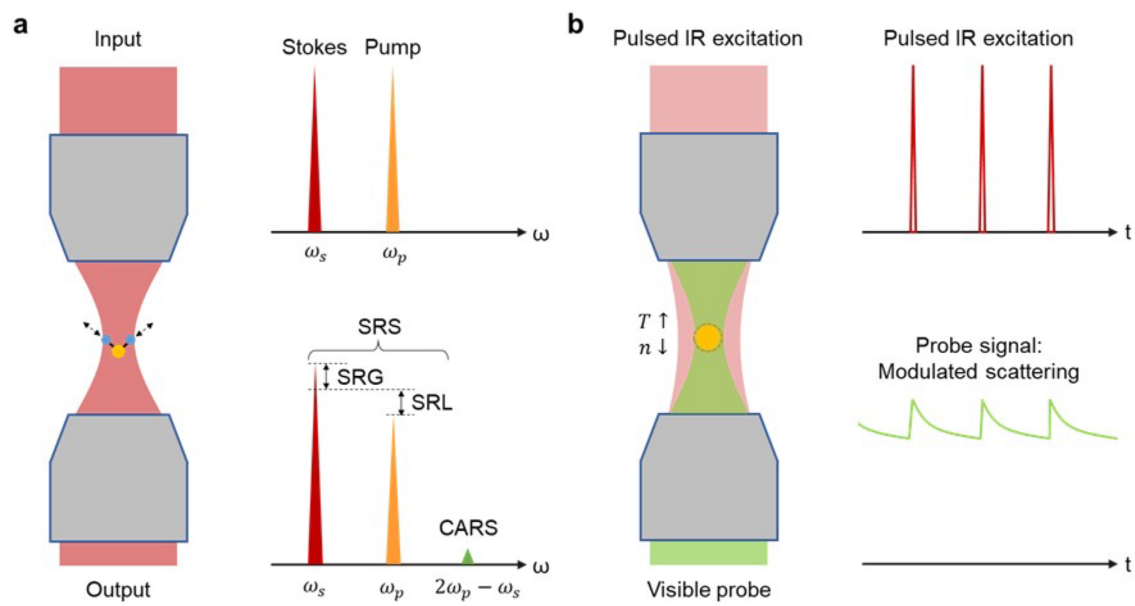

Figure 1.1: Principle of coherent Raman scattering microscopy and mid-infrared photothermal microscopy.

(a) Principle of coherent Raman scattering microscopy. SRS: Stimulated Raman scattering. SRG: Stimulated Raman gain. SRL: Stimulated Raman loss. CARS: Coherent anti-Stokes Raman scattering (b) Principle of mid-infrared photothermal microscopy. IR: Infrared.

1.2.2 Mid-infrared Photothermal (MIP) microscopy

MIP is developed to overcome the limitations of traditional infrared imaging techniques on the spatial resolution and water absorption [16]. MIP breaks the resolution limit of infrared light and achieves sub-micrometer resolution by introducing a visible probe beam to sense the infrared absorption-induced photothermal effect. This detection scheme also alleviates the influence of water absorption because water has a weak photothermal signal. With these advantages, MIP allows subcellular-resolution mid-infrared imaging of living cells, which is impossible with traditional infrared imaging techniques.

A schematic of MIP detection principle is shown in Figure 1.1(b). The pulsed infrared laser will induce a periodic local temperature rise on the sample through the infrared absorption. The temperature rise will then lead to a refractive index change on the sample through the thermos-optic process. The refractive index change will modulate the scattering of the probe beam, which is detected as the MIP signal.

The key advantage of MIP is the high detection sensitivity, which is at sub-micromolar level [17] compared to sub-millimolar level sensitivity of CRS [18]. In the meantime, the scattering-based photothermal detection is intrinsically sensitive to small particles. These characteristics make MIP an excellent tool for imaging small subcellular organelle and domains [19], bacteria [20], and virus [21]. The major disadvantage of MIP comes from the strong water absorption in the mid-infrared region. This strong water absorption causes water background in the MIP images and limits the penetration depth of MIP within tens of micrometers.

1.3 Clinical translation of advanced vibrational microscopy and the challenges

Because of the high-speed, high-sensitivity chemical imaging capability, CRS and MIP have found broad applications in life sciences and showed great potential in clinical translation [12, 22, 23]. Many works have been done to integrate these methods into clinical workflow. CRS has obtained promising results in tissue histology [24-27], flow cytometry [28-32], antibiotic susceptibility test [33, 34], monitoring drug delivery into skin [35-37]. Besides, CRS endoscope and handheld device were developed for in-situ applications [38, 39]. As a relatively new technique, MIP just started exploration in clinical translation. MIP has been successfully demonstrated in tissue histology [40], antibiotic susceptibility test [41] and virus analysis [21, 42].

Although CRS and MIP have demonstrated great performance in many clinical applications, there are remaining challenges hinder their broader adoption in clinic. The first obstacle is the lack of a universally-available, clinical-compatible system. There are fiber laser-based CRS systems developed for the clinical environment [43-45], however, the fiber lasers used in these systems are highly customized and only available in a few research groups. Besides, these reported fiber laser-based CRS systems have either a narrow spectral bandwidth or slow spectral tuning speed, therefore are not suitable to acquire biomarker information. The second challenge is the limited imaging depth. CRS has a maximum imaging depth of around 100 µm, which is mainly limited by the tissue scattering. MIP has a penetration depth of tens of micrometers due to water absorption. This limited imaging depth only allows interrogating the surface of the sample, which not meet the need of many in-vivo and in-situ applications. For example, human epidermis is around 100 μm thick, so a maximum imaging depth of 100 μm cannot penetrate through the epidermis to see the pigments, glands, nerves and vessels which are closely related to many diseases.

My dissertation aims to address the abovementioned challenges by developing new advanced vibrational microscopy techniques. In chapter two, we developed a clinical-compatible SRS system by integrating a commercially available fiber laser with broad spectral bandwidth. Utilizing an auto-balanced detection scheme, we suppressed the laser noise and obtained high-quality imaging results. In chapter three, we introduced biomarker information into stimulated Raman histology. With spectral unmixing algorithm and broadband spectral coverage, we demonstrated high-content mapping of tissue components in human breast cancer. In chapter three, we addressed the challenge of the limited imaging depth by inventing a new modality called shortwave infrared photothermal microscopy, which bridged the gap for micron-resolution millimeter-deep chemical imaging.

2 CHAPTER TWO – FIBER LASER-BASED STIMULATED RAMAN SCATTERING MICROSCOPY

The work in this chapter was published in Analytical Chemistry [46]. Reprinted with permission from American Chemical Society Publications. This work was co-led by Dr. Peng Lin. I contributed to system development, data acquisition and analysis, manuscript writing.

Spectroscopic stimulated Raman scattering (SRS) imaging has become a useful tool finding a broad range of applications. Yet, wider adoption is hindered by the bulky and environmentally-sensitive solid-state optical parametric oscillator (OPO) in current SRS microscope. Moreover, chemically-informative multi-window SRS imaging across carbon-hydrogen (C-H), carbon-deuterium (C-D) and fingerprint Raman regions is challenging due to the slow wavelength tuning speed of the solid-state OPO. In this work, we present a multi-window SRS imaging system based on a compact and robust fiber laser with rapid and widely tuning capability. To address the relative intensity noise intrinsic to fiber laser, we implemented auto-balanced detection which enhances the signal-to-noise ratio of stimulated Raman loss imaging by 23 times. We demonstrate high-quality SRS metabolic imaging of fungi, cancer cells, and Caenorhabditis elegans across the C-H, C-D and fingerprint Raman windows. Our results showcase the potential of the compact multi-window SRS system for a broad range of applications.

2.1 Introduction

SRS microscopy is an increasingly useful tool in various biomedical and clinical research [22, 34, 47-50]. However, broader adoption of this technique is challenged by the routinely-used solid-state optical parametric oscillator (OPO) laser due to its bulkiness and strict requirement for the operating environment. Furthermore, the slow wavelength tuning speed of solid-state OPO hinders multi-window SRS imaging, i.e., spectroscopic SRS imaging across multiple Raman windows including C-H, C-D and fingerprint region.

Current spectroscopic SRS imaging methods can be categorized into two groups according to the bandwidth of the laser pulse. The first category uses narrowband picosecond pulses and generates a spectrum by tuning the laser wavelength, where high-throughput imaging is limited by the slow wavelength tuning of the solid-state OPO [49-51]. The second category uses broadband femtosecond laser and harnesses spectral focusing [52-54] or other pulse shaping [31, 55, 56] techniques for hyperspectral imaging within the bandwidth of the laser pulses. Such approaches enable high speed spectroscopic imaging within a limited spectral window, typically less than 300 cm^{-1} when using 100 fs pulses. Multi-window imaging has to rely on tuning the solid-state OPO, which is slow and suffers from laser pointing drift.

To overcome the limitations of the solid-state OPO, fiber lasers have gained increasing interest in SRS microscopy for its compactness and robustness. Many dual-output fiber lasers have been developed and deployed for SRS imaging, including synchronized fiber laser and Ti:sapphire laser [57, 58], electronically synchronized fiber lasers [59], self-synchronized fiber lasers [60], supercontinuum generation [43, 61], soliton frequency self-shifting [62], Fourier domain mode-locking [44], and parametric frequency generation [45]. Nevertheless, the above-mentioned fiber laser sources either have limited spectral coverage or low power spectral density, which are not suitable for multi-window spectroscopic SRS imaging.

Recently, Brinkmann *et al* developed a rapid widely tunable picosecond fiber laser based on a fiber-OPO (FOPO) and deployed this laser for CARS imaging [63, 64]. By engineering the dispersion and nonlinearity of the fiber, the FOPO enables broad spectral tuning which covers C-H, C-D and fingerprint region. Through incorporating a chirped fiber Bragg grating to match the repetition rate of the two outputs automatically, this FOPO achieves a spectral tuning speed of 5 ms between arbitrary wavenumbers, which is beyond the reach by other fiber lasers used for coherent Raman microscopy.

In this chapter, we demonstrate SRS imaging of cells and organisms with the rapid widely tunable FOPO. As mentioned above, SRS is advantageous over CARS for the lack of non-resonant background, signal linearity and robustness under ambient light. However, fiber laser-based SRS imaging is challenging due to the intrinsic high laser relative intensity noise (RIN). We therefore analyzed the noise spectrum of the fiber laser and optimized the modulation frequency for SRG imaging. Next, we implemented auto-balanced detection (ABD) on the FOPO output, which improves the signal-to-noise ratio (SNR) by 23 times for SRL imaging. Subsequently, we demonstrated SRL imaging of biological specimens cross the C-H, C-D and fingerprint regions. In the C-H region, we mapped the lipid and protein distribution inside fungi and ovarian cancer cells. Through cross-window analysis of the C-D and C-H region, we visualized the metabolic activity of fungi and lipid uptake of ovarian cancer cells. Combining the fingerprint and C-H region images, we analyzed the unsaturated lipid, cholesterol and overall lipid content of the *Caenorhabditis elegans* (*C. elegans*). Collectively, the results demonstrate the potential of our multi-window SRS microscope for a wide range of applications.

2.2 Methods

2.2.1 Multi-window SRS imaging system

Figure 2.1 (a) shows the schematic. The fiber laser (PICUS DUO, Refined Laser Systems GmbH) generates two synchronized pulse trains through the FOPO and an ytterbium-doped fiber oscillator. The pulses from the FOPO serves as the pump and the pulses from the fiber oscillator serves as the Stokes for SRS imaging. The laser repetition rate is 40.5 MHz and the pulse duration is ~7 ps. The spectral tuning range is from 1050 cm^{-1} to 3150 cm^{-1}, corresponding to pump wavelength from ~946 nm to 775 nm and Stokes wavelength from ~1053 nm to 1027 nm. The spectral resolution is about 12 cm^{-1}. The timing of the two beams varies for different Raman windows. To ensure the temporal overlapping of the pump and Stokes pulses, a motorized stage (X-LSM025A-KX14A, Zaber technology) is used to compensate the timing change for every 300 cm^{-1}.

The pump and Stokes beams first pass a half-wave plate (HWP) and a polarization beam splitter (PBS) for power adjustment and polarization parallelization. In the pump path, a 750 nm longpass filter is put after the PBS to filter out possible stray light. Both beams are pre-expanded to around 2 mm in diameter by a 4-f system. Between the 4f lens pair, an acousto-optic modulator (AOM) (1205-C, Isomet) is set near the beam focus to modulate the laser beam. For SRG, the pump is modulated and for SRL the Stokes. The pump and

Stokes beams are spatially combined on the dichroic mirror. The combined beams then pass a pair of galvo mirrors for laser X-Y scanning. A 4-f system is between the galvo mirror and the objective to expand the laser beam to around 6 mm in diameter and conjugate the galvo mirror with the objective back aperture. The spatio-temporally overlapped pump and Stokes beams are focused onto the sample by a water-immersion objective with 1.2 numerical aperture (NA) (UPLSAPO60XW, Olympus). A piezo positioner is installed on the objective to enable axial scanning. The outgoing light is collected by an oil immersion condenser with 1.4 NA (U-TLO, Olympus). The collected light passes a spectral filter to filter out the AOM-modulated beam. For SRL we used a 1000 nm shortpass filter (FESH1000, Thorlabs) and for SRG we used a 1000 nm longpass filter (FESH1000, Thorlabs).

The filtered light is detected by a home-built detector (Fig 2.1 (b)). The light signal is transformed to photocurrent by a large area 62 V-biased photodiode (DET100A2, Thorlabs). The photocurrent is then turned to voltage signal after passing a 50 Ω impedance. The AC and DC components of the signal is separated by a bias tee (ZFBT-282-1.5A+, Mini-circuits). The separated DC is sent out as the DC output. The AC part is pre-filtered by 1.2 MHz highpass (ZFHP-1R2-S+, Mini-circuits) and 22 MHz lowpass filter (BLP-21.4+, Mini-circuits) then amplified by a low-noise voltage amplifier (SA-230F5, Wayne Kerr Electronics). The amplified AC signal is the AC output of the detector. When imaging without the ABD, this AC output is directly demodulated by a lock-in amplifier (HF2LI, Zurich Instrument) to extract the SRS signal.

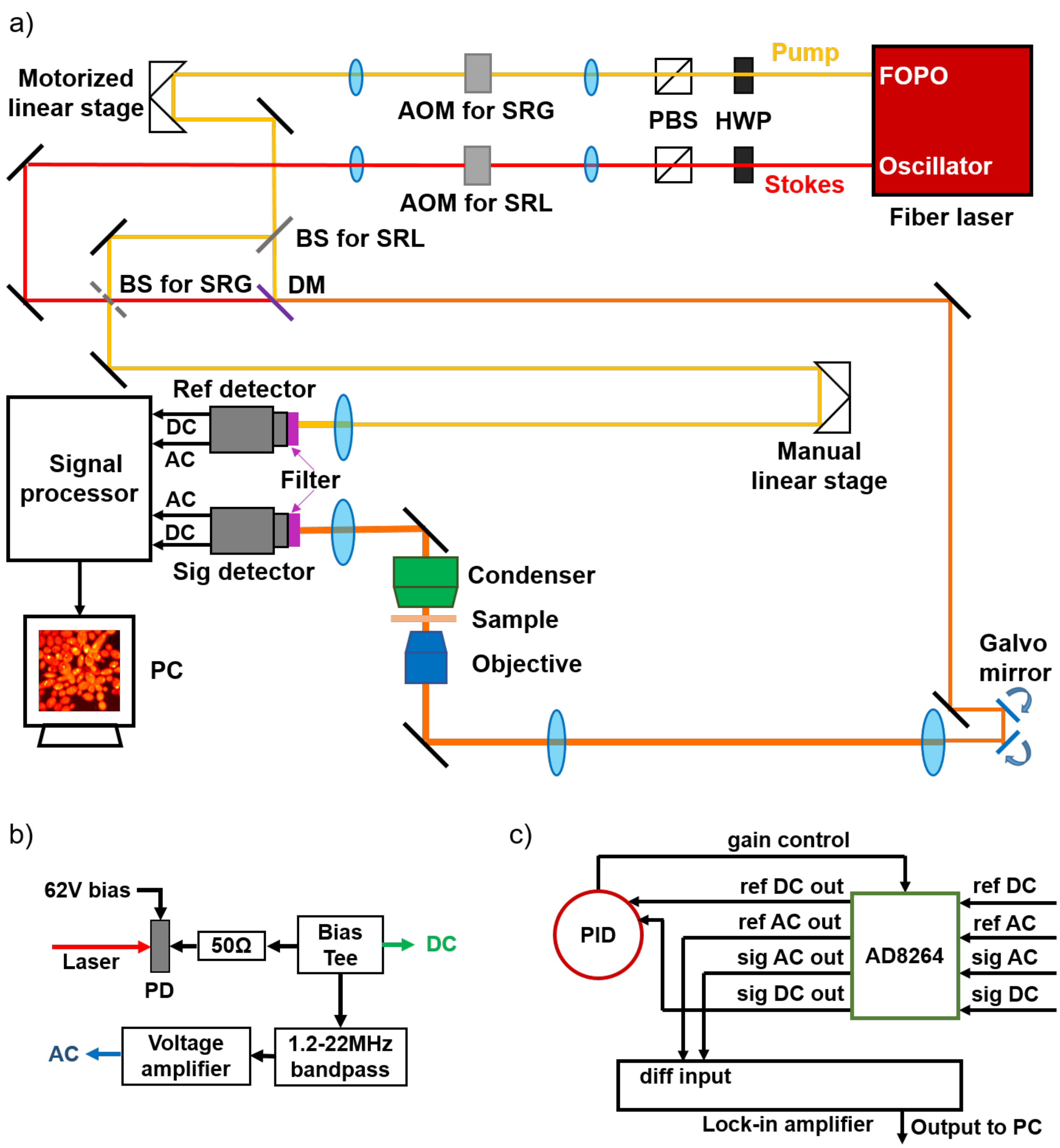

Figure 2.1: A rapid, widely tuning SRS microscope.

(a) Schematic. HWP: Half-wave plate. PBS: Polarization beam splitter. AOM: Acousto-optic modulator. BS: Beam splitter. DM: Dichroic mirror. Ref: Reference. Sig: Signal. (b) Schematic of the detector assembly. PD: Photodiode c) Workflow inside the signal processor for auto-balanced detection. PID: proportional–integral–derivative controller.

2.2.2 Auto-balanced detection

In balanced detection, the noisy laser beam is split into a signal and a reference arm. The signal arm interacts with the sample and the reference arm does not. The laser noise is canceled by taking the difference of the electrical signal from the two arms. The electrical signal from the two arms is carefully balanced in phase and amplitude to obtain the best noise cancellation performance. Compared to the optical delay-based [59] or polarization-based [65, 66] method, ABD requires no special optics as well as fine optical alignment. ABD utilizes a proportional–integral–derivative (PID) controller to balance the signal amplitude of the two arms, making it robust for sample transmission variation [43, 55].

To implement auto-balanced SRS, several components are added into the system (Figure 2.1 (a)). A beam splitter (BS) (BSS11R, Thorlabs) is put into the light path to split the unmodulated beam into 2 arms. The two arms are detected by identical detectors as illustrated in Figure 2.1 (b). The detector for the signal arm is denoted as sig detector and the one for the reference arm is denoted as ref detector. The phase of the AC signal from the two arms is matched by adjusting the manual linear stage in the reference arm. The AC amplitude is balanced with the auto-balancing signal processor shown in Figure 2.1 (c). In the signal processor, the AC and DC outputs from the two detectors are sent to a 4-channel variable gain amplifier (AD8264, Analog Devices Inc.). The function of AD8264 is to amplify the signals with adjustable gain. To balance the AC amplitude, the gain for the two arms is controlled by a PID controller (Moku:Lab, Liquid Instruments). The PID determines the gain according to the DC signal from the two arms.

2.2.3 Sample preparation

The fungal strain, C. albicans SC5314 (wild type), used in this study was from American Type Culture Collection (ATCC). *C. albicans* cells were grown overnight in yeast extract peptone dextrose (YPD) at 30 °C in an incubating shaker to reach stationary phase. The stationary-phase fungal cells were then diluted by 20 times in fresh YPD and cultured for another 5 hours at 30°C to obtain the log-phase cells. After that, fungal specimens were pelleted and washed with 1×PBS. The log-phase *C. albicans* cells were resuspended in 0% and 90% D_2O containing YPD for D_2O treated group and control group at a concentration of 1×10^7 cells/mL and incubated for 2 hours. Then, 1 mL of fungi solution was centrifuged, washed with 1×PBS, and fixed by 10% formalin solution. Before imaging, formalin solution was washed away by 1×PBS.

The ovarian cancer cells OVCAR5 were provided by Daniela Matei lab at Northwestern University and were cultured in RPMI 1640 medium (Gibco) supplemented with 10% FBS, 1% P/S and 2 mM GlutaMax (Gibco). Cells were seeded in 35 mm glass-bottom dishes (Cellvis) overnight and were fixed with 10% neutral buffered formalin for 30 min followed by 3 times PBS wash before imaging. For oleic acid-d34 labeling, cells were cultured with 100μM oleic acid-d34 (Cambridge Isotope Lab) for 6 hours after overnight seeding in the glass-bottom dishes. All cells were maintained at 37 °C in a humidified incubator with 5% CO2 supply.

The *C. elegans* strains were obtained from the Caenorhabditis Genetics Center: wild-type (N2), VC452 [chup-1(gk245)]. The *C. elegans* was grown on standard NGM plates (containing 5 mg/L cholesterol) with *E. coli* OP50 at 20 °C for 2-3 days. Before SRS imaging, the *C. elegans* was anesthetized using 1% sodium azide and sealed between two coverslips.

2.3 Results

2.3.1 Laser noise measurement and stimulated Raman gain imaging performance

We measured the RIN spectra of the fiber oscillator and the FOPO outputs using the setup sketched in Figure 2.2 (a). The detector used for RIN measurement is the same as the one described in section 2.2.1. The AC output is sent to a spectrum analyzer (USB-SA44B, Signal Hound) to obtain the noise spectrum $S(f)$. The unit for $S(f)$ is dBm, which is a power unit. The value of $S(f)$ is influenced by the noise equivalent bandwidth (NBW), the signal amplification gain G_{AC} and the laser power on detector. To better compare the noise level, the noise is normalized to get the RIN spectrum [67]. We used the equation (1) to calculate RIN spectrum. The V_{DC} is the voltage of the detector DC output and is measured by a voltmeter. The $\frac{V_{DC}^2}{R}$ is the DC power, which represents the influence of average laser power on detector.

$$RIN = \frac{S(f)}{NBW * G_{AC} * \frac{V_{DC}^2}{R}} \tag{1}$$

Figure 2.2 (b) gives the laser RIN result with unit dBc/Hz. A RIN spectrum measured from a solid-state OPO (InsightX3, Spectra-Physics) is plotted as a reference. The RIN result indicates that the FOPO output is much noisier than the oscillator output. Therefore, we first performed SRG imaging to avoid the large laser noise in the FOPO output. We also noticed that the oscillator output has lower noise in higher frequency, suggesting that the modulation frequency (MF) can be increased to reduce the noise level in SRG imaging.

Figure 2.2 (c) shows the SRG images of 3 μm PMMA beads. We defined the SNR of a SRS image by equation (2), where the signal mean is measured from the area with strong SRS signal and the noise standard deviation (std) is measured from the background.

$$SNR = \frac{Signal\ mean}{noise\ std} \tag{2}$$

The SNR of an image with 6MHz MF is 2 times of that with 1.5 MHz MF, matching with the RIN spectrum in Figure 2.2 (b). Due to the limited AOM bandwidth, the modulation waveform deteriorates as the MF increases, resulting in SRS signal level drop in the higher MF. The sweet point for the SNR is around 6MHz.

Yet, the optimized SRG modality is not enough for cellular imaging at the C-D and fingerprint regions. Fig 2.2(d) shows the SRG images of D_2O treated fungal cells with 6 MHz MF at 2935 cm^{-1} (C-H region) and 2150 cm^{-1} (C-D region). The C-H region image barely shows the cell morphology. At the C-D region, the SNR is too low to show any contrast.

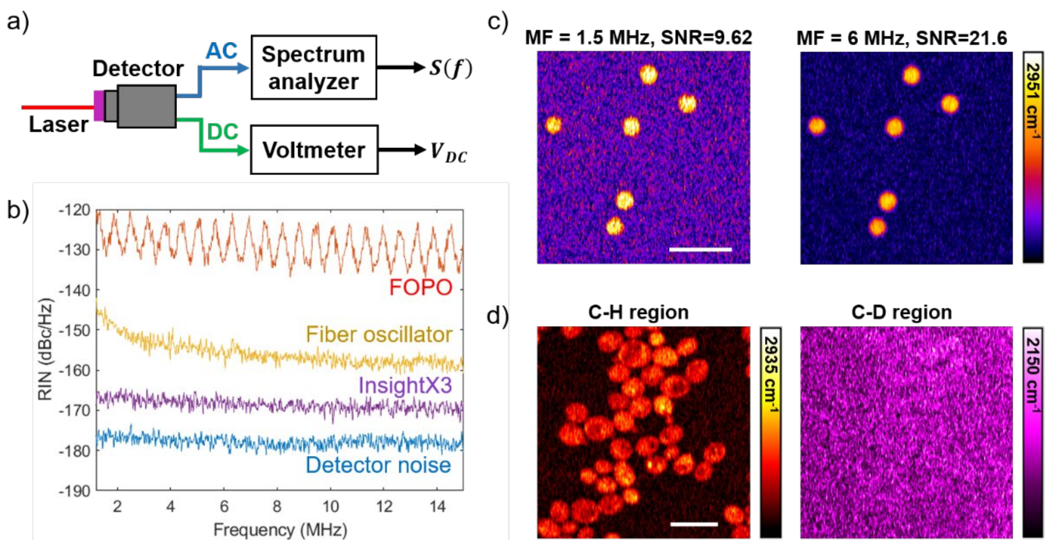

Figure 2.2: Laser noise measurement and SRG imaging result.

(a) Laser RIN measurement setup. (b) Laser RIN measurement result. Laser power on detector: ~20mW. (c) SRG imaging of 3 µm PMMA beads. MF: modulation frequency. Power on sample: Pump: 24 mW, Stokes: 22 mW. Dwell time: 10 µs. (d) SRG imaging of D_2O treated fungi at 2935 cm^{-1} (C-H region) and 2150 cm^{-1} (C-D region). Power on sample: C-H: Pump: 18 mW, Stokes: 43 mW. C-D: Pump: 30 mW, Stokes: 40 mW. Dwell time: 100 µs. MF: 6MHz. Scale bar: 10 µm.

2.3.2 Auto-balanced SRS imaging performance

To further improve the SNR, we implemented the ABD to cancel the laser intensity noise. Figure 2.3 (a) shows the oscillator noise spectrum before and after ABD, measured by the lock-in oscilloscope function. Figure 2.3 (c) shows the FOPO noise spectrum before and after ABD. With 10 mW laser power on the detector, ABD suppressed the oscillator noise by ~4 dB and the FOPO noise by ~26 dB at 3.3 MHz (Figure 2.3 (a) and (c)). This noise reduction led to SRG SNR improvement by 1.59 times and SRL SNR improvement by 20 times. Figure 2.3 (b) and (d) compares the SRS imaging result of 3 µm PMMA beads with and without ABD. The modulation frequency of 3.3 MHz was chosen to avoid too much signal level drop caused by the modulation deterioration. The SNR of the SRG image is improved by ~1.58 times and that of the SRL image is improved by ~23 times. The SNR improvement is more significant for SRL as the FOPO output is much noisier than the oscillator output. The auto-balanced SRL achieves better SNR than the auto-balanced SRG, mainly because the oscillator output has higher power than the FOPO output.

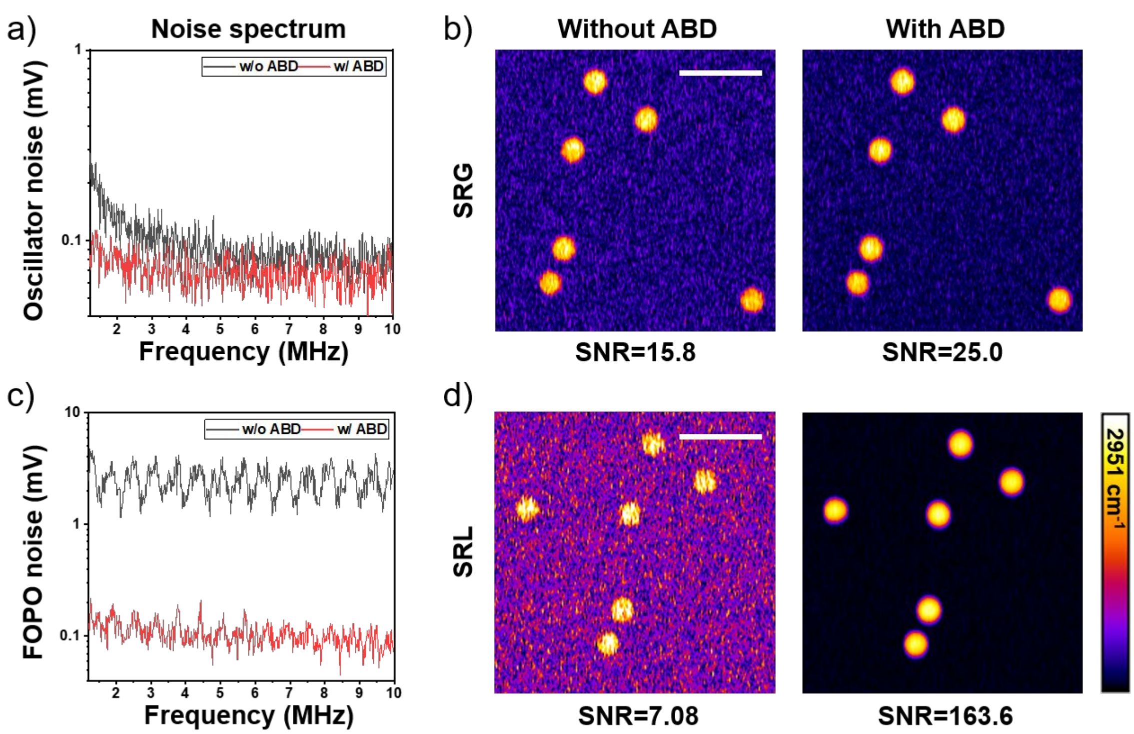

Figure 2.3: Auto-balanced detection (ABD) for improving SNR of SRS imaging.

(a) Oscillator noise spectrum with and without ABD. Power on PD: 11 mW. (b) SRG imaging of 3 μm PMMA beads at 2951 cm^{-1} captured with and without ABD. Power on sample: Pump: 18 mW, Stokes: 22 mW. (c) FOPO noise spectrum with and without ABD. Power on PD: 10 mW. (d) SRL imaging of 3 μm PMMA beads at 2951 cm^{-1} captured with and without ABD. Power on sample: Pump: 16 mW, Stokes: 99 mW. Dwell time: 10 μs. Scale bar: 10 μm.

With the auto-balanced SRL, we characterized the spectral fidelity, detection sensitivity, and excitation volume. Figure 2.4 (a) shows SRL spectra of several standard samples in C-H, C-D and fingerprint regions. The overall shape of the SRL spectra matches well the spontaneous Raman data (Figure 2.4 (a) dash line). The spectra in Figure 2.4 (a) were post-processed to remove artificial sharp dips caused by the laser imperfections (Figure 2.5 (a)). The post-processing procedure manually deletes the bad data points and then smooths the spectra using moving average with a window of 5 data points (Figure 2.5 (c)). Because the raw SRL spectra were sampled with 1 cm^{-1} step, which is much smaller than the spectral resolution, the resolution of the SRL spectrum should not be affected by the post-processing. Figure 2.4 (b) presents the detection sensitivity of DMSO at 2912 cm^{-1}. The detection sensitivity is found to be better than 0.02 mol/L. Figure 2.4 (c) and (d) depicts the transverse and longitudinal view of 3D SRL imaging of a 500 nm PMMA bead. The intensity profiles along the lateral and axial direction are shown in Figure 2.4 (e) and (f). The system axial resolution is around 2.47 μm and the lateral resolution is estimated to be 392 nm after deconvolution with particle size.

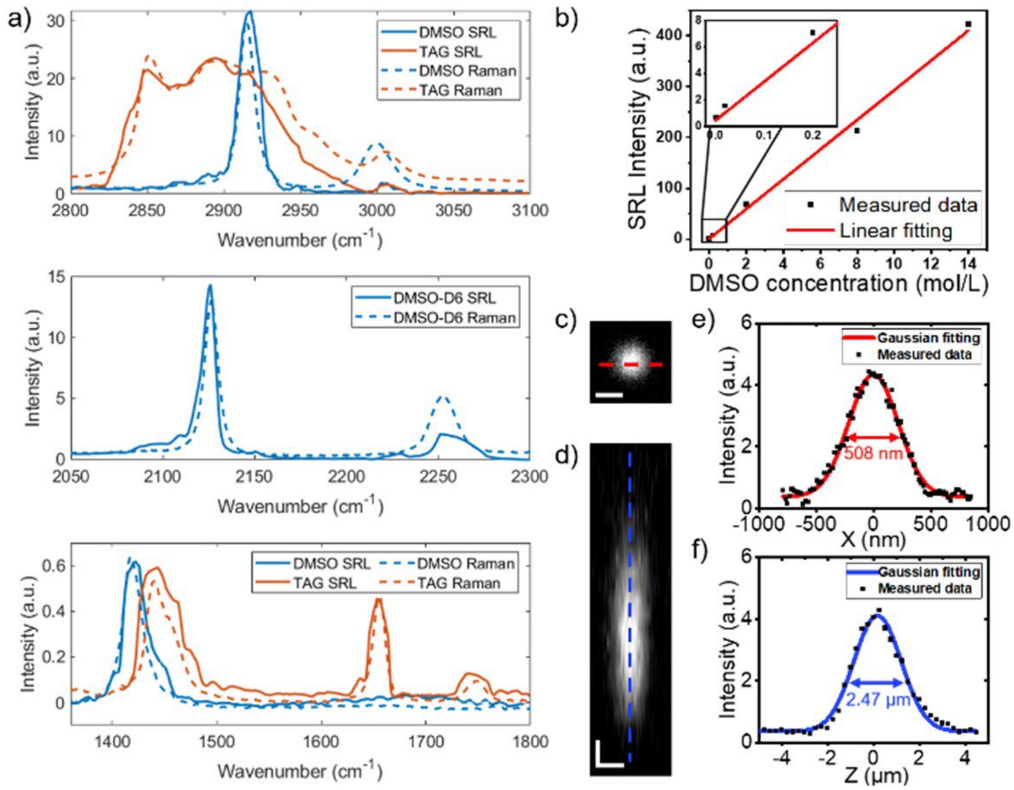

Figure 2.4: Characteristics of auto-balanced SRL.

(a) SRL spectra of representative samples in C-H, C-D, and fingerprint vibration regions. Spectrum acquisition time: ~5 s (C-H and C-D, 301 data points, integrated over 30×30 pixel area), ~7 s (Fingerprint, 441 datapoints, integrated over 30×30 pixel area) (b) DMSO detection sensitivity. (c) Transverse view of 3D SRL imaging of a 500-nm PMMA bead. (d) Longitudinal view of 3D SRL imaging of a 500-nm PMMA bead. (e) Intensity profile along the red line in (c). (f) Intensity profile along the blue line in (d). Power on sample: pump: 15 mW, Stokes: 90 mW. Dwell time: 100µs. Scale bar: 500 nm.

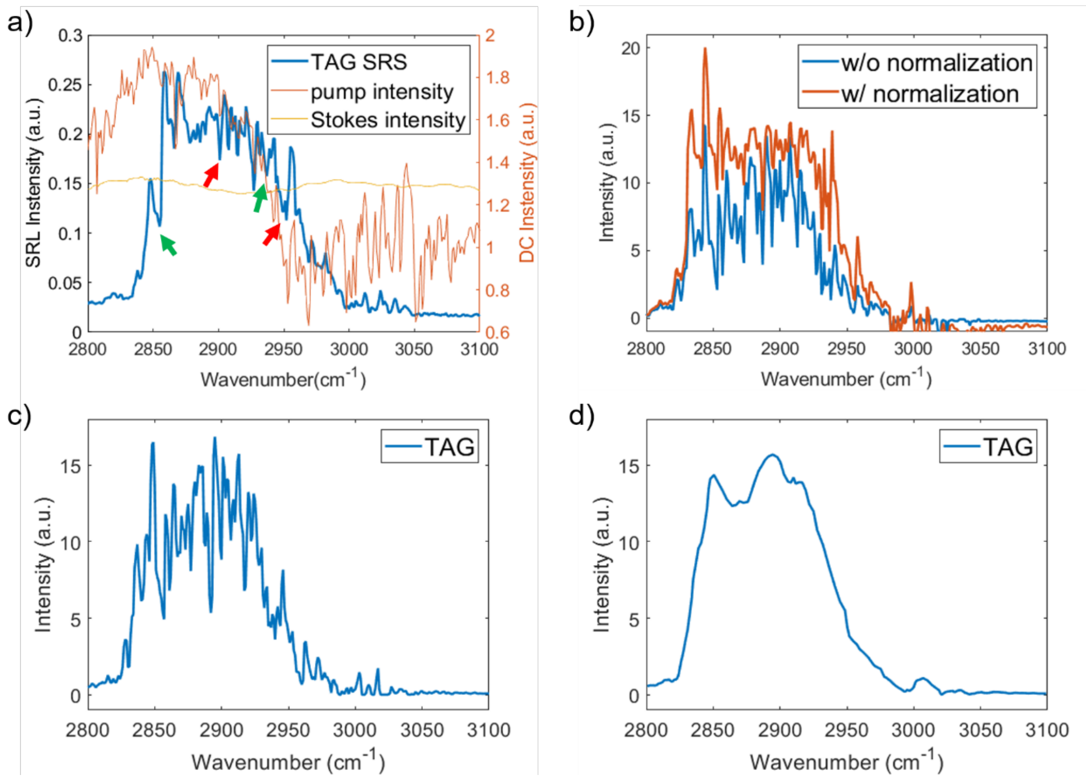

Figure 2.5: Sharp dips in SRS spectra caused by FOPO instability.

(a) Comparison between TAG SRS spectrum and laser intensity. Some sharp dips in the SRS spectrum show correlation with the pump intensity (red arrows). Some other dips are not correlated with the pump intensity (green arrows). (b) Raw TAG SRS spectrum and TAG SRS spectrum normalized by pump intensity. The normalization did not solve the artifacts issue due to multiple factors collectively causing the problem. (c) Raw TAG SRS spectrum. (d) Spectrum in (c) after deleting bad data points and smoothing with average mean with window of 5. TAG: triacylglycerol.

2.3.3 Multi-window SRL imaging of biological samples

To evaluate the imaging performance in the C-H region, we first recorded the SRL spectra of bovine serum albumin (BSA) and triacylglyceride (TAG), as shown in Figure 2.6 (a). We applied the same post-processing method to remove the artificial sharp dips in the SRL spectra as mentioned above. Next, we took hyperspectral image stacks of fungi and ovarian cancer cells from 2800 to 3100 cm^{-1} with 1 cm^{-1} step size. The spectra at every pixel are processed in the same way as the BSA and TAG spectra. The average results of the hyperspectral stacks are shown in the spectral projection column in Figure 2.6 (b) and (c). By applying the LASSO spectral unmixing algorithm [52] and taking the BSA and TAG spectra as protein and lipid spectra reference, maps of protein and lipid distribution in the cells are obtained from the hyperspectral data, as shown in Figure 2.6 (c) and (d). The lipids are located in the cytoplasm, while the protein signals were found in both nucleus and cytoplasm.

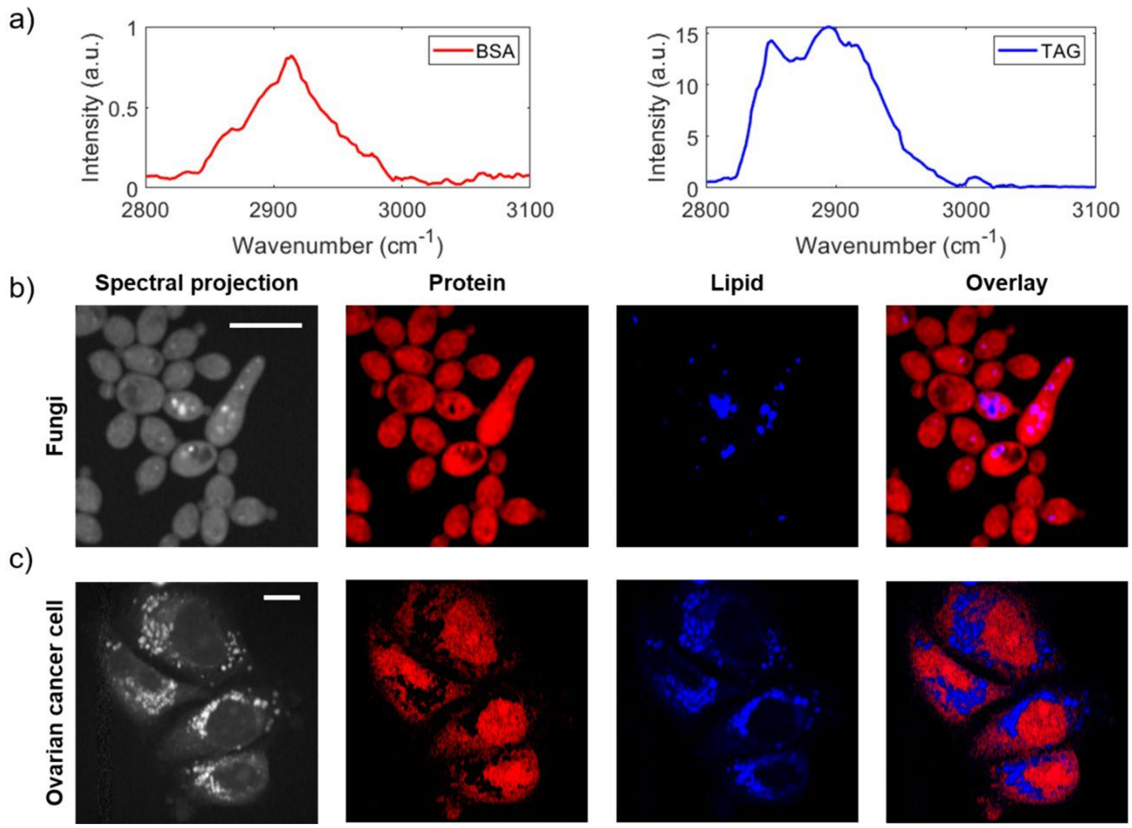

Figure 2.6: SRL imaging of cells in the C-H region.

(a) Standard sample spectra used for LASSO. Spectrum acquisition time: ~5 s (301 data points, integrated over 30×30 pixel area) (b) Hyperspectral stack projection and spectral unmixing result of fungal cells. (c) Hyperspectral stack projection and spectral unmixing result of ovarian cancer cells. Power on sample: Pump: 16 mW, Stokes: 98 mW. Dwell time: 10 µs. Scale bar 10 µm.

Tracking the uptake of deuterium-labeled nutrients using SRS imaging is an important tool for cell metabolism study [34, 49]. When deuterium-labeled nutrients are incorporated into the biomass, part of the C-H bonds in the cell molecules is replaced by the C-D bond, which gives signature Raman peaks in the C-D region. The SRS signal ratio of $I_{C\text{-}D}/(I_{C\text{-}D}+I_{C\text{-}H})$ therefore reflects the activeness of cell metabolism [68]. Due to the slow speed in switching between C-D region and C-H region, most of the published SRS studies only used the C-D intensity to represent cell activity [34, 49]. Yet, the C-D SRS intensity can be influenced by laser intensity, focus drifting, system alignment etc., thus not robust enough to quantify the cell metabolism. Here, multi-window SRS imaging addresses this issue with the capability of rapidly switching between the C-D and C-H vibrations. C-D/C-H SRL imaging of deuterium-labeled fungi and ovarian cancer cells are shown in Figure 2.7 (a)-(d). The D_2O treated fungal cells can be clearly seen in the C-D channel. In the contrast, the control group only shows very vague cell shapes due to cross phase modulation (XPM) [15](Figure 2.7 (a)). XPM is a non-resonant process and not sensitive to the wavenumber change, which is typically treated as a constant background. Similarly, the perdeuterated oleic acid (OA-d34) treated ovarian cancer cells have strong C-D signal from the lipid, while the control group has no signal (Figure 2.7 (d)). The C-H SRS images of the same cells are recorded as references. The heat map of $I_{C-D}/(I_{C-D}+I_{C-H})$ ratio for the fungi and ovarian cancer cells are shown in Figure 2.7 (c) and (f), where the metabolism heterogeneity of the microbes and the lipid accumulation in ovarian cancer cells are clearly seen. The XPM contributes to the background appeared in the control group’s heat map.

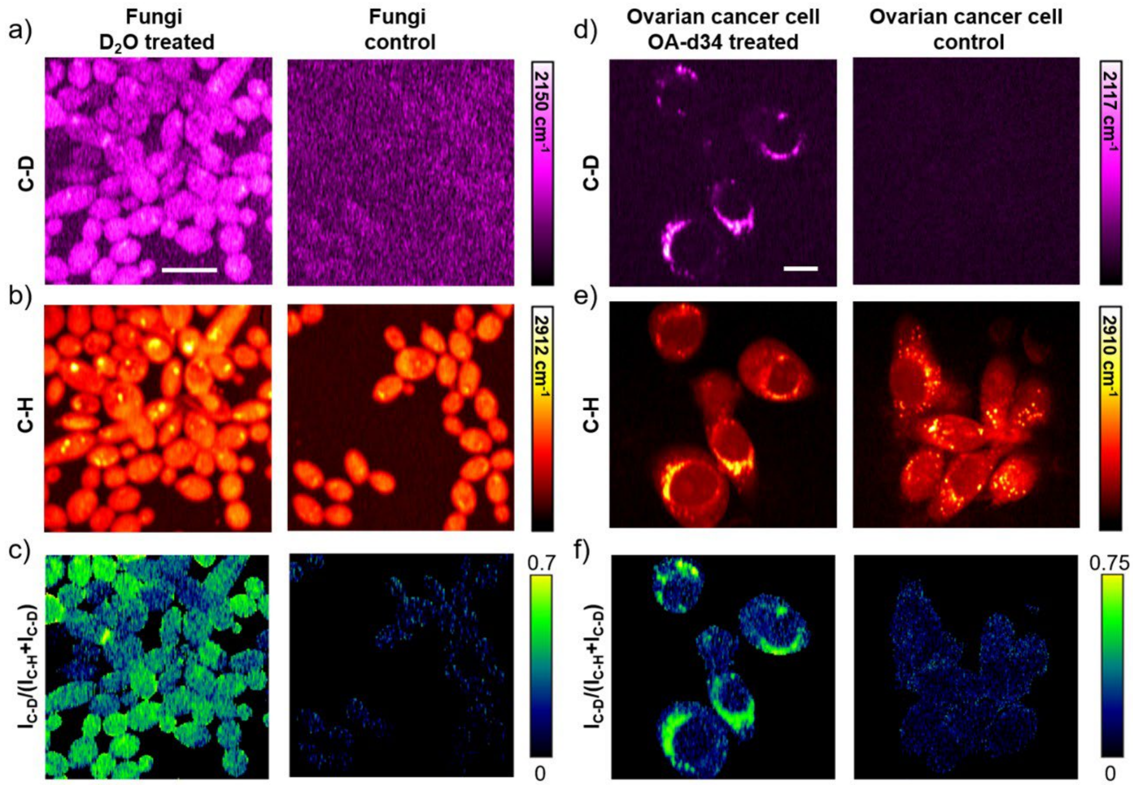

Figure 2.7: C-D/C-H SRL imaging of fungal and cancer cells.

(a) C-D SRL image of fungal cells with and without D_2O treatment. Power on sample: Pump: 21 mW, Stokes: 93 mW. Dwell time: 100 µs. 40 average. (b) C-H SRL image of fungal cells with and without D_2O treatment. Power on sample: Pump: 16 mW, Stokes: 95 mW. Dwell time: 10 µs. 10 average. (c) Heat map of $I_{C-D}/(I_{C-D}+I_{C-H})$ ratio calculated using (a) and (b). (d) C-D SRL image of ovarian cancer with and without OA-d34 treatment. Power on sample: Pump: 21 mW, Stokes: 93 mW. Dwell time: 100 µs. 10 average. (e) C-H SRL image of ovarian cancer with and without OA-d34 treatment. Power on sample: Pump: 16 mW, Stokes: 95 mW. Dwell time: 10 µs. 10 average. (f) Heat map of $I_{C-D}/(I_{C-D}+I_{C-H})$ ratio calculated using (d) and (e). Scale bar 10 µm.

Lastly, to evaluate the performance of our microscope for organism study, we imaged the same *C. elegans* in both fingerprint and C-H region. We chose 3 representative spectral channels: the 1649 cm^{-1} channel targets the acyl C=C bond and shows the distribution of unsaturated fatty acids; the 1675 cm^{-1} channel corresponds to the sterol C=C bond and reflects the cholesterol distribution; The 2850 cm^{-1} in the C-H region shows the overall lipid storage. We chose 1649 cm^{-1} and 1675 cm^{-1} instead of 1655 cm^{-1} and 1670 cm^{-1} where the acyl C=C and sterol C=C peak central locates in order to avoid the peak overlapping region to minimize channel cross-talk. The 3-color SRS imaging result of wild-type *C. elegans* is shown in Figure 2.8 (a). To confirm the SRS signal in the 1675 cm^{-1} channel is from the cholesterol, we also imaged the chup-1 mutant which lacks the cholesterol uptake protein [69]. Because the *C. elegans* can only obtain cholesterol from the environment, the chup-1 mutant should have a much lower cholesterol level than the wild type. The SRS images of chup-1 mutant is shown in Figure 2.8 (b), where the SRS signal almost disappear in the 1675 cm^{-1} channel. This result proves that the SRS signal in the 1675 cm^{-1} is mainly from the cholesterol. By comparing the 1649 cm-1 and 1675 cm-1 SRS images of wild-type *C. elegans*, it is found that the cholesterol is mainly distributed in the intestine area and lack in the epidermis (Pointed by the white arrows). We also calculated the ratio of I_{1649}/I_{2850} to represent the lipid unsaturation level of the lipid-rich particles in wild-type *C. elegans*, as shown in Figure 2.8(c). The ratio map at Z=0 μm corresponds to Figure 2.8 (a). The I_{1649}/I_{2850} ratio indicates a heterogeneity of lipid particles in *C. elegans* that the near-intestine lipid has higher unsaturation ratio than the lipid in the epidermis.

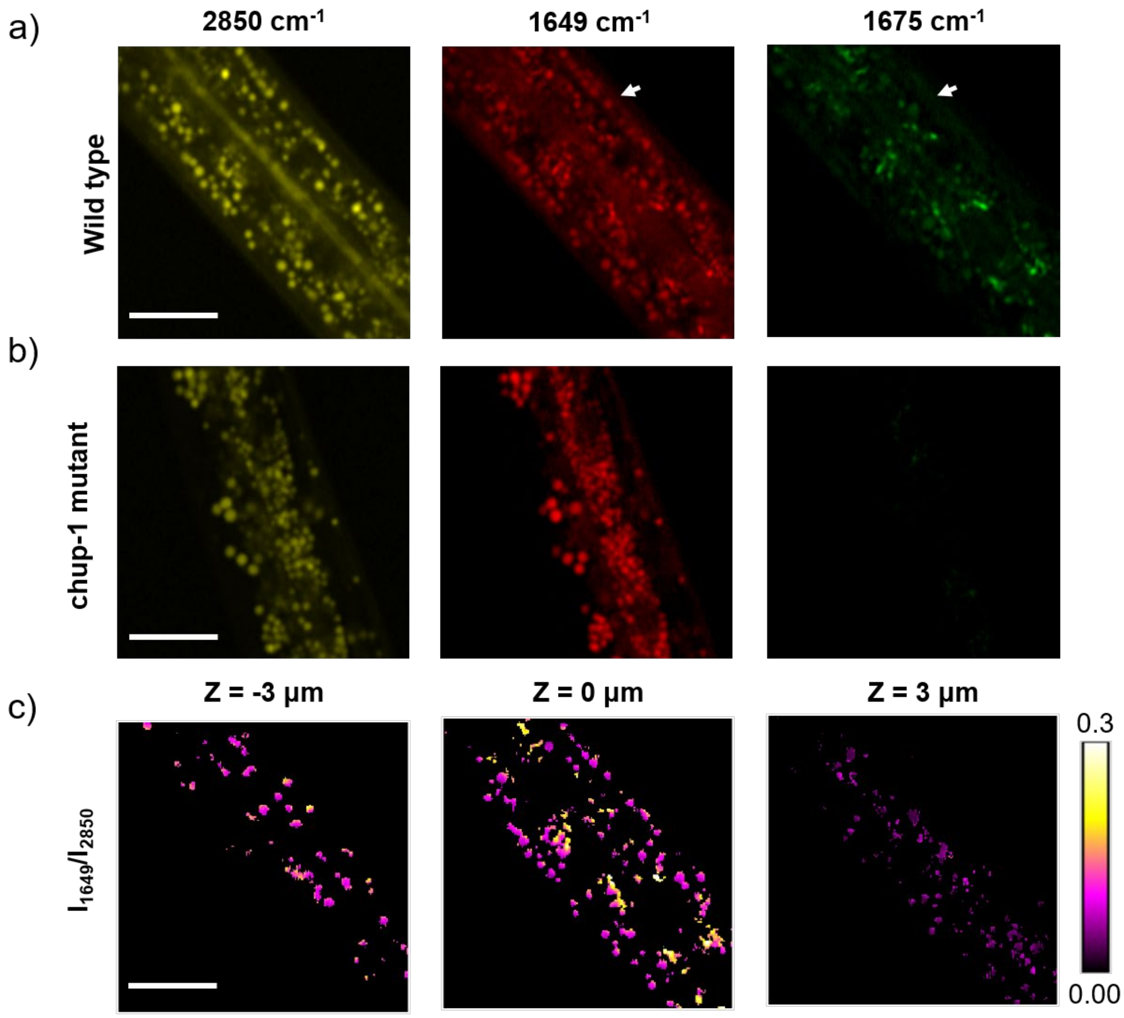

Figure 2.8: C-H and fingerprint SRL imaging of *C. elegans*.

(a) SRL images of wild-type *C. elegans* at 2850, 1649 and 1675 cm^{-1}. White arrow indicates the lipid droplets in epidermis lack cholesterol (b) SRL images of chup-1 mutant *C. elegans* at 2850, 1649 and 1675 cm^{-1}. (c) Depth-resolved map of I_{1649}/I_{2850} ratio for lipid particles in wild-type *C. elegans*. Z=0 μm is corresponding to (a). Power on sample: 2850 cm^{-1}: Pump: 12 mW, Stokes: 91 mW. 1649 cm^{-1} and 1675 cm^{-1}: Pump: 16 mW, Stokes: 79 mW. Averaging: 2850 cm^{-1}: 10 average. 1649 cm^{-1}: 20 average. 1675 cm^{-1}: 40 average. Dwell time: 2850 cm^{-1}: 10 μs. 1649 cm^{-1} and 1675 cm^{-1}: 100 μs. Scale bar 10 μm.

2.4 Discussion and conclusion

We demonstrated multi-window SRS imaging with a rapid widely tunable fiber laser. The fast spectral tuning capability across C-H, C-D and fingerprint regions enables cross-window quantitative analysis of cell metabolic activity. Furthermore, our multi-window SRS microscope is able to sample the spectrum selectively and discretely, which is in the contrary to spontaneous Raman [70] and broadband CARS imaging [71]. As the spectral data is highly sparse [72], the selective sampling would greatly boost the spectroscopic imaging speed and meanwhile lower the total laser energy on the sample.

In this work, we compared the SRG and SRL modalities. We note an independent, parallel work by Würthwein et al. demonstrated SRG imaging of polymer beads (30 μm in diameter), pure dDMSO (14.1 mol/L), lipid and dDMSO-soaked adipose tissue using the same laser source [73]. Due to limited power of the FOPO output (pump beam in SRS), SRG imaging of cell metabolism remains difficult (see Fig. 2 (d)). By applying auto-balanced detection to the FOPO beam, we successfully developed an SRL modality with greatly enhanced detection sensitivity (i.e., 20 mM DMSO as shown in Fig. 4 (b)). With this modality, we have mapped chemicals in biological cells and *C. elegans* in C-H, C-D, and fingerprint vibration windows.

In the fingerprint and C-D region, we applied a relatively long dwell time and multiple averaging to get good SNR, resulting in an imaging speed of 1~2 minutes per frame. The rapid spectral tuning speed of the laser is not fully utilized at this imaging speed. The SNR can be further improved with several approaches. Firstly, it is possible to suppress the laser noise to a lower level with the ABD. By modeling the residual noise after ABD suppression, we found the SRS detection is not shot-noise-limited or electrical noise-limited (Supplementary Fig. S5). It is possible to further reduce the electronic noise of our detector to achieve shot-noise limit detection. The second approach is to increase the detector saturation power threshold. The detector saturation issue limits the maximum laser power for the unmodulated beam. We will test photodiodes that have higher saturation level. By using new detectors with higher saturation level, we can potentially use full laser power provided by the FOPO and the oscillator, which could improve the SRL SNR by ~2 times and SRG SNR by ~9 times.

The FOPO instability is another issue of the current multi-window SRS system, which resulted in artificial sharp dips in current SRL spectra. This issue can be solved within a small tuning range by not tuning the oscillator wavelength but the repetition rate. With a fixed oscillator wavelength, the system allows tuning the FOPO wavelength over a small range in a smooth way, as demonstrated by Würthwein et al. using the same laser source [73]. We reported a multi-window SRS imaging system enabled by a rapid and widely tunable fiber OPO and auto-balanced detection. Our system is able to access Raman bands from 1050 cm^{-1} to 3150 cm^{-1} and can tune between two arbitrary wavenumbers within 5 ms. By analyzing the laser noise spectrum, we optimized the modulation frequency for SRG imaging. We implemented auto-balanced detection to suppress the pump noise by ~26 dB at 3.3 MHz, leading to an SNR improvement of 23 times in SRL imaging. With the auto-balanced SRL, we demonstrated multi-window SRS imaging across the C-H, C-D and fingerprint regions. Through hyperspectral SRL imaging in C-H region, lipid and protein distribution inside fungi and ovarian cancer cells are mapped. With C-D/C-H SRL imaging, D_2O metabolism in fungi and fatty acid uptake by ovarian cancer cells are visualized. Through multi-window imaging across the fingerprint and C-H region, we showed the heterogeneity in cholesterol content and unsaturation ratio of lipid particle inside *C. elegans*. These results collectively demonstrate the potential of a multi-window fiber-laser SRS imaging system in a wide range of applications.

3 CHAPTER THREE – HIGH-CONTENT STIMULATED RAMAN HISTOLOGY OF BREAST CANCER

The work in this chapter was published in Theranostics [74]. Reprinted with permission from Ivyspring International Publisher. This work was equally contributed by me, Chinmayee Prabhu Dessai and Dr. Haonan Lin. I contributed to data acquisition, algorithm optimization, data analysis and manuscript writing.

Breast cancer is one of the most common cancers among women worldwide. The gold standard for breast cancer is histology, including hematoxylin and eosin (H&E) and Immunohistochemistry staining. These traditional histology methods suffer from the labor-intensive preparation as well as inter- and intra- lab variation. In this work, we present a high-content Stimulated Raman Histology (HC-SRH) to overcome these limitations. Through spectral unmixing in the C-H vibration window, we can map unsaturated lipids, cell protein, extracellular matrix, saturated lipid, water in breast tissue. We successfully demonstrated the HC-SRH in a clinical-compatible fiber laser-based SRS microscopy. With the widely rapid tuning capability of the advanced fiber laser richer chemical contrast of breast tissue is obtained through multi-window SRS imaging.

3.1 Introduction

Breast cancer is one of the most prevalent cancers, accounting for ~15% of cancer-related deaths in women [75, 76]. As a highly heterogeneous disease, breast cancer requires detailed histopathology for diagnosis and treatment. However, the staining-based histology requires labor-intensive and time-consuming sample preparation, which inhibits rapid diagnosis. Besides, the inter- and intra-lab differences in the staining protocol can induce result variation, leading to a diagnosis discordance [77, 78]. Staining differentiates tissue components based on their chemical contents, so tissue imaging techniques that require minimum sample preparation while providing rich chemical information are good candidates to overcome the above-mentioned problems.

As a label-free non-destructive chemical analysis approach, Raman spectroscopy has been widely applied in cancer research [79, 80]. Spontaneous Raman spectroscopy can hardly be applied to tissue histology due to its slow signal acquisition speed, typically several seconds per spectrum. Coherent Raman scattering microscopy, based on either coherent anti-Stokes Raman scattering (CARS) or stimulated Raman scattering (SRS), overcomes this limitation through coherent excitation, enabling high-speed chemical imaging [27, 71, 81]. Compared to CARS, SRS is more favorable for clinical practice because SRS is free of non-resonant background and can be performed under ambient light. SRS microscopy has been used for label-free cancer histology. By detecting lipid-rich and protein-rich regions with two SRS spectral channels, two-color stimulated Raman histology (SRH) was developed to visualize brain tumor morphology [24, 82]. The two-color SRH results correlate well with the hematoxylin and eosin staining (H&E) data, which enables rapid intraoperative brain tumor analysis when combined with deep learning algorithms [25, 26]. The two-color SRH was also successfully applied to other cancer types, including gastric, prostate, and breast cancer [83-85]. Besides two-color SRH, other studies utilized SRS to map microcalcifications which is a well-known breast lesion biomarker, for breast tissue classification [48, 86]. The two-color SRH and microcalcification-based approach both achieved high breast cancer detection accuracy when combined with machine learning models. Nevertheless, these methods only detect one or two chemical components, which compromises the chemical mapping capability of SRS. Recent studies show that spectroscopic SRS is capable of targeting multiple biomolecules of interest [55, 87]. As cancer development involves a variety of biomolecules, providing such rich chemical information is important for accurate subtyping of breast cancer [88, 89] and enables precise treatment.

Here, we demonstrated high-content stimulated Raman histology (HC-SRH) that exploits the rich chemical information in spectroscopic SRS. By implementing hyperspectral SRS imaging in the C-H spectral window and subsequent sparsity-penalized unmixing, we mapped 5 major chemical components in breast tissue: saturated lipids, unsaturated lipids, cellular protein, extracellular matrix (ECM), and water. The change in amount and relative ratio of these components were shown to be closely related to cancer progression [90-93]. In our work, successful high-content chemical mapping in the crowded C-H window was achieved by a least absolute shrinkage and selection operator (LASSO) regression algorithm for spectral unmixing [52, 94]. As imaging speed is a key parameter for clinical trials, we further boosted the speed of HC-SRH by one order of magnitude through spectrally selective sampling. Our HC-SRH results showed various tissue components for sub-typing of breast cancers. Moreover, using a multi-window fiber laser-based SRS microscope [46], we demonstrate compact HC-SRH for which the results agree well with the state-of-the-art SRS system. In the meanwhile, the broader spectral range of the multi-window fiber laser enabled HC-SRH to map more types of biomolecules. Our fingerprint results showcased a clear contrast for nucleic acid and solid-state ester as well as representative peaks for different amino acids. These contrasts are beyond the reach of C-H based SRH and show the potential of fingerprint SRH for discovering new biomarkers for cancer diagnosis [89].

3.2 Methods and materials

3.2.1 SRS imaging systems and data acquisition

Figure 3.1 (A) shows the setup of a state-of-the-art SRS system based on a solid-state optical parametric oscillator (OPO). Without extra note, the SRS data was collected with this system. The solid-state OPO outputs two synchronized femtosecond laser pulse trains with 80 MHz repetition rate. The laser with shorter wavelength provides the pump beam and the other one fixed at 1040 nm provides the Stokes beam. For HC-SRH, the pump wavelength is centered at 800 nm. The Stokes beam is modulated by an acousto-optic modulator (AOM) at 2.4 MHz and pre-chirped by 15 cm SF57 rods. A motorized delay stage is put in the pump path to control the temporal overlapping of the two laser beams. The pump and Stokes are spatially combined with a dichroic mirror and then linearly chirped by 75 cm long SF57 glass rods. The combined beam is focused on the sample by a 60X water-immersion objective with 1.2 numerical aperture (NA). The transmission light is collected by an oil-immersion condenser with 1.4 NA and then filtered by a 1000 nm short pass filter to block the Stokes beam. The transmitted pump beam is detected by a photodiode. The SRS signal is conveyed as the modulation transfer from the Stokes beam to the pump beam. Extraction of the modulation is done with a lock-in amplifier. An SRS image is formed by laser scanning with a galvo mirror. A motorized sample stage is combined with the galvo mirror to cover a large field-of-view (FOV) for large-area tissue mapping. Hyperspectral SRS imaging is achieved through spectral focusing where the targeted spectral position is controlled by the temporal delay between the linearly chirped pump and Stokes laser pulses [87]. Second harmonic generation (SHG) imaging is performed in the same setup by replacing the photodiode with a photomultiplier tube. When performing SHG, only the Stokes laser is incident on the sample and a 520/70 bandpass filter is placed before the photomultiplier tube to filter out the Stokes beam.

Figure 3.1(B) presents the schematic of a compact SRS system based on a fiber OPO (FOPO) [63]. The setup of the FOPO-based SRS system is the same as the solid-state OPO-based system except for the modulation, hyperspectral scanning, and detection parts. The fiber laser outputs two synchronized picosecond laser pulse trains with 40 MHz repetition rate. The Stokes is modulated by a built-in modulator inside the laser at 6.7 MHz. This system realizes hyperspectral SRS by tuning the laser wavelength; therefore, no chirping rods and motorized stage are required. The FOPO can achieve arbitrary tuning between 700 and 3100 cm^{-1} within 20 milliseconds. Because the fiber laser has high laser intensity noise, auto-balanced detection is implemented to improve signal-to-noise ratio. Briefly, two identical photodiodes detect the transmitted pump beam and a reference pump beam without passing the sample. The signal amplitudes from the two photodiodes are matched automatically by the variable gain amplifier and the proportional–integral–derivative controller. The laser noise is then suppressed by performing difference of the two amplitude-matched signals. The SRS signal is obtained by demodulating the differential signal with a lock-in amplifier.

The laser power incident on the sample is set as follows: pump 15 mW, Stokes 50 mW for solid-state OPO-based SRS; Stokes 50 mW for SHG; pump 15 mW, Stokes 100 mW for fiber laser-based SRS. All the SRS data is acquired with 10 μs pixel dwell time and 500 nm pixel size. The imaging time is around 1.0 minute for 1.0X1.0 mm^2 per spectral channel.

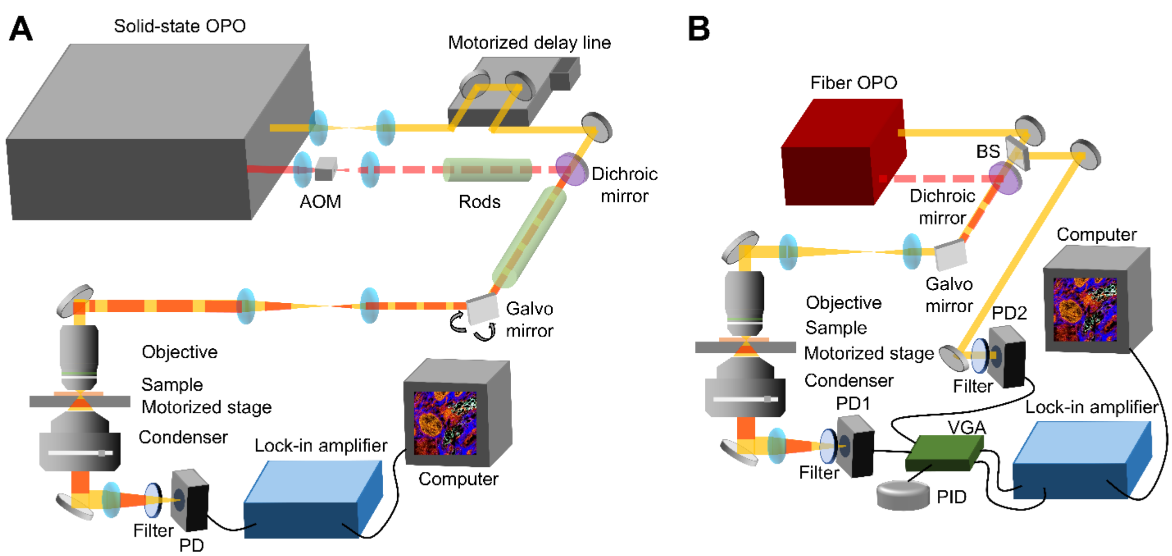

Figure 3.1: System schematic.

(A) A state-of-the-art SRS imaging system with a solid-state laser. (B) A compact fiber laser-based SRS imaging system. OPO: optical parametric oscillator. AOM: acousto-optic modulator. PD: Photodiode. VGA: Variable gain amplifier. PID: proportional–integral–derivative controller. BS: Beam Splitter.

3.2.2 Sample preparation

The human breast cancer tissue samples are freshly frozen tissue sections purchased from Biochain Institute (Newark, CA). The tissue samples were collected by the company from anonymous patients with ethics approval. Each tissue section has a thickness around

5~10 µm and was mounted on a standard glass slide. For SRS and SHG imaging, the frozen tissue slide was washed using 1X phosphate-buffered saline (PBS) and then covered with a glass coverslip. Nail polish was used to seal the coverslip to prevent tissue dehydration. To acquire histology, a neighboring section of the tissue section used for SRS was prepared for standard H&E staining. The co-registration of HC-SRH and H&E was done manually.

3.2.3 Data processing

For every large-area SRS imaging data, the small-FOV SRS hyperspectral images were first fused into a large-FOV image with the ImageJ grid stitching toolbox. The fused hyperspectral image was then denoised by the spectral total variation algorithm [95]. Finally, the denoised SRS data was fed into the LASSO algorithm with reference spectra for generating concentration maps. The principle of LASSO can be expressed as:

$$\hat{C}_i = arg\min_{C_i}\left\{\frac{1}{2}||D(i,:) - C_iS||^2 + \beta||C_i||_1\right\}$$

Where $D(i,:)$ is the spectrum of the ith pixel in the data, C_i represents the concentration for the targeted chemical components, S is the reference spectra for the targeted chemical components. β is the hyperparameter that can be fine-tuned to minimize channel crosstalk. We fixed β =0.01 in this work. The reference spectra for unsaturated lipids, ECM, saturated lipids, and water were acquired from glycerol trioleate, breast tissue ECM, palmitic acid, and 1X PBS, respectively. The cellular protein spectrum is extracted by subtracting the unsaturated lipid spectrum from the breast cancer cell spectrum.

Spectral selective sampling is performed by a recursive feature elimination (RFE) algorithm. The principle of RFE is to iteratively discard the least contributing channel for the LASSO unmixing result. To determine the least important channel, every channel in the current spectrum will be tentatively discarded and a mean square error (MSE) will be calculated between the current LASSO result and the LASSO result generated with the full spectrum. The channel corresponding to the minimum MSE is the least important. The RFE algorithm stops when the number of current spectral channels reaches the targeted value. Because RFE has high computational complexity, we only fed a small data set of 2100 pixels to the algorithm to accelerate the selection process. The 2100 pixels consist of 5 subsets, where every subset has a dominant chemical component and was randomly selected from a representative FOV. This design can balance the contribution of every chemical component in the selection process. The data processing flow for the spectral selective sampled SRS data is the same as the hyperspectral data.

3.3 Results

3.3.1 HC-SRH maps 5 chemical contents of breast cancer tissue

Figure 3.2 demonstrates that HC-SRH in the C-H window can successfully map 5 major chemical components in breast cancer tissue. Figure 3.2(A) shows the merged pseudo-color concentration map with yellow for unsaturated lipids, red for cellular protein, blue for ECM, cyan for saturated lipids, and grey for water. The separated concentration maps are shown in Figure 3.2(B), where the water channel is contrast-enhanced to visualize the details better. The reference spectra used for LASSO unmixing are also shown in Figure 3.2(B). The major spectral difference between the cellular protein and ECM is the overall spectral blue shift. This blue shift can come from the increased hydrogen bonds [96] or can be related to the fibrils formation [97].

To validate the concentration mapping given by HC-SRH, we compared the results of HC-SRH imaging with standard H&E staining on adjacent tissue section (Figure 3.2(C)). The unsaturated lipid is rich in the cell cytoplasm and fat cell residues, which is corroborated by the literature that breast cancer cells and adipose cells contain rich unsaturated lipids [98, 99]. The fat cells are seen as holes in HC-SRH because the tissue slicing procedure punctured the fat cells and only membrane-like residues remained. The cellular protein and ECM maps in HC-SRH agree well with the cell and ECM area in the H&E result. The fat cell residue area also shows a high saturated fat content in HC-SRH, which is consistent with that breast fat contains rich saturated lipids [98]. In addition, the solid-form saturated lipids are more likely to be preserved in tissue slicing. The water channel indicates that water is distributed across the whole FOV while the ECM contains slightly higher water content, and the fat residue area is lower in water content. This distribution makes sense because the main constituent of ECM, collagen, is hydrophilic, whereas lipid is hydrophobic. An enlarged view of one small FOV corresponding to the white box in Figure 3.2(A) is shown in Figure 3.2(D) with spectra of five representative pixels for cell nuclei, cell cytoplasm, ECM, fat cell residue and empty area.

We further compared HC-SRH with SHG which is commonly used for collagen imaging (Figure 3.2(E)). A cancer-adjacent blood vessel FOV is selected for verification because this FOV is rich in ECM including collagen and elastin. The H&E result is acquired from an adjacent section from the section used for SRS and SHG. The ECM channel of the HC-SRH correlates well with the SHG result. Yet, there are two main differences between the ECM channel of HC-SRH and the SHG. First, the intensity differs significantly for large and small fibers in SHG but appears more uniform in HC-SRH ECM channel. This difference may because SHG has a strong signal for type I and II collagen as well as highly aligned fibers but less sensitive to other types of collagens and small fibers [100]. The SRS signal is based on the protein concentration therefore provides better contrast for the small fibers. The second difference is that the blood vessel wall is visible in HC-SRH ECM channel but not in SHG. This difference is because the ECM of the blood vessel wall is rich in elastin [101], which can be detected by SRS but has a very low SHG signal.

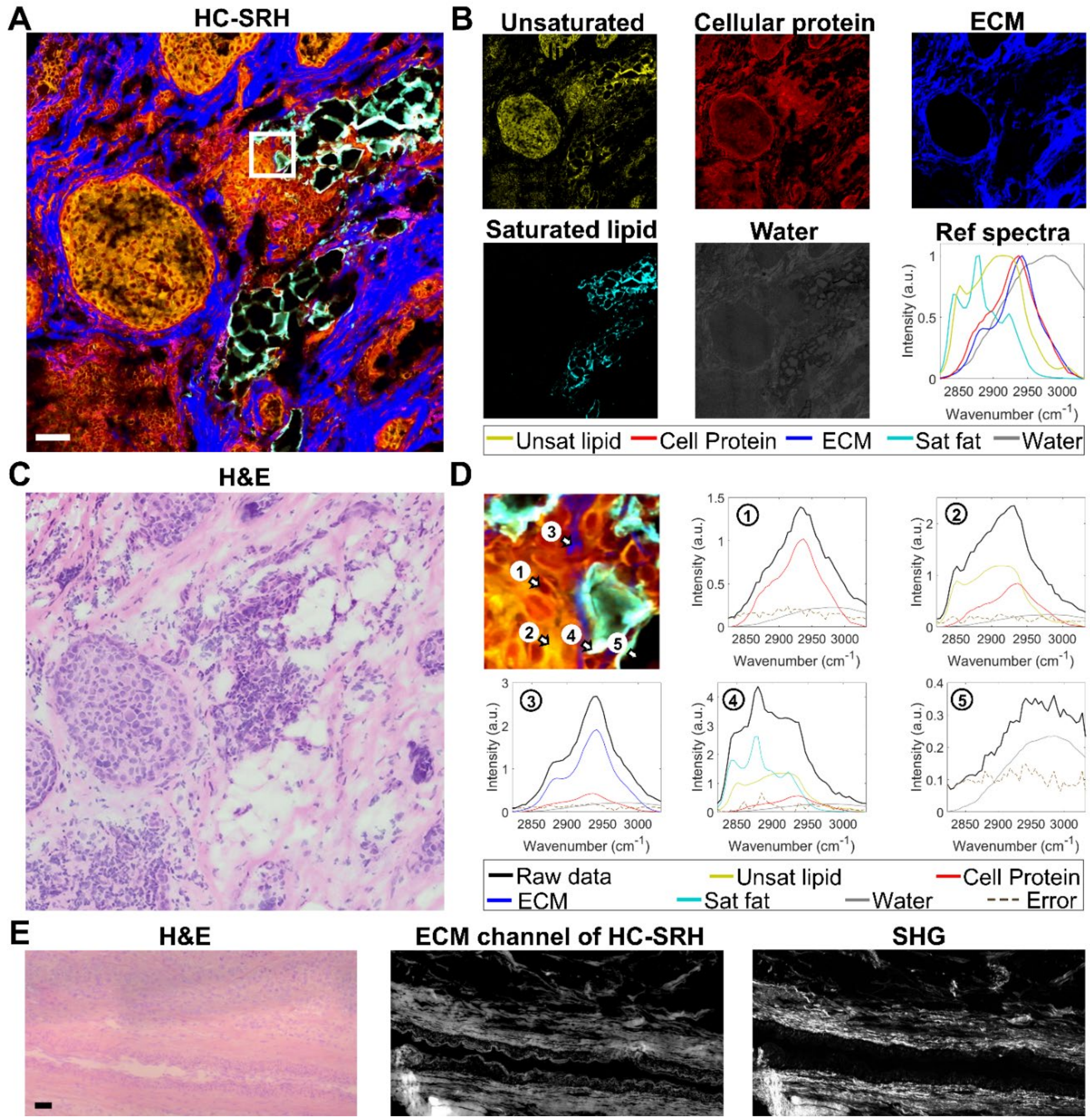

Figure 3.2: HC-SRH of human breast cancer tissue slice.

(A) Merged concentration map for a breast cancer tissue sample. Yellow for unsaturated lipids, red for cellular protein, blue for ECM, cyan for saturated lipids, and grey for water. (B) Separate concentration maps for the 5 chemical components and the reference spectra corresponding to (A). (C) H&E result of a neighboring section to the tissue section used in (A). (D) Zoom-in view of the white box in (a) and SRS spectra of the five selected pixels as numbered. (E) Comparison of HC-

SRH and SHG in mapping ECM in a cancer-adjacent vessel. Scale bar: 50 μm.

3.3.2 Selective spectral sampling boosts HC-SRH speed by one order of magnitude

The HC-SRH results shown in Figure 3.2(A) are generated with 45 SRS spectral channels covering 2820 to 3030 cm^{-1}, which required 40 minutes for the full field of view stack. As imaging speed is crucial for clinical practice, we boosted the speed of HC-SRH by reducing the number of spectral channels to be sampled. Theoretically, 5 chemical components require at least 5 channels to unmix. Therefore, we implemented the RFE algorithm to reduce the spectral channels to 5 while monitoring the HC-SRH result degradation to find a balance of between speed and image quality. Figure 3.3 presents the HC-SRH result of two breast cancer tissue sections with 45, 20, 10, and 5 selected spectral channels. The HC-SRH quality is quantified by the structural similarity (SSIM) and peak signal-to-noise ratio (PSNR) to the 45-channel result. The channel reduction does not lead to significant image quality degradation. Even with only 5 channels, the image quality is sufficiently enough for further analysis. Hence, the speed of HC-SRH can be boosted by 9 times by reducing 45 spectral channels to 5 selected ones (2837, 2880, 2908, 2951, and 3009cm^{-1}). Thus, there can be multiple good combinations for the selective sampling, which makes sense as the reference spectra in the C-H window cover a wide spectral range.

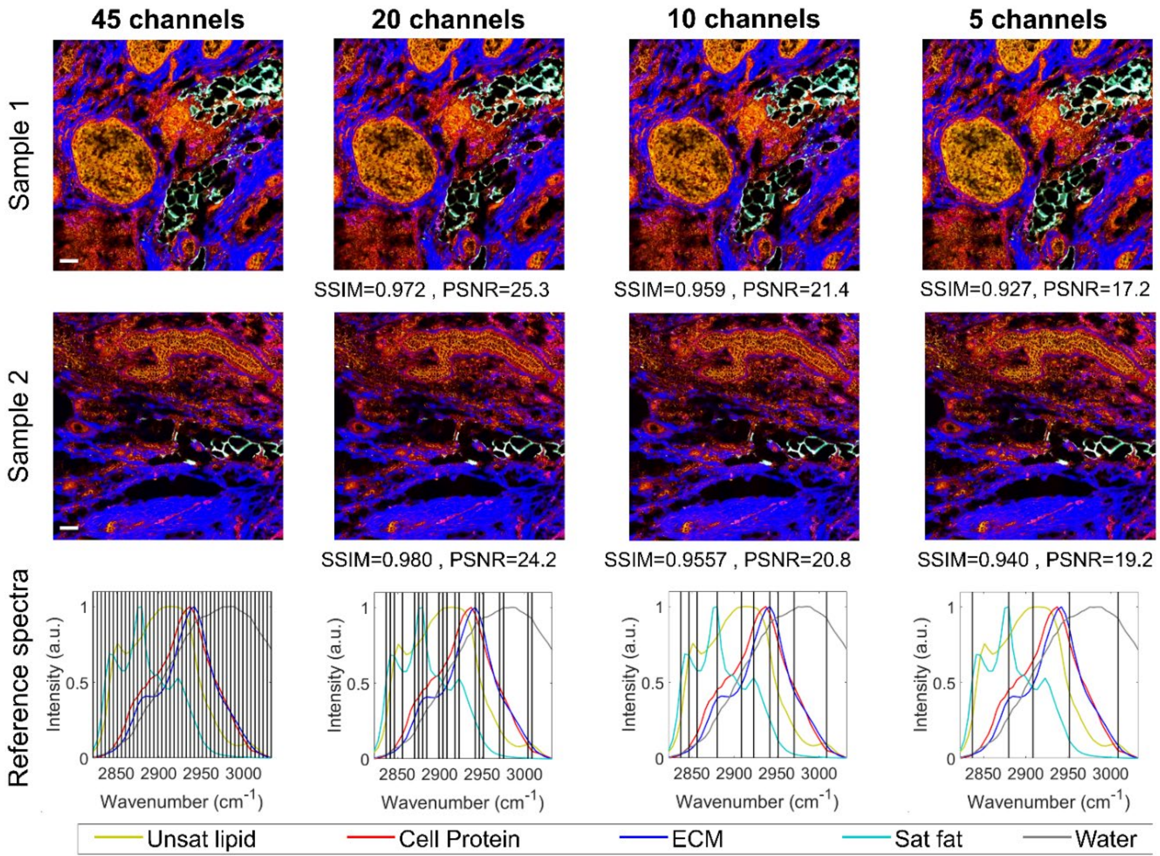

Figure 3.3: High-speed HC-SRH via spectral selective sampling.

Scale bar: 50 µm. SSIM: structural similarity. PSNR: peak signal-to-noise ratio.

3.3.3 HC-SRH provides excellent contrast for various breast tissue components

With the 5 selected spectral channels, we demonstrated the histology capability of our method by imaging different types of breast lesion and structure, including typical ductal carcinoma in-situ (DCIS), usual ductal hyperplasia (UDH), normal duct, invasive ductal carcinoma (IDC), invasive lobular carcinoma (ILC), and chemotherapy lesion (Figure 3.4(A)-(D)). Figure 3.4(E)-(H) shows the H&E results of adjacent sections corresponding to Figure 3.4(A)-(D). The SRH acquisition time for every tissue is less than 7 minutes.

We selected 10 regions of interest (ROI) from the four breast tissue sections to illustrate the performance of HC-SRH in detail. The ROI 1 is a typical DCIS where the cancer cells have grown inside the duct, and the ECM fibers nearby are stretched because of the over-growth. ROI 2 shows a necrosis area in the center of the DCIS duct, which is a signature of high-grade DCIS [102]. In HC-SRH, the necrosis shows an obviously higher cellular protein concentration than the surrounding cells, possibly due to cell condensation [103]. ROI 3 visualizes some stroma cells buried in the ECM, whose zoom-in view is shown in Figure 3.4(I). ROI 4 shows IDC permeates the fat cell area, where the fat cell morphology differs from the healthy fat cells with smaller structures surrounded by more ECM, which is the signature of cancer-associated adipocytes. (Figure 3.4(J)). ROI 5 presents a normal duct structure. ROI 6 is a usual ductal hyperplasia structure whose zoom-in is Figure 3.4(K). The duct cells in Figure 3.4(K) are overgrown, but the two-layer structure of the duct is still visible. ROI 7 is a blood vessel structure where the elastin around the vessel wall is shown as a mixture of ECM and cellular protein in HC-SRH. ROI 8 shows more intact fat cells close to the cancerous area. ROI 9 presents an ILC-like characteristic where cancer cells are aligned in a line shape (Figure 3.4(L)). ROI 10 shows a post-chemotherapy lesion consisting of newly grown collagen. The newly grown collagen is shown as a mixture of ECM and cellular protein in the HC-SRH, likely because the newly synthesized collagen is at an intermediate between fully grown collagen and cellular protein biomolecules. In summary, Figure 3.4 indicates that HC-SRH has excellent contrast for duct, necrosis, stroma, blood vessel, fat cell, chemotherapy lesion, and epithelial cell morphology, which corresponds well with the H&E result. In addition, HC-

SRH overperforms H&E in fat cell identification and distinguishing changes in the ECM composition.

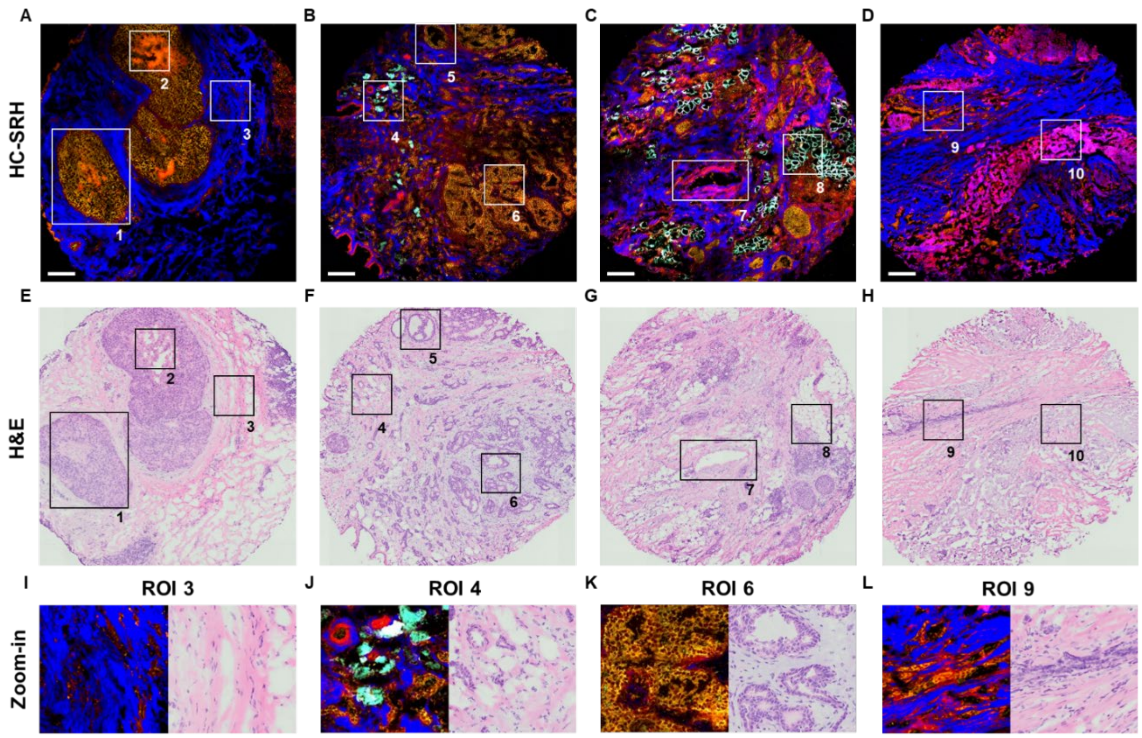

Figure 3.4: Breast tissue features revealed by HC-SRH.

(A-D) HC-SRH of breast lesion tissue with 5-channel selective spectral sampling. A: typical ductal carcinoma in-situ (DCIS); B: mixture of usual ductal hyperplasia (UDH), normal duct, and invasive ductal carcinoma (IDC); C: IDC and invasive lobular carcinoma mixture (ILC); D: Chemotherapy lesion and some ILC residue. (E-H) H&E of neighboring tissue section corresponding to (A-D). (I-L) Zoom-in of ROIs 3,4,6,9. Color representation: Yellow: Unsaturated lipid, Red: Cell protein, Blue: Extracellular matrix, Cyan: Saturated fat. Scale bar: 200 μm.

3.3.4 HC-SRH with a compact FOPO laser

The results in Figures 3.2-3.4 were acquired with a state-of-the-art SRS system operated with a solid-state OPO. The solid-state OPO is bulky and environment-sensitive, which is not suitable for clinical use. Furthermore, the complex optical alignment, e.g., spectral focusing, to achieve hyperspectral scanning requires well-trained users. A rapid-tuning picosecond fiber laser facilitates the system operation and is suitable for clinical translation. We performed HC-SRH on a recently built FOPO-laser-based SRS system [46]. Figure 3.5 compares the HC-SRH result acquired with the FOPO-laser-based system and that with the solid-state OPO-based system. Comparing Figure 3.5(A) and 3.5(B), we saw that selective spectral sampling can still preserve most of the HC-SRH quality using the same selected wavenumbers as in section 3.3.2. Equivalent image quality was achieved with fiber laser-based system as with solid-state OPO-based system (Figure 5B and 5C).

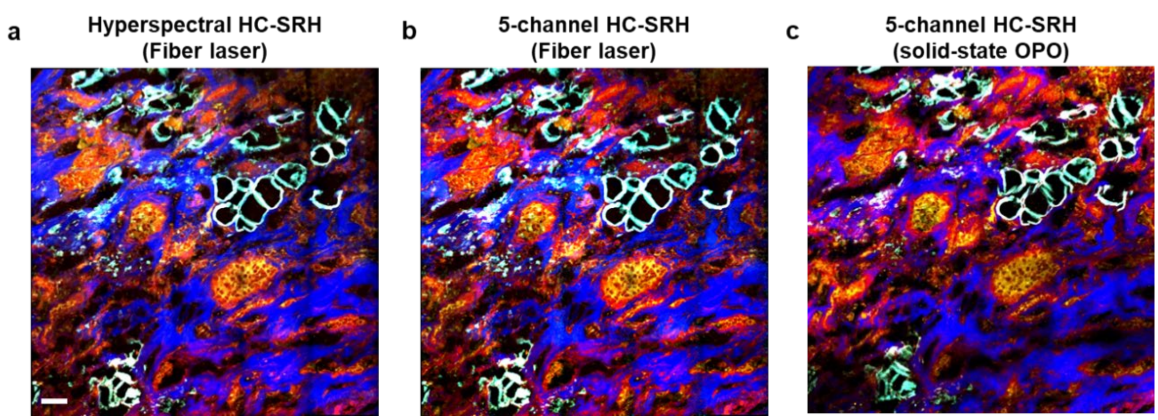

Figure 3.5: HC-SRH with a compact fiber laser.

(A) Hyperspectral HC-SRH (61 spectral channel) acquired by the FOPO-laser-based SRS system. (B) Selective sampled HC-SRH (5 spectral channel) acquired by the FOPO-laser-based SRS system. The spectral channel position is the same with Figure 3. (C) Selectively sampled HC-SRH (5 spectral channel) acquired in solid state OPO-based SRS system. Color representation: Yellow:

Unsaturated lipid, Red: Cell protein, Blue: Extracellular matrix, Cyan: Saturated fat. Scale bar: 50 μm.

3.3.5 SRS imaging of breast cancer tissue in the fingerprint window

Besides being clinically compatible, the FOPO-laser-based SRS system can complete fast tuning between two arbitrary wavenumbers within 20 milliseconds. This rapid spectral tuning capacity enables convenient spectroscopic SRS imaging across the whole biologically relevant Raman window. Fingerprint and C-H SRS hyperspectral images of a breast cancer tissue sample are shown in Figure 3.6. With the C-H HC-SRH (Figure 3.6(A)), we distinguished between different tissue components as introduced in section 3.1. The fingerprint images at the 6 characteristic Raman peaks are presented in Figure 3.6(B). The 790 cm^{-1} and 1495 cm^{-1} images corresponding to nucleic acid peaks can clearly visualize the cancer cell nuclei, which is beyond the reach of C-H SRH. Phenylalanine and carotenoids have a characteristic peak at 1005 cm^{-1}. Images at this wavenumber can help reveal the detailed composition of protein and lipids. The image at 1250 cm^{-1} corresponding to the collagen further validates our ECM mapping in the C-H HC-SRH. Combining the 1300 cm^{-1} image for lipids and the 1745 cm^{-1} image for ester, we find that the lipids in the fat cell residue are highly esterized, but the lipids in cancer cell cytoplasm are not. Thus, combining information from the fingerprint region data and the C-H region data can provide valuable information for more precise cancer diagnosis.

The fingerprint spectra of the 4 ROIs in Figure 3.6A are shown in Figure 3.6C. The 4 ROIs are selected to represent cancer cell cytoplasm, cancer cell nuclei, ECM, and fat cells. As expected, the cytoplasm spectrum shows a series of characteristic peaks for lipids and protein; the cell nuclei spectrum has many peaks corresponding to the nucleic acid; ECM spectra show many collagen features, and fat cell residue spectra are dominated by lipid characteristics. Another point to be noted is that we see a split ester peak in 1730 and 1745 cm^{-1} in the fat cell spectrum. This characteristic corresponds to a feature of solid-state fat [104], which is because the solid-state fat is better preserved than other lipids after tissue slicing. A detailed peak registration can be found in the **Table S1**.

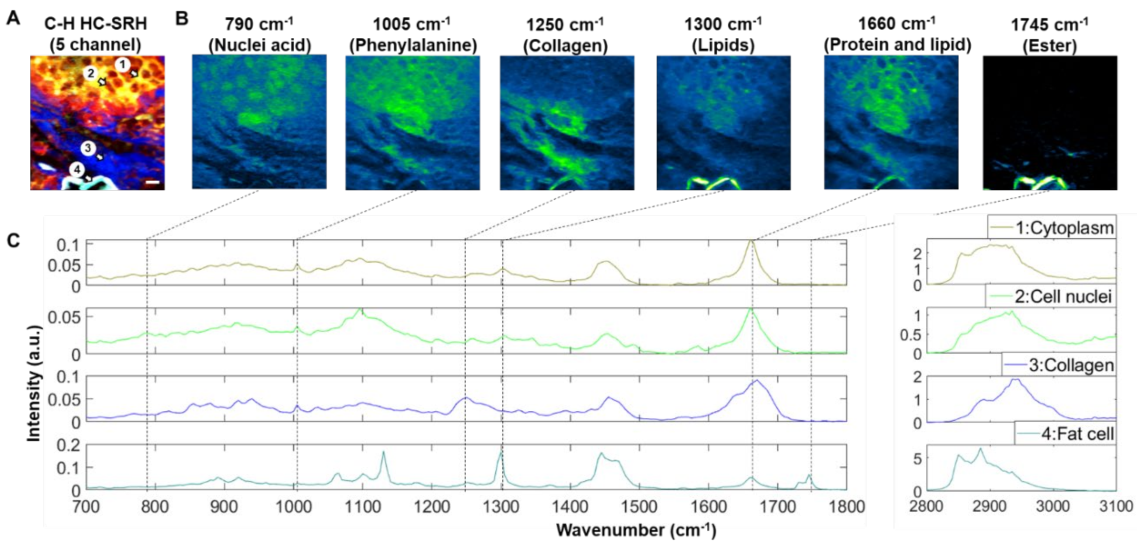

Figure 3.6: Fingerprint SRS imaging of breast cancer tissue.

(A) C-H HC-SRH result. Color representation: Yellow: Unsaturated lipid, Red: Cell protein, Blue: Extracellular matrix, Cyan: Saturated fat. (B) Fingerprint SRS result at representative spectral position in the same FOV of (A). (C) Multi-window SRS spectra of the 4 selected ROIs in (A). Scale bar: 10 µm.

Table 3.1: Peak registration for fingerprint and C-H SRS imaging of breast cancer

Peak	Cytoplasm	Cell nuclei	ECM	Fat cell	Registration
785		X			DNA (O-P-O)
825~830		X			DNA (O-P-O stretch)
855	X	X			Tyrosine
855			X		Collagen
880	X			X	Lipids/carbohydrates
880			X		Collagen
890				X	Solid state TAGs (CH3 rocking vibrations)
920	X	X	X	X	Proline ring / glucose / lactic acid (C–C stretch)
940			X		C–C stretch backbone
1005	X	X		X	Phenylalanine / carotenoids
1005			X		Phenylalanine
1035	X	X	X		Phenylalanine (C–H in-plane bending mode)
1065				X	Skeletal C–C stretch lipids
1075	X	X			Lipid (C–C or C–O stretch) / Nucleic acids (PO2 stretch)
1095	X	X			Phosphodiesters (O-P-O)
1100				X	Stearic acid
1130					Lipids (C-C stretch)
1205	X	X			Hydoxyproline / tyrosine
1250			X		Collagen (CH2 wag, C–N stretch)
1260	X	X			Protein (Amide III)
1300				X	Lipids (CH2 deformation)
1305		X			Adenine, cytosine
1455	X	X	X	X	Proteins/elastin/collagen/phospholipids (CH2)
1490		X			Nucleic acid purine bases
1585		X			Nucleic acid (Pyrimidine ring)
1640~1670	X	X	X		Protein (Amide I)

1660	X			X	Lipids (C=C)
1730 & 1746				X	Ester (C=O. polymorphic form)
2850					Lipids (symmetric CH2)
2885					Asymmetric CH2 stretch of lipids
2925					Saturated bonds of lipids
2930	X	X		X	Lipids (asymmetric CH2 stretch)
2940	X	X	X		Protein (C-H stretching)
3010	X				Unsaturated Lipids (=CH)

3.4 Discussion and conclusion

In this study, we have developed stain-free HC-SRH that provides breast cancer histology with rich chemical information. Compared to the well-developed two-color SRH, HC-SRH provides extra chemical information that can benefit cancer diagnosis in two aspects. First, HC-SRH has the potential to improve cancer classification accuracy which is of great importance in clinics. Machine learning has been widely applied to histology results to obtain diagnostic information automatically. Although decent classification accuracy can be obtained from tissue morphology, studies have indicated that chemical information can further improve classification performance [41]. For clinical application, classification accuracy is of great importance, and every improvement is worthwhile. In addition, chemical information gained from HC-SRH can contribute greatly to our knowledge about cancer biology which can accelerate the discovery of new biomarkers. The informative fingerprint window is especially promising for identifying cancer biomarkers [5]. For example, microcalcifications [17, 18] and carotenoids [42] are indicated as biomarkers for breast cancer development, which have characteristic peaks in the fingerprint window. Other than relying on the morphological-based machine learning classification, HC-SRH can deepen our understanding of subtle chemical changes involved in cancer progression.

In order to further advance the HC-SRH toward clinical applications, several future works must be carried out. Firstly, an HC-SRH classification model based on either machine learning or specific chemical biomarkers needs to be established to generate diagnostic information, which can help the HC-SRH to be used by the doctor and fit into the existing clinical workflow. Such a model is missing in this work due to the limited number of samples. Moreover, HC-SRH would better be performed on fresh, unsliced biopsy samples, which would minimize the sample preparation requirement and avoid artifacts caused by the tissue slicing. One slicing artifact we observed is the loss of fat cells, resulting in dark holes in our imaging results. Additionally, the water channel of HC-SRH could have been more informative because the original water content in the tissue is altered during the sample preparation, i.e., frozen sectioning and external PBS. The feasibility of applying HC-SRH on fresh unsliced biopsy can be shown by the two-color SRH work performed on fresh breast needle biopsy samples [15]. As HC-SRH has the same imaging depth as two-color SRH, HC-SRH has the promise to be applied to unsliced biopsy to get the image of the tissue surface and performed on the fresh samples.

We have developed a new approach for label-free cancer histology called high-content stimulated Raman histology (HC-SRH). The HC-SRH in the C-H window allows the mapping of major chemical contents in the breast tissue and provides excellent contrast for various tissue components. Through implementing spectral selective sampling, we boosted the speed of HC-SRH by ~1 order without sacrificing image quality. We also demonstrated that the HC-SRH is robust with a clinical-compatible fiber laser system. With the rapid, widely tuning capability of the FOPO, we extended the spectral coverage of the HC-SRH to the fingerprint window, which provides extra contrast for nucleic acid, amino acid, and solid-state fat in breast tissue. Collectively, these results show that HC-SRH is a promising tool for label-free cancer histology with rich chemical information.

4 CHAPTER FOUR – SHORTWAVE INFRARED PHOTOTHERMAL MICROSCOPY

The work in this chapter was published in Nature Photonics [105]. Reprinted with permission from nature publishing group. This work was co-led by Dr. Yuhao Yuan. My role was system development, data acquisition and analysis, and manuscript writing.

Deep-tissue chemical imaging plays a vital role in biological and medical applications. Current approaches suffer from water absorption and tissue scattering, which limits imaging depth to hundreds of micrometers. The short-wave infrared spectral window allows deep tissue imaging, but typically features unsatisfactory spatial resolution or low detection sensitivity. Here, we present a shortwave infrared photothermal (SWIP) microscope for millimeter-deep vibrational imaging with micron lateral resolution. By pumping the overtone transition of carbon-hydrogen bonds and probing the subsequent photothermal lens with shortwave infrared light, SWIP can obtain chemical contrast from one-micron polymer particles located at 800-μm depth in a highly scattering phantom. The amplitude of the SWIP signal is shown to be 63 times larger than the optically probe photoacoustic signal. We further demonstrate that SWIP can resolve intracellular lipids across an intact tumor spheroid and the layered structure in thick liver, skin, brain, and breast tissues. SWIP microscopy fills a gap in vibrational imaging with sub-cellular resolution and millimeter-level penetration, which heralds broad potential for life science and clinical applications.

4.1 Introduction

Probing cellular activities and functions in intact tissue is crucial for biomedical applications such as cancer pathology and drug discovery [106]. Vibrational microscopy is a powerful tool for studying cellular functions by providing chemical contrast from nutrients, metabolites, and other biomolecules [8]. However, the imaging depth of current vibrational microscopy is not sufficient to map the chemical content in intact organoids or tissue without altering the natural microenvironment. Specifically, infrared spectroscopy-based approaches suffer from a strong water absorption which restricts the penetration depth to tens of micrometers [16]. Spontaneous or coherent Raman microscopy with visible or near-infrared excitation has large tissue scattering, limiting their imaging depth to around 100 μm [107, 108]. With detection of diffusively back-scattered photons, spatially offset Raman spectroscopy [109, 110] and spontaneous Raman tomography [111-113] can acquire signals beyond millimeter-deep in tissue. However, these methods have a millimeter-level spatial resolution, not sufficient to monitor cellular-level activity.

The shortwave infrared (SWIR) region (from 1000 to 2000 nm) [114] opens a new window for deep tissue imaging with reduced scattering compared to the visible region and lower water absorption compared to the mid-infrared region (Figure 4.1(a)) [9, 115]. Importantly, the overtone transitions, which are high-order harmonics of the fundamental modes of molecular vibrations (Figure 4.1(b)) reside in this window [116], allowing deep vibrational imaging. Among various SWIR modalities, diffuse optical tomography can image beyond millimeter-deep in tissue, yet at millimeter-level spatial resolution [117]. Photoacoustic (PA) imaging achieves a higher spatial resolution by detecting acoustic waves with low tissue scattering [118, 119]. SWIR-photoacoustic microscopy (SWIR-PAM) allowed vibrational mapping of lipids in arterial tissues and drosophila embryo [9]. In SWIR-PAM, the transducer is placed at a considerable distance away from the absorption site. Acoustic signal loss takes place during the propagation, which degrades the detection sensitivity and constrains the detected target sizes to tens of micrometers. Additionally, acoustic coupling complicates the optical path design and is not applicable to samples sensitive to mechanical contact such as a patient wound [120]. Optically probed photoacoustic microscopy is developed for remote sensing purpose [120, 121] and has been extended to the SWIR window [122, 123]. However, the sensitivity of photoacoustic remote sensing is not sufficient for subcellular chemical imaging.

Here we present a shortwave infrared photothermal (SWIP) microscope for subcellular-resolution and millimeter-deep tissue imaging. By optically sensing the refractive index change directly from the absorption site (Figure 4.1(c)), SWIP prevents signal loss during propagation and eliminates the necessity of sample contact. Through a pump-probe scheme, SWIP achieves subcellular spatial resolution and millimeter-level imaging depth in highly scattering mediums, which allows imaging of single 1-µm polystyrene (PS) beads through 800-µm thick scattering phantom. Furthermore, the photothermal (PT) dynamics enables the detection of small objects over surrounding medium background. With these advances, we demonstrate volumetric SWIP imaging of intracellular lipids in an intact tumor spheroid, thick animal tissue slices, and human breast biopsy.

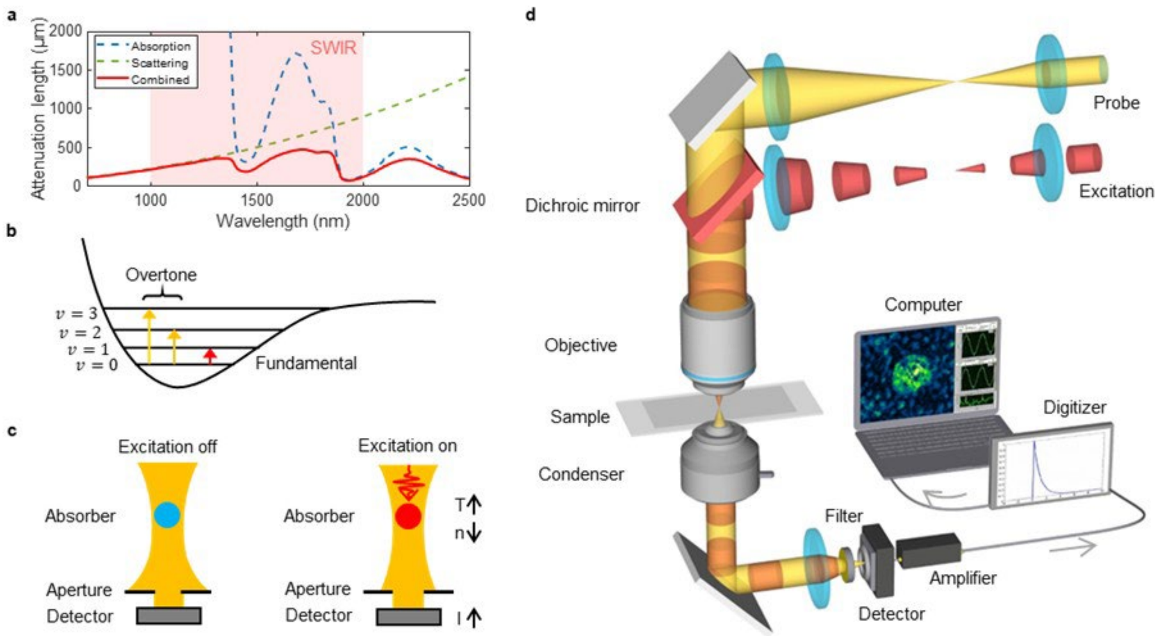

Figure 4.1: SWIP microscope principle and schematic.

(a) Wavelength-dependent attenuation length in brain tissue calculated with water absorption and brain tissue scattering coefficients [115]. (b) Overtone absorption energy diagram. (c) Photo-thermal contrast mechanism. T: temperature, n: refractive index, I: light intensity. (d) Short-wave infrared photothermal microscope schematic.

4.2 Methods

4.2.1 A shortwave infrared photothermal microscope

To fulfill the SWIP concept, we built a pump-probe microscope shown in Figure 4.1(d). Both pump and probe beams are in the shortwave infrared window to ensure deep tissue penetration. The pulsed pump beam is generated by an optical parametric oscillator (DX-1725-OPO, Photonics Industries), with a repetition rate of 2 kHz, wavelength centered at 1725 nm, and a pulse duration of 10 ns. The 1310 nm probe beam is provided by a CW diode laser (TURN-KEY CCS-LN/1310LD-4-0-0/OC, Research Lab Source Corporation).

The 1725 nm excitation laser is chosen to excite the first overtone of C-H stretching vibrations. Although the first C-H overtone absorption cross section is around two orders of magnitude smaller than the fundamental absorption [124, 125], detecting at the first overtone region can circumvent the strong water absorption in the mid-infrared region where water absorption is more than 3 orders stronger than that in the SWIR region [126]. Moreover, compared to the second overtone, the first overtone of C-H gives 7 times larger signal from lipids [127].

The beam sizes of the two lasers were adjusted to be around 6 mm with telescopes. The telescopes are also used for optimizing the axial offset of the two laser foci on sample to obtain maximum SWIP signal [128]. After beam expansion, the two lasers were collinearly combined with a dichroic mirror and then focused into a sample through an objective lens. The SWIP signal originating from the absorption-induced thermo-optic effect. The thermal-modulated refractive index forms a micro-lens and consequently alters the propagation of the probe laser, which modulates the light intensity collected through a small aperture inside the condenser (Figure 4.1(d)). Two objective lenses were used for the experiments. A 1.0 NA water-immersion objective with 800 μm working distance (UPLSAPO30XSIR, Olympus) was used to image the polymer beads, cancer cells, spheroid, swine liver, and human breast biopsy. A 2-mm working distance objective with an effective NA of ~0.4 was applied for mouse ear and brain imaging. The transmitted light from the sample was collected by an air condenser (D-CUO, Nikon) with an adjustable aperture. After the condenser, the remaining excitation laser was filtered out by a 1310 nm bandpass filter (FBH1310-12, Thorlabs). The signal-carrying probe beam is detected by a biased InGaAs photodiode (PD). When recording both PA and PT signals, we used a small-area high-speed PD (70 MHz bandwidth, 0.8 mm^2, DET10N2, Thorlabs). When only targeting the PT signal, we used a slower PD with larger active area (11.7 MHz bandwidth, 3.14 mm^2, DET20C2, Thorlabs). The photocurrent from the PD is converted to a voltage signal with a 50 Ohm impedance and then amplified by an AC-coupled low-noise voltage amplifier (100 MHz bandwidth, SA230F5, NF corporation) and digitized by a high-speed data acquisition card at 180 MSa/s (ATS9462, Alazar Tech). Every excitation laser pulse corresponds to a single pixel in the image. The image was formed by sample scanning achieved with a stage (Nano-Bio 2200, Mad City Labs). The volumetric image was acquired with a motorized z-knob to allow axial scanning.

4.2.2 SWIP image formation

Every pixel in the SWIP image corresponds to one excitation laser pulse, for which, a temporal trace of the probe laser intensity will be recorded. A gating method is applied to turn the signal temporal trace to pixel intensity. Two averaging windows are used: the first window is set before the excitation pulse arriving to estimate the probe intensity baseline; the second window starts at intensity extremum right after the excitation to obtain the changed probe intensity. The pixel intensity is assigned to be the difference between the two window averages. This gating method takes advantage of the long decay of PT signal for a better SNR. Multiple window sizes have been tested and the size of 80 sampling points (~450 ns) is chosen to output the best SNR.

4.2.3 Time domain extraction of SWIP signal from water background

The thermal property is closely related to the object size, shape, and chemical constitution. The thermal decay coefficient of SWIP signal can therefore provide extra information for differentiating small objects within bulk medium. When the particle size is smaller than the SWIP heating volume (usually satisfied for intracellular features as the axial resolution of SWIP is 3.5 μm), the heat dissipation of the small object is significantly faster than that of bulk surrounding medium. To reject the background from bulk medium with the thermal decay difference, the decay part of every SWIP signal trace is fitted with a two-component exponential function. Two-component exponential function is selected considering the detected SWIP signal consist of the in-focus target and out-of-focus water background contribution. A weight $w(x, y)$ is calculated by thresholding the decay coefficient $d(x, y)$ of the faster decay component. The water background is estimated by $a(x, y) + c(x, y) * w(x, y)$, where $a(x, y)$ and $c(x, y)$ are the amplitude of the two fitted exponential components. Assume the water background is spatially slow-varying, we applied a Gaussian blurring filter on the estimated water background to avoid sharp spatial intensity change. The final image is generated by subtracting the water background from the raw image. The background rejection workflow is shown in Figure 4.2(a).

Considering the fitting fidelity is related to the SNR, we tested the robustness of our fitting-based background rejection algorithm. As presented in Figure 4.2(b), weak signals with a SNR around 8 can be extracted with high fidelity.

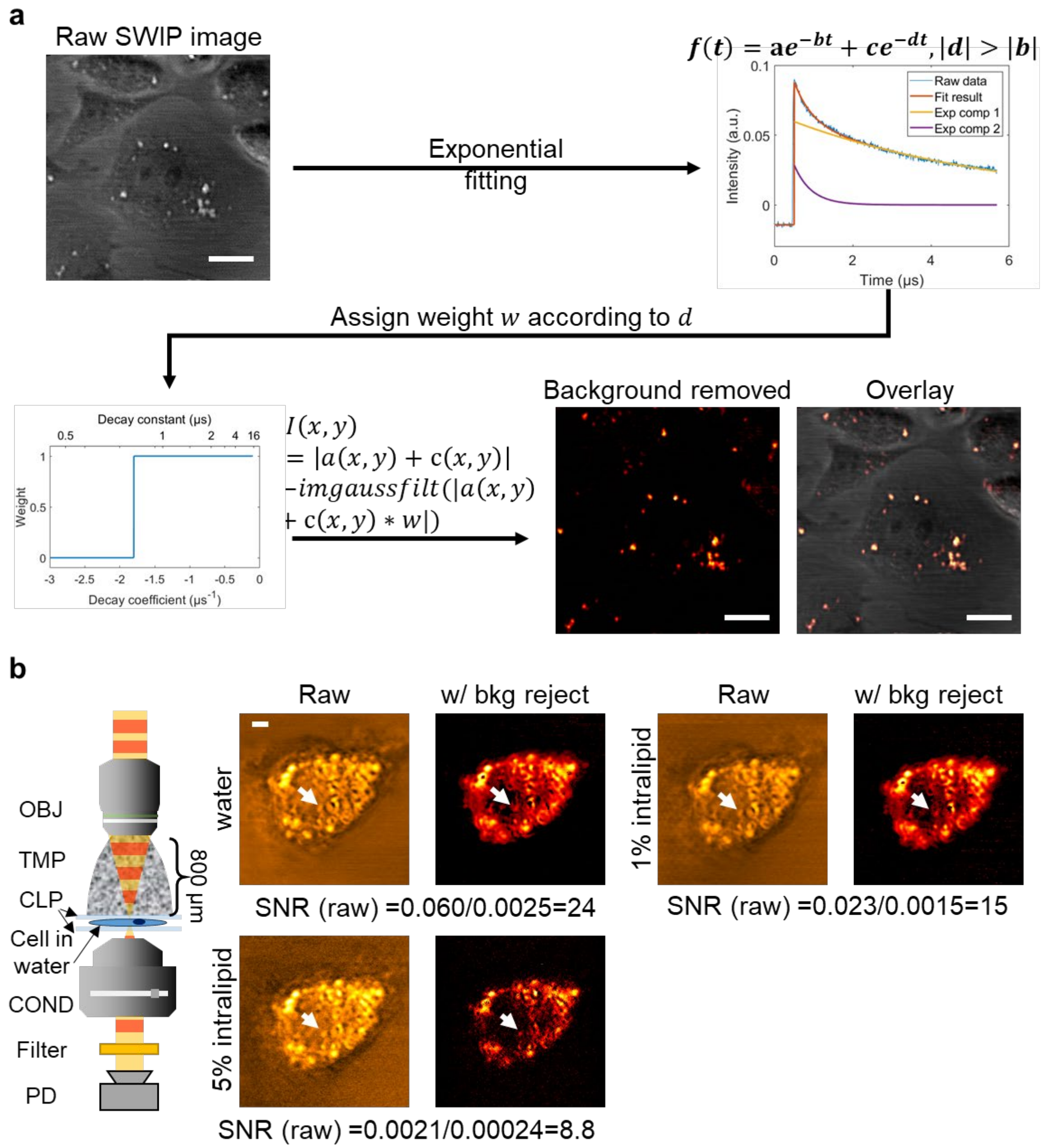

Figure 4.2: Time domain extraction of SWIP signal from water background.

(a) Water background rejection workflow. For the cell image example here, the single-pixel lipid area has a fitting result of a=0.07 a.u., b=0.12 μs^{-1}, c=0.03 a.u., d=1.96 μs^{-1}. The decay coefficient threshold is set as 1.8 μs^{-1}. Scale bar: 20 μm. (b) Background rejection test on OVCAR-5-cisR cells under scattering medium. (Left) Scattering phantom imaging schematic. OBJ: objective lens. TMP:

tissue-mimicking phantom. CLP: Coverslip. COND: condenser. PD: photodiode. (Right) SWIP imaging of cells and background rejection results through intralipid solution at different concentrations. The SNR is calculated from the lipid pointed by the white arrow. Laser power on sample: 1725 nm: 20 mW, 1310 nm: 8.5 mW. Scale bar: 5 μm.

4.2.4 SWIP spectroscopy

The SWIP spectra were acquired by replacing the single-color excitation laser with a tunable excitation laser (Opolette HE 355 LD, OPOTEK Inc), which has a tuning range from 410 to 2400 nm, a pulse duration of 5 ns and a repetition rate of 20 Hz. Other parts in the SWIP microscope remained unchanged. The spectral scanning was achieved by manually tuning the laser wavelength with a step size of 10 nm.

4.2.5 Limit of detection measurement

The limit of detection is the molar concentration with a signal intensity as 3 times of background standard deviation over the background [129]. If the signal has a linear dependence on the concentration, the LOD can be calculated by: $LOD=3\sigma/S$ [129], where σ is the standard deviation of the background intensity, S is the fitted slope of the signal versus concentration.

4.2.6 Stimulated Raman scattering microscope

Two synchronized femtosecond laser pulse trains with an 80 MHz repetition rate were used for SRS imaging. The wavelengths of the lasers are at 800 nm and 1040 nm to target the C-H stretch vibration. The 1040 nm laser is modulated by an acousto-optic modulator (AOM) at 2.27 MHz to separate the SRS signal from the laser repetition rate frequency. The SRS is conveyed by the modulation transfer from 1040 nm to 800 nm laser at 2.27 MHz. The two lasers are chirped to a few picoseconds with SF57 glass rods for spectral focusing. A dichroic mirror spatially combines the two lasers. The combined beams pass a pair of galvo mirrors for laser scanning, then is focused on the sample by the same objective (1.0 NA, UPLSAPO30XSIR, Olympus) used for SWIP. The transmitted light is collected by a 1.4 NA oil-immersion condenser and filtered by a 980 nm short pass filter. The residue 800 nm laser is detected by a biased photodiode. The SRS signal is obtained by demodulating the signal received by a photodiode with a lock-in amplifier.

4.2.7 Sample preparation

For standard chemical samples, the oil and DMSO solution samples were prepared by sandwiching 2 μl liquid with two no. 1 coverslips. An 80 μm double sided tape was placed between the two coverslips as a spacer. To prepare the polystyrene (PS) beads sample, an aqueous PS beads solution was first prepared and mixed well with an ultrasound homogenizer to avoid large aggregates. Then the beads solution was dried on a no. 1 coverslip. When performing SWIP imaging, the coverslip side was on the top to isolate the beads from the immersion medium or the scattering phantom. The protein and DNA samples for the SWIP spectrum acquisition were prepared by sandwich bovine serum albumin crystal (A2153, Sigma-Aldrich) and DNA powder (D3159, Sigma-Aldrich) between two no. 1 coverslips with 80 μm double sided tape as spacer.

To prepare the cancer cells and spheroids, cisplatin-resistant ovarian cancer cells (OVCAR-5-cisR) [130] were generously provided by the Daniela Matei Lab at Northwestern University. The cells were cultured in RPMI 1640 with 10 % fetal bovine serum, 100 units/ml penicillin and 100 μg/ml streptomycin. Cells were seeded on a coverslip for 24 hours for monolayer cell imaging. To form ovarian cancer spheroids, 200 μl/well of OVCAR-5-cisR cell suspension were added to an ultra-low attachment 96 well plate with a cell density of 0.5 x 10^4 cells/ml. The spheroids were cultured for 7 days. Cells were then kept in 1x Phosphate Buffered Saline (PBS) and sealed in between two coverslips with spacers.

The fresh swine liver was purchased from the supermarket. Before imaging, the liver was hand-sliced into around 3 mm and sandwiched between two no. 1 coverslips. The mouse ear sample was isolated from a 6-month-old mouse and fixed with 10% formalin solution. Before imaging, the ear was rinsed with 1x PBS and then attached to a coverslip. The mouse brain was from a 6-month-old mouse and fixed with 10% formalin solution. The brain was sliced to be 1-mm thick with a vibratome. Before imaging, the brain was rinsed with 1x PBS then attached to a coverslip. The de-identified healthy human breast biopsy sample was obtained from Susan G. Komen tissue Bank at the IU Simon Cancer Center. The breast biopsy sample was freshly frozen and had a thickness of around ~ 0.6 mm. Before imaging, the breast biopsy sample was defrosted then sandwiched between two coverslips.

4.3 Results

4.3.1 Optically detected photothermal versus photoacoustic signal

Under pulsed excitation, PT and PA conversions occur simultaneously. Studying the relative amplitudes between the coupled PT and PA signals is valuable in designing the detection scheme. We first performed a theoretical analysis of PT and PA contribution to the optically probed signal. Since both PT and PA signal can be written as a function of temperature rise, we have:

$$\delta n_{PT} = \alpha \Delta T \tag{16}$$

$$\delta n_{PA} = \frac{\eta n_0^3 p_0}{2\rho v_a^2} \tag{17}$$

$$p_0 = \Gamma \rho C_V \Delta T \left(\frac{\tau_{relax}}{\tau_{pulse}}\right) \tag{18}$$

$$\tau_{relax} = \frac{r_{focus}}{v_a} \tag{19}$$

Where δn_{PT} is PT-induced refractive index change, δn_{PA} is A-induced refractive index change, ΔT is initial temperature rise, p_0 is initial pressure rise, α is thermo-optic coefficient, v_a is speed of sound, τ_{relax} is the acoustic relaxation time, τ_{pulse} is the pulse duration, η is elasto-optic coefficient, n_0 is the initial refractive index of the sample, Γ is Gruneisen parameter, C_V is constant volume heat capacity, r_{focus} is the radius of probe focus. The amplitude ratio between optically probed PT and PA signal intensities could be calculated as:

$$\frac{I_{PT}}{I_{PA}} = |\frac{\delta n_{PT}}{\delta n_{PA}}| = \frac{2|\alpha| v_a^3 \tau_{pulse}}{\eta n_0^3 \Gamma C_V r_{focus}} \tag{1}$$

For olive oil, $|\alpha| = 0.00043\ K^{-1}, v_a = 1490\ m/s, \eta \approx 0.3, n_0 = 1.42, \Gamma = 0.9, C_V = 1970\ J * K * kg^{-1}$. Assuming $r_{focus} = 400\ nm$ calculated with 1310 nm probe wavelength and 1.0 objective NA, we find that $\frac{I_{PT}}{I_{PA}} \approx 47$.

The calculation indicates PT contributes over one order larger than PA. To validate this result, we measured PA and PT signals simultaneously using the SWIP microscope. Through fast digitization, PT and PA contributions can be differentiated by their temporal profiles (Figure 4.3). Because the estimated acoustic relaxation time is shorter than the pulse duration, PA initial pressure rise should have the same duration as the excitation pulse, which is 10 ns. In contrast, PT signal exhibits a long exponential decay as indicated by Newton's law of cooling. When the two foci were tight and in a good lateral overlapping (Figure 4.3(a)), the PT signal overwhelmed the PA signal (Figure 4.3(b)). A bipolar PA oscillation was observed with an amplitude 63 times smaller than PT (Figure 4.3(c)).

To confirm if the initial oscillation signal was from PA, we acquired 3 other signal traces under different focusing conditions. We recognize that PT is locally confined and PA propagates according to their diffusion speeds. Therefore, enlarging the probe focus size (Figure 4.3(d)) or introducing lateral displacement between two foci (Figure 4.3(g) and (j)) should selectively probe the PA signal[131]. As expected, under the modified schemes, the relative amplitude of PA became larger in the detected signal (Figure 4.3(e), (h), (k)), which could be clearly observed in the zoom-in views (Figure 4.3(f), (i), (l)). In an extreme case when two foci had little overlap (Figure 4.3(j)), the PT contribution in the probed signal became negligible and a typical acoustic bipolar oscillation was observed (Figure 4.3(k)-(l)). The width of the strongest PA pulse in Figure 4.3(f), (i), (l) was around 10 ns, consistent with the initial pressure rise theory. In Figure 4.3(c) and Figure 4.3(f), the oscillations following the strongest PA pulse represent the low-frequency PA components, whereas the ripples in Figure 4.3(i) and Figure 4.3(l) are a result of detector noise. Together, these results confirm the bipolar signal detected in Figure 4.3(c) is from PA.

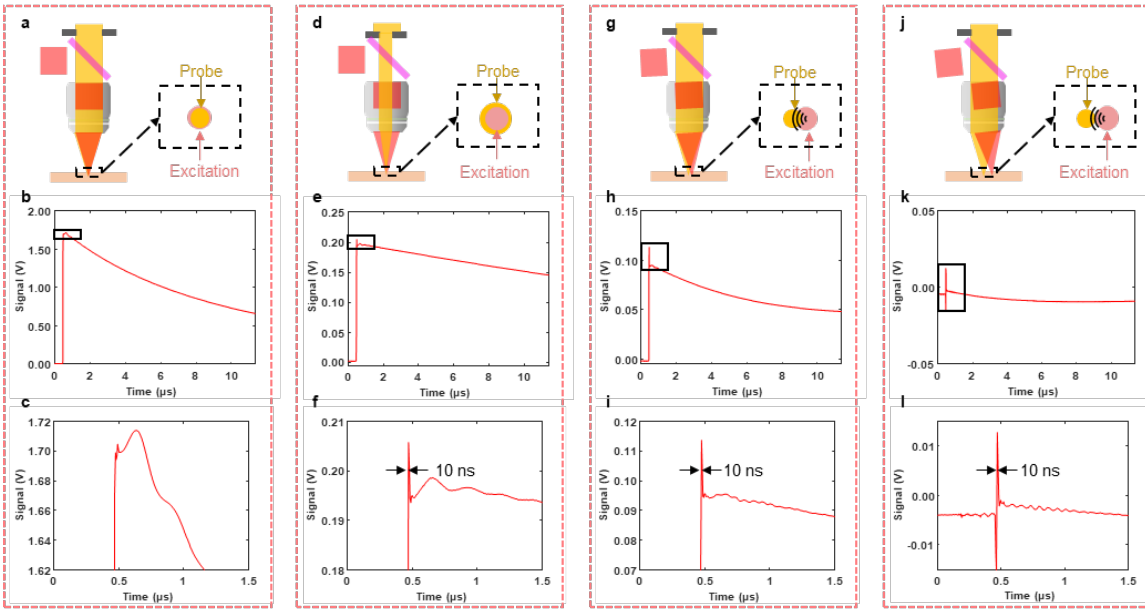

Figure 4.3: Comparison of optically detected photothermal and photoacoustic signals. (a) Normal SWIP focusing configuration where probe and excitation foci have similar size and good lateral overlapping. (b) Signal trace under the configuration in (a). (c) Zoom-in of (b). (d) Focusing configuration where the probe focus is enlarged by reducing the probe beam diameter before the objective, which leads to a reduced effective NA. (e) Signal trace under the configuration in (d). (f) Zoom-in of (e). (g) Focusing configuration where probe focus has a small lateral shift relative to the excitation focus. (h) Signal trace under the configuration in (g). (i) Zoom-in of (h). (j) Focusing configuration where probe focus has a large lateral shift to the excitation focus. (k) Signal trace under the configuration in (j). (l) Zoom-in of (k). Sample: Olive oil. SWIR excitation power on sample: 4.2 mW.

We noticed a slight mismatch between the theoretical calculation and the experimental result, possibly due to the deviation of the elasto-optic coefficient used in our calculation from the real value in our experimental system, or the limited bandwidth of our photodetector (70 MHz). Such mismatch does not influence the conclusion that the PT signal has more than one order larger amplitude than the PA signal in the well-overlapped tight-focusing condition.

To compare the detection sensitivity, we measured SWIP and optically detected PA signal dependence on dimethyl sulfoxide (DMSO) concentration in D_2O (Figure 4.4). The limit of detection (LOD) (See section 4.2.5) was 112 mM for SWIP and 7.78 M for optically detected PA. Thus, the LOD for SWIP is 69 times better than the LOD for optically detected PA, consistent with the measured amplitude difference on pure oil sample. Together, the SWIP amplitude is significantly larger than the optically probed PA in our configuration theoretically and experimentally.

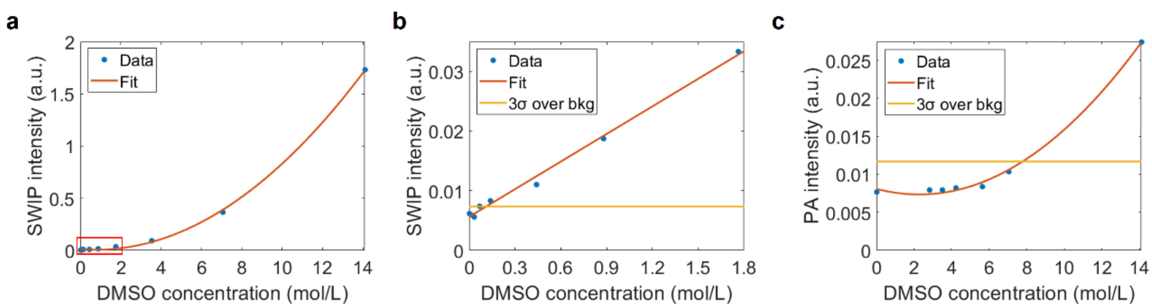

Figure 4.4: Limit of detection quantification for SWIP and optically detected PA.

(a) SWIP intensity dependence on the concentration of DMSO in D_2O. Signal is fitted with second order polynomial. Fitting result: $y=0.010x^2-0.015x+0.013$. Power on sample: 1725 nm: 5 mW, 1310 nm: 10mW. (b) SWIP intensity dependence on the concentration of DMSO in D_2O at the low concentration region. Signal is fitted with first order polynomial. Fitting result: $y=0.015x+0.0056$. 3σ over background is at $y=0.0074$. (c) Optically detected PA intensity dependence on the concentration of DMSO in D_2O. Signal is fitted with second order polynomial. Fitting result: $y=1.4e^{-4}x^2-6.5e^{-4}x+0.0081$. 3σ over background is at $y=0.0070$. Power on sample: 1725 nm: 5 mW, 1310 nm: 10mW.

4.3.2 A ball-lens model for the explaining SWIP contrast

To interpret the SWIP contrast, we developed a ball-lens model that connects the SWIP intensity with the thermal-induced refractive index change (Figure 4.5). Our model is based on a geometrical approximation, which ignores interference and diffraction for ease of understanding.

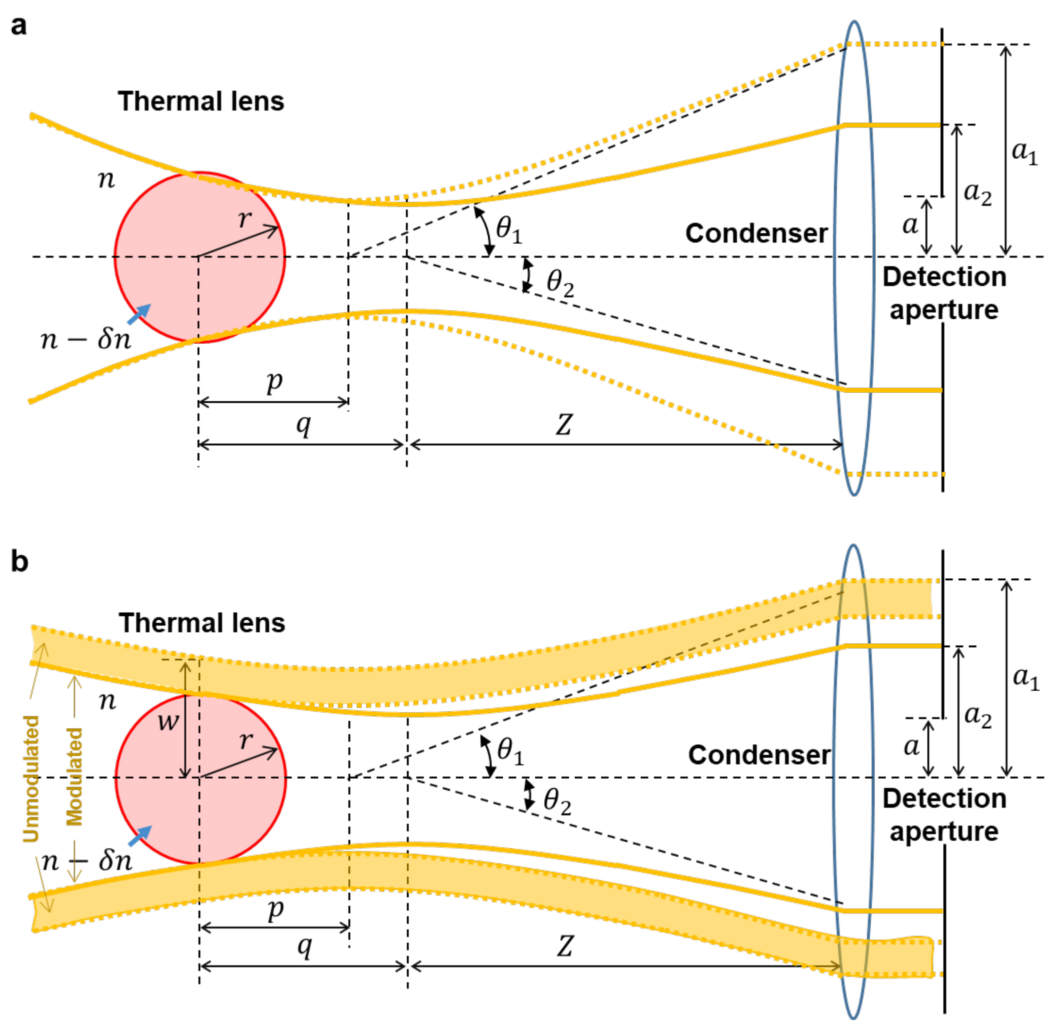

Figure 4.5: A ball-lens model for the optically detected photothermal signal.

(a) Detection schematic where the thermal lens is larger or matches the size of the probe focus. (b) Detection schematic where the thermal lens is smaller than the size of the probe focus. The red dashed line and solid line represent the propagation of the probe beam in the absence and presence of the thermally induced ball lens, respectively.

We first studied the case where the thermal-induced lens is larger than or matches the size of the probe beam (Figure 4.5 (a)). The generated thermal lens can be simplified as a ball lens with a uniform refractive index change δn and a radius r. n is the original refractive index of the sample, p and q are the distances from the thermal lens to the unmodulated probe focus and the modulated probe focus, respectively. θ_1, θ_2 are the divergence angles of the unmodulated and modulated probe laser. a is the radius of the detection aperture. a_1, a_2 are the radius of the unmodulated and modulated probe beam at the plane of detection aperture. According to the ball lens formula, we have:

$$\frac{1}{f} = \left(\frac{n - \delta n}{n} - 1\right)\frac{2}{r} = -\frac{2\delta n}{nr} \tag{1}$$

Assuming that the probe laser is a Gaussian beam. According to the Gaussian beam thin-lens equation:

$$\frac{\theta_1}{\theta_2} = m = \frac{f}{\sqrt{(p - f)^2 + z_R^2}} \tag{2}$$

Here, z_R is the Rayleigh range of the unmodulated probe laser. As $\delta n \ll n$, we have $|f| \gg r \sim z_R$. Therefore,

$$\frac{\theta_1}{\theta_2} \approx \frac{f}{f - p} \tag{3}$$

We assume a constant total intensity I_{probe} before and after the thermal modulation. We then denote the intensity distribution on the detection aperture plan for the unmodulated and modulated probe beam as I_1 and I_2:

$$I_1(r) = I_{probe}\frac{2}{\pi a_1^2}\exp\left(\frac{-r^2}{a_1^2}\right) \tag{4}$$

$$I_2(r) = I_{probe}\frac{2}{\pi a_2^2}\exp\left(\frac{-r^2}{a_2^2}\right) \tag{5}$$

Assuming $a \ll a_1, a_2$, the transmitted laser intensity after the detection aperture can be written as follows:

$$I_1^{det} = \int_0^a I_1(r) * 2\pi r\, dr = I_{probe}\left(1 - \exp\left(-\frac{a^2}{a_1^2}\right)\right) \approx I_{probe}\frac{a^2}{a_1^2} \tag{6}$$

$$I_2^{det} = \int_0^a I_2(r) * 2\pi r\, dr = I_{probe}\left(1 - \exp\left(-\frac{a^2}{a_2^2}\right)\right) \approx I_{probe}\frac{a^2}{a_2^2} \tag{7}$$

Here, I_1^{det} and I_2^{det} are the probe beam intensity on the detector without and with the thermal lens, respectively. The detected modulation depth induced by the thermal lens can then be calculated as:

$$(\frac{\Delta I}{I})_{bl\approx pr} = \frac{I_2^{det} - I_1^{det}}{I_1^{det}} = \frac{a_1^2}{a_2^2} - 1 \tag{8}$$

Here, *bl* and *pr* represent the ball lens size and the probe focus size, respectively. Under paraxial approximation, $a_1 \approx \theta_1 Z$, $a_2 \approx \theta_2 Z$. By utilizing $|f| \gg r{\sim}p$, Equation 8 can be re-written as:

$$(\frac{\Delta I}{I})_{bl\approx pr} = \frac{a_1^2}{a_2^2} - 1 = \frac{\theta_1^2}{\theta_2^2} - 1 = \left(\frac{f}{f-p}\right)^2 - 1 = \frac{-2fp - p^2}{(f-p)^2} \approx -2\frac{p}{f} = -4\frac{p}{nr}\delta n \tag{9}$$

In our scheme, δn is negative, which gives a positive modulation depth. By denoting β as the percentage of the probe laser transmitted from the sample to the detector through the aperture, the SWIP intensity can be written as follows:

$$I_{SWIP} = (\frac{\Delta I}{I})_{e \approx b} \beta I_{probe} = -4 \frac{p}{nr} \beta I_{probe} \delta n \tag{10}$$

The thermal-induced refractive index change δn arises from the temperature rise ΔT induced by optical absorption:

$$\delta n = \alpha \Delta T = \sigma N \tau I_{excitation} \cdot \alpha \frac{1}{C_p} \tag{11}$$

Here, α is the negative thermo-optic coefficient, C_p is the heat capacity of the sample; σ is the overtone absorption coefficient; N is the number of molecules in the focus volume, which represents the molecular concentration given a fixed focus volume; τ is the duration of the excitation pulse. As the excitation pulse (~10 ns) is short in SWIP, we do not consider the heat dissipation here; $I_{excitation}$ is the average intensity of the excitation laser within the pulse duration.

Combining equations 10 and 11, we get:

$$I_{SWIP} = \sigma N \tau I_{excitation} \cdot \alpha \frac{1}{C_p} \cdot (-4 \frac{p}{nr} \beta I_{probe}) \tag{12}$$

Equation 12 contains three parts. The first term presents the amount of optical absorption which is linear to the excitation intensity, overtone cross-section, and molecular concentration. This linear relationship lays the foundation for quantitative chemical analysis. The second term presents the conversion from optical absorption into a refractive index change. The third term presents the conversion of refraction index change into a probe intensity modulation. This term indicates that the SWIP intensity not only depends on the transmitted probe intensity (βI_{probe}), but also on the radius (*r*) of the thermal lens and the offset (*p*) of the probe focus from the thermal lens.

Next, we analyzed the case where the thermal lens with radius r is smaller than the probe focus (Figure 4.5(b)), i.e., the situation described in the main text Figure 4.4 (d). With an enlarged probe focus, only the central portion of the light is modulated by the thermal lens. This is equivalent to a reduced I_{probe} for calculating I_2^{det}. Denoting the probe beam radius w at the plane of the thermal lens, the I_2^{det} can be calculated as:

$$I_2^{det} = (I_{probe}\frac{r^2}{w^2})\frac{a^2}{a_2^2} \tag{14}$$

The modulation depth for Figure 4.5 (b) can then be written as:

$$(\frac{\Delta I}{I})_{bl<pr} = \frac{I_2^{det} - I_1^{det}}{I_1^{det}} = \frac{r^2}{w^2}\frac{a_1^2}{a_2^2} - 1 = \frac{r^2}{w^2}\left(\left(\frac{\Delta I}{I}\right)_{bl\approx pr} + 1\right) - 1 \approx \frac{r^2}{w^2}(\frac{\Delta I}{I})_{bl\approx pr} \tag{15}$$

Equation 15 shows a reduced modulation depth when the thermal lens is smaller than the probe focus. This reduction of modulated portion also explains the reduced PT modulation depth when the probe focus has a lateral offset from the thermal lens. We note that this model is based on geometrical derivation and considers no diffraction. A more rigorous analysis can be derived based on scattering theories [132, 133]. Overall, our theoretical model explains our experimental result shown in the main text and Figure 4.4.

4.3.3 SWIP imaging characteristics

Next, we characterized the performance of our SWIP microscope using standard samples. Figure 4.6(a) and (b) show the XY and YZ sections of volumetric SWIP images of 500 nm PS beads. The signal-to-noise ratio (SNR) of the XY image of a single bead was 25, suggesting the high sensitivity of SWIP. Figure 4.6(c) and (d) show the lateral and axial profiles of a single 500 nm PS bead, where the lateral and axial FWHM were 0.92 µm and 3.5 µm. After deconvolution with the bead's profile, the calculated system's lateral and axial resolution were 0.77 μm and 3.5 μm. Such a resolution is sufficient to resolve the subcellular features.

To confirm the chemical selectivity of SWIP, we acquired SWIP spectra of standard samples (Figure 4.6(e)). The SWIP spectra match well with the SWIR absorption spectra reported in the literatures[114, 134]. The peak registration was illustrated in Supplementary Material section 5. Figure 4.6(f) and (g) show a linear dependence of the SWIP signal on both excitation power and molecular concentration, consistent with the ball-lens model of SWIP contrast (Section 4.3.2). Based on the concentration curve (Figure 4.6(g)), the LOD of DMSO for SWIP was measured to be 112 mM. Under the same average power, the LOD of DMSO using a hyperspectral stimulated Raman scattering (SRS) microscope in our lab was 152 mM. Collectively, these data demonstrate good sensitivity and linearity of SWIP microscopy.

The deep-penetration, high-resolution imaging capability of SWIP was characterized with scattering phantoms. A tissue-mimicking intralipid aqueous solution was placed between the objective and 1.0 μm PS beads (Figure 4.6(h)). Note that 1% intralipid has a similar scattering coefficient to human skin epidermis [135]. Figure 4.6(i)shows the SWIP imaging results through water, and 1%, 5%, 10% intralipid. SWIP successfully resolved single 1.0 μm PS beads even under 10% intralipids. In comparison, near-infrared SRS imaging was performed under the same conditions (Figure 4.6(j)). In pure water condition, SRS showed higher resolution than SWIP due to shorter excitation wavelengths. However, the image quality of SRS quickly degraded as the intralipid concentration increased. No beads could be seen by SRS under 5% and 10% intralipid solutions. To investigate the resolution degradation of SWIP and SRS through scattering medium, we plotted the lateral profiles of a single bead and observed no significant broadening through scattering phantom for SWIP (Figure 4.6(k)) but a slight broadening for SRS (**Fig. 3l**), indicating SWIP can maintain good spatial resolution through highly-scattering medium, which is beyond reach of typical near-infrared SRS microscope.

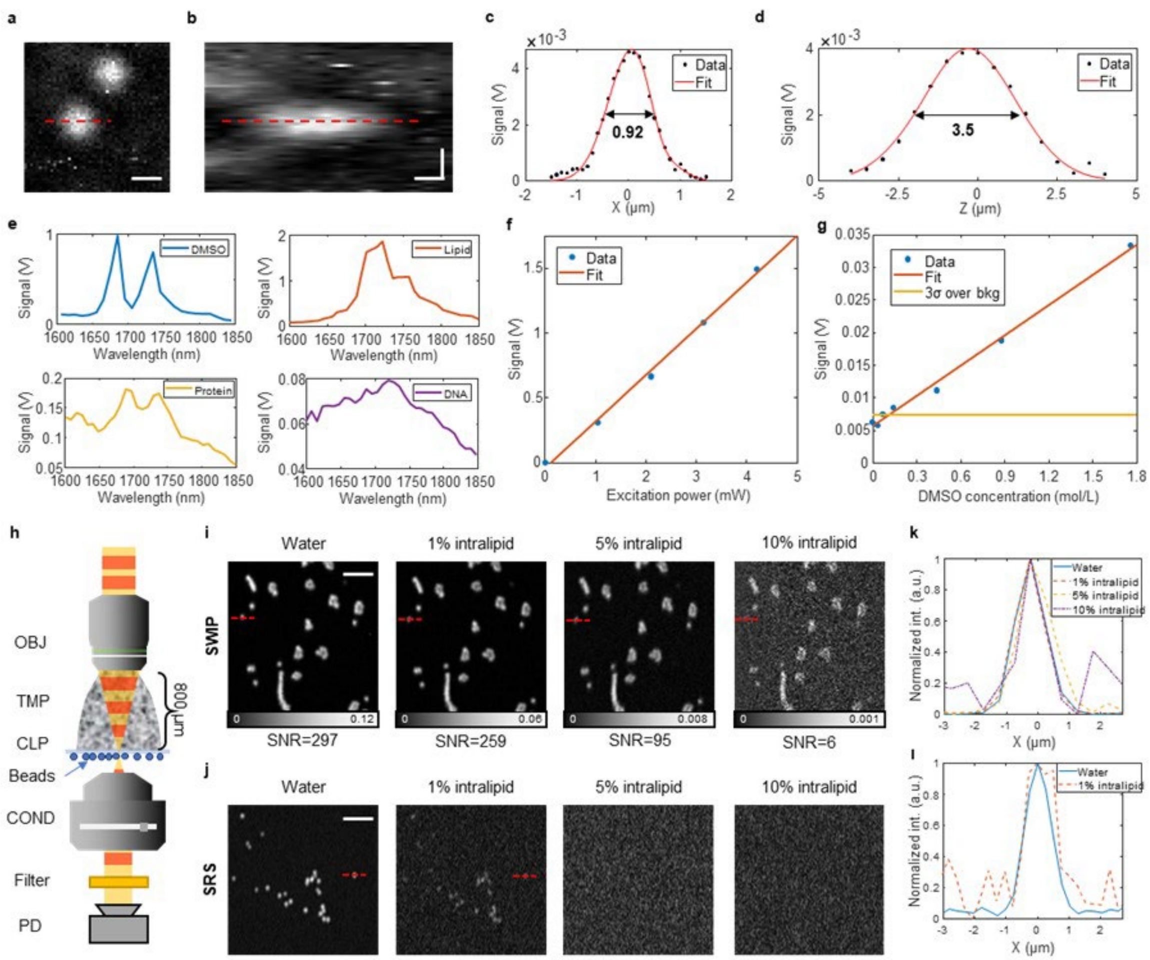

Figure 4.6: SWIP microscope performance.

(a, b) XY and YZ section of volumetric SWIP image of single 500 nm PS beads. Excitation power on sample: 20 mW. Scale bar: 1 µm. (c, d) Single 500 nm PS bead's lateral and axial profile corresponding to dashed lines in (a, b). (e) SWIP spectra of DMSO, lipid, protein, and DNA. (f)

SWIP signal dependence on excitation power. Sample: pure DMSO. (g) SWIP signal dependence on the concentration of DMSO in D_2O. (h) Scattering phantom imaging schematic. OBJ: objective lens. TMP: tissue-mimicking phantom. CLP: Coverslip. COND: condenser. PD: photodiode. (i) SWIP imaging results of 1.0 μm PS beads through water or scattering medium. Laser power on sample: 1725 nm: 20 mW. 1310 nm: 10.3 mW. Scale bar: 10 μm. (j) SRS imaging results of 1.0 μm PS beads through water or scattering medium. Laser power on sample: 798 nm: 10 mW. 1040 nm: 60 mW (water group). 798 nm: 50 mW. 1040 nm: 100 mW (intralipid groups). Scale bar: 10 μm. (k) Lateral profile of a single 1.0 μm PS bead in (i) as indicated by the red dashed lines. (l) Lateral profile of a single 1.0 μm PS bead in (j) as indicated by the red dashed lines.

4.3.4 SWIP imaging of lipids in an intact tumor spheroid

Tumor-derived spheroid is an in-vitro cancer model that better recapitulates tumor physiology than two-dimensional cell culture [136]. As cancer development is closely related to the altered lipid metabolism [137], imaging intracellular lipids help understand cancer progression and test drug effectiveness. However, imaging cellular components inside spheroids is challenging as the densely packed cells strongly scatter light. Sectioning [138] and tissue clearing [139, 140] have been applied to circumvent the strong scattering. Yet, these methods alter the metabolic state of spheroids and cannot be used for live sample study. Deep-penetrating multi-photon or light-sheet fluorescence microscopy can image live spheroids [141, 142]. However, fluorescent labeling is perturbative, especially for small lipid molecules [143].

SWIP provides an opportunity to overcome the above-mentioned challenges. We first validated the SWIP contrast on single-layer cells. SWIP well mapped intracellular lipids and revealed good cell morphology (Figure 4.7(a)). Utilizing the different thermal decay coefficients of lipids (Figure 4.7(b)) and bulk water (Figure 4.7(c)), the water background in Figure 4.7(a) was removed (blue arrow, Figure 4.7(d)) and the intracellular lipid contrast was enhanced (red arrow, Figure 4.7(d)). The logic and workflow of the background suppression are described in the section 4.2.3.

Figure 4.7(e) shows SWIP images of an intact tumor spheroid with a diameter of around 200 μm. In raw SWIP images, the intracellular lipids were successfully identified at the top, equatorial, and bottom planes. After background suppression, the intracellular lipids showed up cleanly. Individual cells can be identified by circles of intracellular lipids (blue arrow in Figure 4.7(e)). Hollow structures in the center of the spheroid can be observed (white arrow in Figure 4.7(e)). Figure 4.7(f) shows a background-removed three-dimensional volumetric SWIP image of the spheroid where an enriched accumulation and a relatively uniform distribution of lipid were seen.

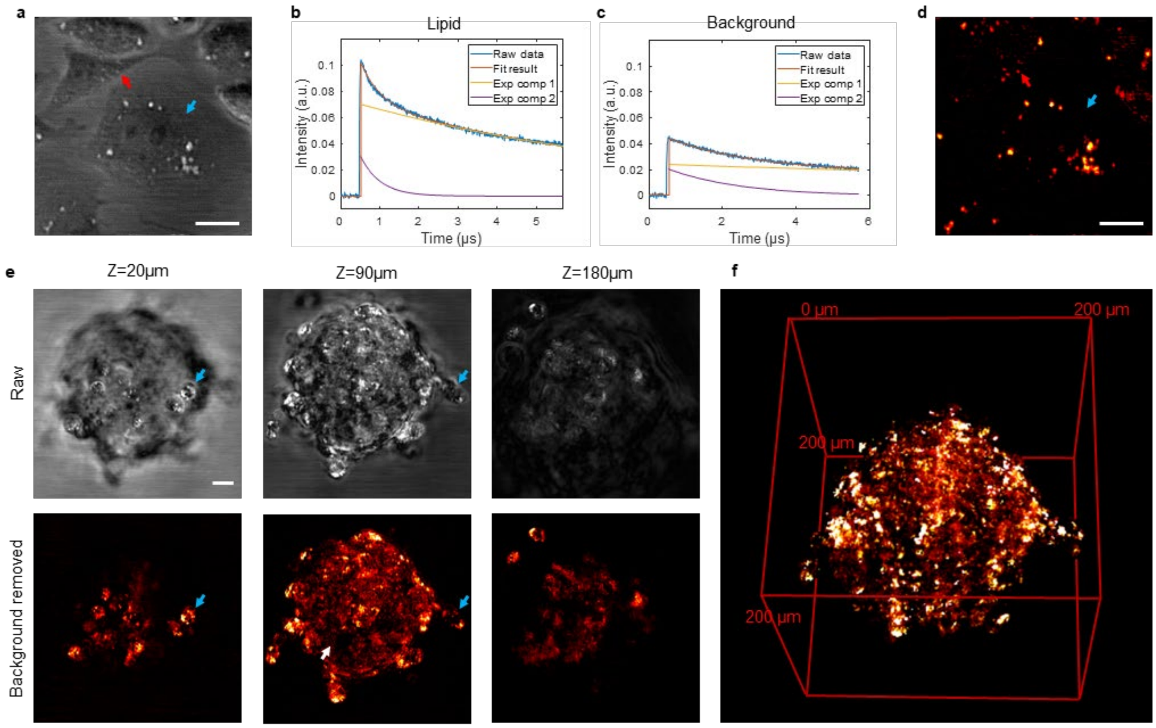

Figure 4.7: SWIP imaging of cancer cells and spheroid.

(a) Raw SWIP image of monolayer OVCAR-5-cisR cells. Red arrow: lipid droplets. Blue arrow: water area. (b) Single-pixel SWIP signal trace at the red arrow-pointed lipid area. The fitting result is $f(t) = 0.071e^{-0.12t} + 0.031e^{-1.96t}$. (c) Single-pixel SWIP signal trace at the blue arrow-pointed background area. The fitting result $f(t) = 0.024e^{-0.045t} + 0.020e^{-0.50t}$. (d) Background rejection result of (a) using the decay characteristic. Red arrow: lipid droplets. Blue arrow: water area. (e) SWIP imaging of an OVCAR-5-cisR spheroid. (f) 3-D rendering of volumetric SWIP imaging of the OVCAR-5-cisR spheroid after background rejection. Laser power on sample for all subpanels: 1725 nm: 20 mW, 1310 nm: 8.5 mW. Scale bars for all subpanels: 20 µm.

4.3.5 SWIP imaging of lipids in biological tissues

Lipids play an important role in biological tissue including energy storage, signaling, and transport of fat-soluble nutrients [144]. Imaging lipid content and its distribution inside a tissue enables a broad range of applications [145]. Because fluorescent labeling is perturbative for lipid molecules, vibrational imaging is widely adopted for lipid studies [143]. As mentioned, current vibrational imaging modalities do not allow high-resolution lipid imaging in deep tissue. Tissue sectioning is generally applied for high-resolution layer-by-layer imaging, but the sectioning process usually introduces morphological artifacts and causes lipid loss [146].

Here, we explored SWIP imaging of lipids in various types of tissues. Figure 4.8(a) shows SWIP images of a fresh swine liver slice. The lipid and liver morphology revealed by SWIP was consistent with previously reported SRS results [147]. Lipid droplets as small as 1.0 μm in diameter can be distinguished even at 300 μm deep inside the fresh liver with rich blood content, which cannot be achieved via existing modalities. Figure 4.8(b) shows SWIP images of a mouse ear. Characteristic layered structures were observed, including hair at Z=0 μm, sebaceous gland at Z = 52 μm, and subcutaneous fat layer or cartilage at Z=156 μm. SWIP can also image through a 1.0 mm thick brain slice and well capture the myelin fibrous structures (Figure 4.8(c)), confirmed by benchmarking with SRS on the same mouse brain slice (Figure 4.9). Images in Figure 4.8(b) and Figure 4.8(c) have a slightly lower resolution because of using a different objective with longer working distance and lower effective NA (see section 4.2.1). Figure 4.8(d) demonstrates SWIP images of fat cells at different layers across a 600 μm thick healthy breast biopsy.

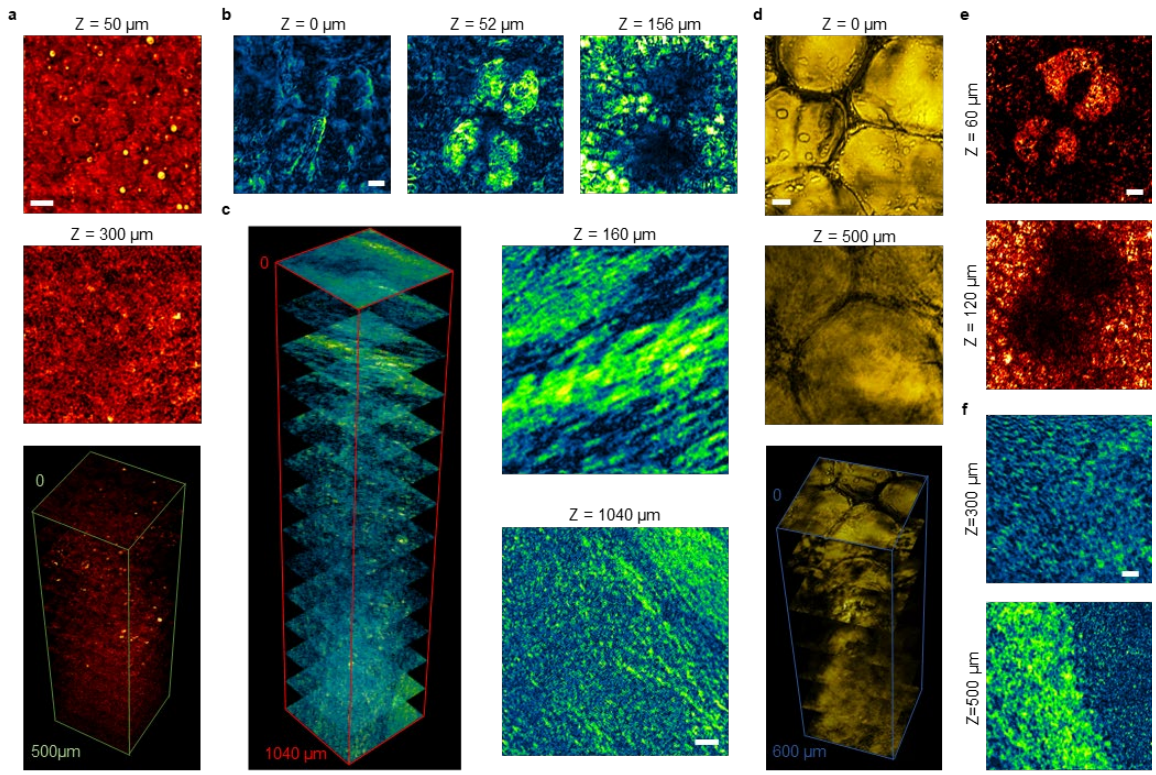

Figure 4.8: SWIP imaging of lipids in biological tissues.

(a) SWIP imaging of a fresh swine liver slice. (b) SWIP imaging of a mouse ear. (c) SWIP imaging of a mouse brain slice. (d) SWIP imaging of a breast biopsy from a healthy human. (e) Epi-SWIP imaging of a mouse ear at 60 µm and 120 µm depth. (f) Epi-SWIP imaging of a mouse brain at 300 µm and 500 µm depth. Laser power on sample: (a-d): 1725 nm: 20 mW, 1310 nm: 50 mW. (e-f): 1725 nm: 20 mW, 1310 nm: 70 mW. Scale bars for all subpanels: 20 µm.

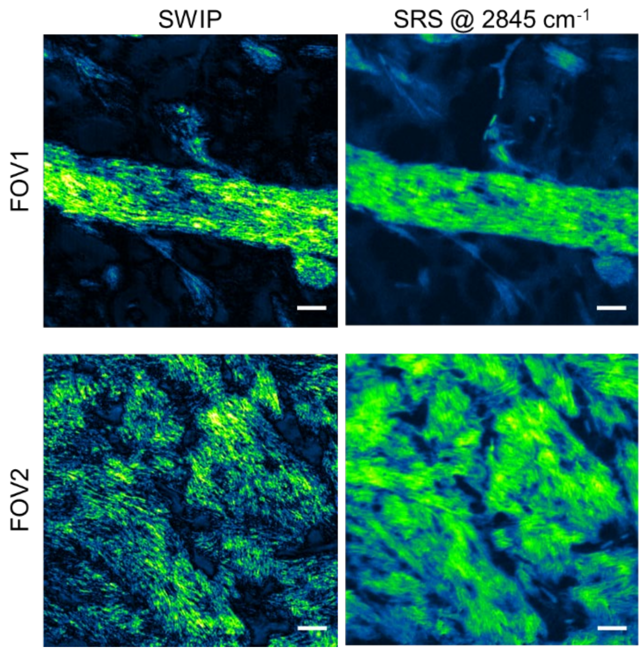

Figure 4.9: SWIP and SRS benchmarking on mouse brain slice.

SWIP power on sample: 1725 nm: 20 mW, 1310 nm: 10.3 mW. SRS power on sample: 800 nm: 15 mW, 1040 nm: 80 mW. SRS dwell time: 10 μs, 10 average. Scale bar: 20 μm.

Finally, towards in-vivo deep-tissue imaging, we demonstrated an epi-detected SWIP system (Figure 4.10 (a)). We harnessed an amplified photodiode with higher sensitivity to detect the weak back-scattered probe laser. Figure 4.10(b) shows epi-detected SWIP images of a mouse ear with sebaceous gland at Z=60 μm and subcutaneous fat layer or cartilage at Z=120 μm, well matched with the forward results (Figure 4.8(b)). Figure 4.10(c) reports epi-detected SWIP images of an intact mouse brain. The SWIP signal became stronger at Z=500 μm compared to Z=300 μm as the imaging plane moving from the cell-rich grey matter to the myelin-rich white matter. Together, these results show that in-vivo SWIP imaging could be potentially achieved.

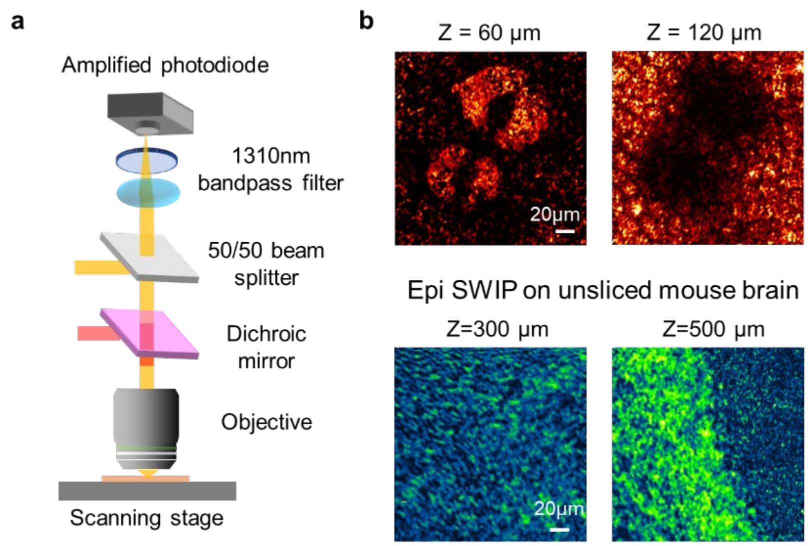

Figure 4.10: Epi-detected SWIP microscope.

(a) Schematic. DM: Dichroic mirror. BS: Beam splitter. BP: Bandpass filter. PD: Photodiode. (b) SWIP imaging of a mouse ear. (c) SWIP imaging of an unsliced mouse brain. Scale bar: 20 μm.

4.4 Discussion

A comparison of SWIP with existing vibrational imaging modalities in the depth-resolution space is illustrated in Figure 4.11. These techniques can be clustered into three groups. The first group (bottom-left) has subcellular resolution and sensitivity but limited imaging depth up to 100 microns. The second group (top-right) has deep penetration depth but relatively poor spatial resolution at best hundreds of microns. Although SWIR-PAM can achieve higher spatial resolution with tighter optical focus, the large signal loss leads to a low detection sensitivity and prevents it from probing small intracellular components. Clearly, there exists a gap between two groups for deep tissue vibrational imaging at subcellular resolution. As demonstrated in this work, SWIP successfully fills this gap. The millimeter-deep, micron-resolution, high-sensitivity vibrational imaging capability provided by SWIP opens exciting opportunities for many applications including live organoid study, slice-free tissue pathology, dynamic embryo imaging, etc.

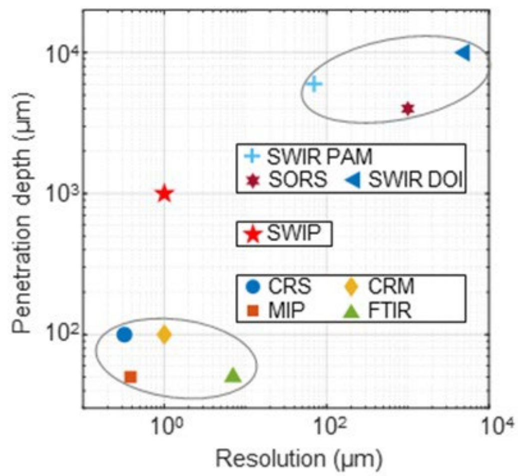

Figure 4.11: Penetration depth versus spatial resolution of vibrational imaging modalities. The data of penetration depth and spatial resolution are collected from reference [16, 107, 109, 117, 118, 148]. Group 1 (Bottom-left): CRS: coherent Raman scattering, MIP: mid-infrared photothermal, CRM: confocal Raman microscopy, FTIR: Fourier transform infrared spectroscopy; Group 2 (Top-right): SWIR PAM: short-wave infrared photoacoustic microscopy, SWIR DOI: shortwave infrared diffusive optical imaging, SORS: spatial-offset Raman spectroscopy; Group 3: SWIP: shortwave infrared photothermal.

As a nonlinear optical microscopy, both SWIP and SRS signals are largely contributed by ballistic photons. To interpret the distinct imaging performance of SWIP and SRS shown in Figure 4.6, we calculated the amounts of ballistic photons transmitted through a scattering medium. As shown in Table 4.1, through 800 µm of 10% intralipid, 1.9% and 0.11% photons at 1725 nm and 1310 nm remain ballistic, whereas the amounts of ballistic photons at 798 nm and 1040 nm are negligible. Thus, the deep imaging capability of SWIP largely benefits from the longer wavelengths.

Table 4.1: Absorption, scattering and attenuation data of 10% intralipid solution. $\boldsymbol{\mu_t = \mu_a + \mu_s}$. $\boldsymbol{T_b = \exp(-\mu_t l)}$ according to Beer–Lambert's law[149]. $\boldsymbol{\mu_s}$ is calculated using on a fitted model based on Mie scattering[150]. $\boldsymbol{\mu_a}$ is approximated with water absorption coefficients.

Wavelength (nm)	Absorption coefficient μ_a (mm^{-1})	Scattering coefficient μ_s (mm^{-1})	Total attenuation coefficient μ_t (mm^{-1})	Ballistic photon transmission through 800 µm phantom T_b
798	0.00233	27.50	27.50	2.8e-10
1040	0.02020	14.56	14.58	8.6e-06
1310	0.14891	8.369	8.517	0.0011
1725	0.62759	4.323	4.951	0.019

It is noteworthy that the SWIP signal intensity is sensitive to the focusing condition. As in Figure 4.3, the best configuration for PT detection is when two foci have similar size and in good lateral overlapping. The PA signal can be selectively detected if the probe volume is larger than the excitation volume, consistent with the photoacoustic remote sensing study [120]. Compared to PT, PA imaging has its own merits. The PA signal is closely related to the mechanical property which is valuable for many applications [151]. Furthermore, the high-frequency PA can circumvent low-frequency noises. Our data and theory relating the signal level with the focusing condition can serve as a guide for better utilizing the strengths of PT and PA.

The reported SWIP microscope can be improved in several aspects. By far, our single-color SWIP imaging using the first overtone absorption at 1725 nm mainly targets the C-H bond that is enriched in lipid content. With a wavelength-tunable excitation laser, hyperspectral SWIP imaging and subsequent decomposition can differentiate multiple molecular species such as proteins, fatty acids, cholesterol, and carbohydrates [114, 116]. We noticed that the SWIP LOD of 112 mM DMSO is relatively large compared to the molecule concentration inside a cell. Fortunately, many biomolecules such as lipids are locally concentrated, which ensures their detectability with SWIP. Furthermore, some biomolecules have multiple targeted bonds. As shown in Table S2, the C-H bond concentrations of cellular protein and lipid are much higher than the SWIP LOD for C-H bond. Thus, SWIP can be applied to study a variety of locally enriched biomolecules including lipid, cellular protein, and collagen.

Table 4.2: Comparison of C-H bond concentration corresponding to SWIP LOD of DMSO, cellular lipid concentration and cellular protein concentration.

Cellular lipid and cellular protein concentration is calculated from the data in literature[152].

	Concentration (M)	Number of C-H bond per molecule	Corresponding C-H bond concentration (M)
SWIP LOD of DMSO	0.112	6	0.224
Cellular lipid	0.0636	106 (estimated by dioleoylphosphatidylcholine)	6.74
Cellular protein	0.00151	2332 (estimated by bovine serum albumin)	3.52

Second, the acquisition time of the current SWIP microscope is around 3 minutes per frame, limited by the 2 kHz excitation laser repetition rate. Combining a higher-repetition-rate excitation laser with galvo scanning, the imaging speed of SWIP can be improved. Third, SWIP has shown good performance in imaging through a homogeneous scattering phantom but encounters image degradation at hundreds-of-micrometers deep in the tissue. We attribute such degradation to tissue-induced aberration which inevitably distorts the laser focus. By implementing adaptive optics for aberration correction [153], SWIP can reach even deeper. Lastly, we envision that SWIP microscopy can be upgraded into SWIP-OCT for high-speed volumetric vibrational imaging of organoids and tissues.

5 CHAPTER FIVE – OUTLOOK

Since its invention in the 2000s, the field of advanced vibrational microscopy has grown rapidly in both instrumentation and application. Because of its high-speed, high-resolution label-free chemical imaging capability, advanced vibrational microscopy has demonstrated tremendous potential for clinical applications. Despite significant progress, a definitive clinical function has yet to be identified that would compel medical professionals to embrace this new technique.

In my opinion, one potential direction to establish vibrational microscopy as a standard of care is in-vivo, in-situ fingerprinting imaging on patients. The unique label-free chemical fingerprinting ability of the advanced vibrational microscopy has the maximum value when applied live subjects, especially human. The development of CRS endoscopes and handheld devices has been aimed at enabling such applications. To bring these devices into hospital, a robust and versatile fiber laser-based system is essential. The work presented in the chapter two and three of this dissertation work contributed to this need.

On the other hand, the shallow imaging depth of CRS constraints its ability to capture comprehensive diagnostic information. The imaging depth of CRS is limited by both the tissue scattering and the principle of the modality. Therefore, in chapter four, we developed a new technique, SWIP, to address the problem. We believe these innovations in instrumentation can broaden the application scope of advanced vibrational microscopy and bring the technique closer to the clinical practice.

BIBLIOGRAPHY

[1] W. W. Coblentz, *Investigations of infra-red spectra* (Carnegie Institution of Washington publication; 35; 65; 97; no. 35, 65, 97). Washington, D.C.: Carnegie institution of Washington (in English), 1908.

[2] M. J. Baker *et al.*, "Using Fourier transform IR spectroscopy to analyze biological materials," *Nature Protocols,* vol. 9, no. 8, pp. 1771–1791, Aug 2014, doi: 10.1038/nprot.2014.110.

[3] G. Steiner and E. Koch, "Trends in Fourier transform infrared spectroscopic imaging," *Analytical and Bioanalytical Chemistry,* vol. 394, no. 3, pp. 671–678, Jun 2009, doi: 10.1007/s00216-009-2737-5.

[4] D. Zhang, C. Li, C. Zhang, M. N. Slipchenko, G. Eakins, and J.-X. Cheng, "Depth-resolved mid-infrared photothermal imaging of living cells and organisms with submicrometer spatial resolution," *Science Advances,* vol. 2, no. 9, p. e1600521, 2016, doi: 10.1126/sciadv.1600521.

[5] C. V. Raman and K. S. Krishnan, "A New Type of Secondary Radiation," *Nature,* vol. 121, no. 3048, pp. 501–502, 1928/03/01 1928, doi: 10.1038/121501c0.

[6] G. Pezzotti, "Raman spectroscopy in cell biology and microbiology," *Journal of Raman Spectroscopy,* vol. 52, no. 12, pp. 2348–2443, 2021/12/01 2021, doi: https://doi.org/10.1002/jrs.6204.

[7] A. F. Palonpon *et al.*, "Raman and SERS microscopy for molecular imaging of live cells," *Nature Protocols,* vol. 8, no. 4, pp. 677–692, 2013/04/01 2013, doi: 10.1038/nprot.2013.030.

[8] J. X. Cheng and X. S. Xie, "Vibrational spectroscopic imaging of living systems: An emerging platform for biology and medicine," *Science,* vol. 350, no. 6264, p. aaa8870, Nov 27 2015, doi: 10.1126/science.aaa8870.

[9] H. W. Wang *et al.*, "Label-free bond-selective imaging by listening to vibrationally excited molecules," *Physical Review Letters,* vol. 106, no. 23, p. 238106, Jun 10 2011, doi: 10.1103/PhysRevLett.106.238106.

[10] V. Raghunathan, Y. Han, O. Korth, N.-H. Ge, and E. O. Potma, "Rapid vibrational imaging with sum frequency generation microscopy," *Optics Letters,* vol. 36, no. 19, pp. 3891–3893, 2011/10/01 2011, doi: 10.1364/OL.36.003891.

[11] A. M. Hanninen, R. C. Prince, R. Ramos, M. V. Plikus, and E. O. Potma, "High-resolution infrared imaging of biological samples with third-order sum-frequency

generation microscopy," *Biomedical Optics Express,* vol. 9, no. 10, pp. 4807–4817, Oct 1 2018, doi: 10.1364/BOE.9.004807.

[12] C. H. Camp Jr and M. T. Cicerone, "Chemically sensitive bioimaging with coherent Raman scattering," *Nature Photonics,* vol. 9, no. 5, pp. 295–305, 2015, doi: 10.1038/nphoton.2015.60.

[13] E. M. Vartiainen, "Phase retrieval approach for coherent anti-Stokes Raman scattering spectrum analysis," *Journal of the Optical Society of America. B, Optical Physics,* vol. 9, no. 8, 1992, doi: 10.1364/josab.9.001209.

[14] C. W. Freudiger *et al.*, "Label-Free Biomedical Imaging with High Sensitivity by Stimulated Raman Scattering Microscopy," *Science,* vol. 322, no. 5909, pp. 1857–1861, 2008, doi: 10.1126/science.1165758.

[15] D. Zhang, M. N. Slipchenko, D. E. Leaird, A. M. Weiner, and J. X. Cheng, "Spectrally modulated stimulated Raman scattering imaging with an angle-to-wavelength pulse shaper," *Optics Express,* vol. 21, no. 11, pp. 13864–13874, Jun 3 2013, doi: 10.1364/OE.21.013864.

[16] D. Zhang, C. Li, C. Zhang, N. Slipchenko Mikhail, G. Eakins, and J.-X. Cheng, "Depth-resolved mid-infrared photothermal imaging of living cells and organisms with submicrometer spatial resolution," *Science Advances,* vol. 2, no. 9, p. e1600521, 2016, doi: 10.1126/sciadv.1600521.

[17] H. He *et al.*, "Mapping enzyme activity in living systems by real-time mid-infrared photothermal imaging of nitrile chameleons," *Nature Methods,* vol. 21, no. 2, pp. 342–352, 2024/02/01 2024, doi: 10.1038/s41592-023-02137-x.

[18] L. Wei and W. Min, "Electronic Preresonance Stimulated Raman Scattering Microscopy," *The Journal of Physical Chemistry Letters,* vol. 9, no. 15, pp. 4294–4301, 2018/08/02 2018, doi: 10.1021/acs.jpclett.8b00204.

[19] H. He *et al.*, "Mapping enzyme activity in living systems by real-time mid-infrared photothermal imaging of nitrile chameleons," *Nature Methods,* vol. 21, pp. 342–352, Jan 8 2024, doi: 10.1038/s41592-023-02137-x

[20] Q. Xia *et al.*, "Click-free imaging of carbohydrate trafficking in live cells using an azido photothermal probe," *Science Advances,* vol. 10, no. 34, p. eadq0294, doi: 10.1126/sciadv.adq0294.

[21] Q. Xia *et al.*, "Single virus fingerprinting by widefield interferometric defocus-enhanced mid-infrared photothermal microscopy," *Nature Communications,* vol. 14, no. 1, p. 6655, 2023/10/20 2023, doi: 10.1038/s41467-023-42439-4.

[22] F. Hu, L. Shi, and W. Min, "Biological imaging of chemical bonds by stimulated Raman scattering microscopy," *Nature Methods,* vol. 16, no. 9, pp. 830–842, Sep 2019, doi: 10.1038/s41592-019-0538-0.

[23] Y. Bai, J. Yin, and J.-X. Cheng, "Bond-selective imaging by optically sensing the mid-infrared photothermal effect," *Science Advances,* vol. 7, no. 20, p. eabg1559, 2021, doi: 10.1126/sciadv.abg1559.

[24] M. Ji *et al.*, "Detection of human brain tumor infiltration with quantitative stimulated Raman scattering microscopy," *Science Translational Medicine,* vol. 7, no. 309, p. 309ra163, 2015, doi: 10.1126/scitranslmed.aab0195.

[25] D. A. Orringer *et al.*, "Rapid intraoperative histology of unprocessed surgical specimens via fibre-laser-based stimulated Raman scattering microscopy," *Nature Biomedical Engineering,* vol. 1, article 0027, 2017, doi: 10.1038/s41551-016-0027

[26] T. C. Hollon *et al.*, "Near real-time intraoperative brain tumor diagnosis using stimulated Raman histology and deep neural networks," *Nature Medicine,* vol. 26, no. 1, pp. 52–58, Jan 2020, doi: 10.1038/s41591-019-0715-9.

[27] M. T. Cicerone and C. H. Camp, "Histological coherent Raman imaging: a prognostic review," *Analyst,* vol. 143, no. 1, pp. 33–59, Dec 18 2017, doi: 10.1039/c7an01266g.

[28] J. Gala de Pablo, M. Lindley, K. Hiramatsu, and K. Goda, "High-Throughput Raman Flow Cytometry and Beyond," *Accounts of Chemical Research,* vol. 54, no. 9, pp. 2132–2143, 2021/05/04 2021, doi: 10.1021/acs.accounts.1c00001.

[29] Y. Suzuki *et al.*, "Label-free chemical imaging flow cytometry by high-speed multicolor stimulated Raman scattering," *Proceedings of the National Academy of Sciences of the United States of America,* vol. 116, no. 32, pp. 15842–15848, Aug 6 2019, doi: 10.1073/pnas.1902322116.

[30] K. Hiramatsu *et al.*, "High-throughput label-free molecular fingerprinting flow cytometry," *Science Advances,* vol. 5, no. 1, p. eaau0241, doi: 10.1126/sciadv.aau0241.

[31] K. C. Huang, J. Li, C. Zhang, Y. Tan, and J. X. Cheng, "Multiplex Stimulated Raman Scattering Imaging Cytometry Reveals Lipid-Rich Protrusions in Cancer Cells under Stress Condition," *iScience,* vol. 23, no. 3, p. 100953, Mar 27 2020, doi: 10.1016/j.isci.2020.100953.

[32] J. C. H. Camp, S. Yegnanarayanan, A. A. Eftekhar, and A. Adibi, "Label-free flow cytometry using multiplex coherent anti-Stokes Raman scattering (MCARS) for the

analysis of biological specimens," *Optics Letters,* vol. 36, no. 12, pp. 2309–2311, 2011/06/15 2011, doi: 10.1364/OL.36.002309.

[33] W. Hong *et al.*, "Antibiotic Susceptibility Determination within One Cell Cycle at Single-Bacterium Level by Stimulated Raman Metabolic Imaging," *Analytical Chemistry,* vol. 90, no. 6, pp. 3737–3743, Mar 20 2018, doi: 10.1021/acs.analchem.7b03382.

[34] M. Zhang *et al.*, "Rapid Determination of Antimicrobial Susceptibility by Stimulated Raman Scattering Imaging of D2O Metabolic Incorporation in a Single Bacterium," *Advanced Science (Weinheim, Germany),* vol. 7, no. 19, p. 2001452, Oct 2020, doi: 10.1002/advs.202001452.

[35] B. G. Saar, L. R. Contreras-Rojas, X. S. Xie, and R. H. Guy, "Imaging Drug Delivery to Skin with Stimulated Raman Scattering Microscopy," *Molecular Pharmaceutics,* vol. 8, no. 3, pp. 969–975, 2011/06/06 2011, doi: 10.1021/mp200122w.

[36] A. Feizpour, T. Marstrand, L. Bastholm, S. Eirefelt, and C. L. Evans, "Label-Free Quantification of Pharmacokinetics in Skin with Stimulated Raman Scattering Microscopy and Deep Learning," *Journal of Investigative Dermatology,* vol. 141, no. 2, pp. 395–403, 2021/02/01/ 2021, doi: https://doi.org/10.1016/j.jid.2020.06.027.

[37] P. Zarmpi *et al.*, "Evaluation of chemical disposition in skin by stimulated Raman scattering microscopy," *Journal of Controlled Release,* vol. 368, pp. 797–807, 2024/04/01/ 2024, doi: https://doi.org/10.1016/j.jconrel.2024.02.011.

[38] C.-S. Liao *et al.*, "In Vivo and in Situ Spectroscopic Imaging by a Handheld Stimulated Raman Scattering Microscope," *ACS Photonics,* vol. 5, no. 3, pp. 947–954, 2017, doi: 10.1021/acsphotonics.7b01214.

[39] A. Lombardini *et al.*, "High-resolution multimodal flexible coherent Raman endoscope," *Light, Science & Applications,* vol. 7, p. 10, 2018, doi: 10.1038/s41377-018-0003-3.

[40] M. Schnell *et al.*, "All-digital histopathology by infrared-optical hybrid microscopy," *Proceedings of the National Academy of Sciences of the United States of America,* vol. 117, no. 7, pp. 3388–3396, Feb 18 2020, doi: 10.1073/pnas.1912400117.

[41] Z. Guo, Y. Bai, M. Zhang, L. Lan, and J.-X. Cheng, "High-Throughput Antimicrobial Susceptibility Testing of Escherichia coli by Wide-Field Mid-Infrared Photothermal Imaging of Protein Synthesis," *Analytical Chemistry,* vol. 95, no. 4, pp. 2238–2244, 2023/01/31 2023, doi: 10.1021/acs.analchem.2c03683.

[42] Y. Zhang *et al.*, "Vibrational Spectroscopic Detection of a Single Virus by Mid-Infrared Photothermal Microscopy," *Analytical Chemistry,* Feb 17 2021, doi: 10.1021/acs.analchem.0c05333

[43] C. W. Freudiger, W. Yang, G. R. Holtom, N. Peyghambarian, X. S. Xie, and K. Q. Kieu, "Stimulated Raman Scattering Microscopy with a Robust Fibre Laser Source," *Nature Photonics,* vol. 8, no. 2, pp. 153–159, Feb 1 2014, doi: 10.1038/nphoton.2013.360.

[44] S. Karpf, M. Eibl, W. Wieser, T. Klein, and R. Huber, "A Time-Encoded Technique for fibre-based hyperspectral broadband stimulated Raman microscopy," *Nature Communications,* vol. 6, p. 6784, Apr 17 2015, doi: 10.1038/ncomms7784.

[45] T. Gottschall, T. Meyer, C. Jauregui *et al.* "All-fiber optical parametric oscillator for bio-medical imaging applications," In C.A. Robin and I. Hartl (eds.) *Fiber Lasers XIV: Technology and Systems*, Proceedings of SPIE, vol. 10083, article 100831E, 2017. https://doi.org/10.1117/12.2250484

[46] H. Ni *et al.*, "Multiwindow SRS Imaging Using a Rapid Widely Tunable Fiber Laser," *Analytical Chemistry,* vol. 93, no. 47, pp. 15703–15711, 2021/11/30, doi: 10.1021/acs.analchem.1c03604.

[47] Y. Wakisaka *et al.*, "Probing the metabolic heterogeneity of live Euglena gracilis with stimulated Raman scattering microscopy," *Nature Microbiology,* vol. 1, no. 10, p. 16124, Aug 1 2016, doi: 10.1038/nmicrobiol.2016.124.

[48] K. S. Shin, M. Laohajaratsang, S. Men, B. Figueroa, S. M. Dintzis, and D. Fu, "Quantitative chemical imaging of breast calcifications in association with neoplastic processes," *Theranostics,* vol. 10, no. 13, pp. 5865–5878, 2020, doi: 10.7150/thno.43325.

[49] L. Zhang *et al.*, "Spectral tracing of deuterium for imaging glucose metabolism," *Nature Biomedical Engineering,* vol. 3, no. 5, pp. 402–413, May 2019, doi: 10.1038/s41551-019-0393-4.

[50] M. Ji *et al.*, "Label-free imaging of amyloid plaques in Alzheimer's disease with stimulated Raman scattering microscopy," *Science Advances,* vol. 4, no. 11, p. eaat7715, Nov 2018, doi: 10.1126/sciadv.aat7715.

[51] D. Lee, J. Du, R. Yu, Y. Su, J. R. Heath, and L. Wei, "Visualizing Subcellular Enrichment of Glycogen in Live Cancer Cells by Stimulated Raman Scattering," *Analytical Chemistry,* vol. 92, no. 19, pp. 13182–13191, Oct 6 2020, doi: 10.1021/acs.analchem.0c02348.

[52] H. Lin *et al.*, "Microsecond fingerprint stimulated Raman spectroscopic imaging by ultrafast tuning and spatial-spectral learning," *Nature Communications,* vol. 12, no. 1, 2021, doi: 10.1038/s41467-021-23202-z.

[53] C.-S. Liao *et al.*, "Stimulated Raman spectroscopic imaging by microsecond delay-line tuning," *Optica,* vol. 3, no. 12, 2016, doi: 10.1364/optica.3.001377.

[54] B. Figueroa *et al.*, "Broadband hyperspectral stimulated Raman scattering microscopy with a parabolic fiber amplifier source," *Biomedical Optics Express,* vol. 9, no. 12, pp. 6116–6131, Dec 2018, doi: 10.1364/boe.9.006116.

[55] S. P. Laptenok *et al.*, "Fingerprint-to-CH stretch continuously tunable high spectral resolution stimulated Raman scattering microscope," *Journal of Biophotonics,* vol. 12, no. 9, p. e201900028, Sep 2019, doi: 10.1002/jbio.201900028.

[56] D. Zhang, P. Wang, M. N. Slipchenko, D. Ben-Amotz, A. M. Weiner, and J. X. Cheng, "Quantitative vibrational imaging by hyperspectral stimulated Raman scattering microscopy and multivariate curve resolution analysis," *Analytical Chemistry,* vol. 85, no. 1, pp. 98–106, Jan 2 2013, doi: 10.1021/ac3019119.

[57] Y. Ozeki *et al.*, "Stimulated Raman scattering microscope with shot noise limited sensitivity using subharmonically synchronized laser pulses," *Optics Express,* vol. 18, no. 13, pp. 13708–19, Jun 21 2010, doi: 10.1364/OE.18.013708

[58] K. Wang, C. W. Freudiger, J. H. Lee, B. G. Saar, X. S. Xie, and C. Xu, "Synchronized time-lens source for coherent Raman scattering microscopy," *Optics Express,* vol. 18, no. 23, pp. 24019–24024, 2010/11/08 2010, doi: 10.1364/OE.18.024019.

[59] K. Nose *et al.*, "Sensitivity enhancement of fiber-laser-based stimulated Raman scattering microscopy by collinear balanced detection technique," *Optics Express,* vol. 20, no. 13, pp. 13958–13965, 2012/06/18 2012, doi: 10.1364/OE.20.013958.

[60] C. Kong *et al.*, "High-contrast, fast chemical imaging by coherent Raman scattering using a self-synchronized two-colour fibre laser," *Light, Science & Applications,* vol. 9, p. 25, 2020, doi: 10.1038/s41377-020-0259-2.

[61] A. Gambetta *et al.*, "Fiber-format stimulated-Raman-scattering microscopy from a single laser oscillator," *Optics Letters,* vol. 35, no. 2, pp. 226–228, 2010/01/15 2010, doi: 10.1364/OL.35.000226.

[62] F. Crisafi, V. Kumar, A. Perri, M. Marangoni, G. Cerullo, and D. Polli, "Multimodal nonlinear microscope based on a compact fiber-format laser source," *Spectrochimica Acta. Part A, Molecular and Biomolecular Spectroscopy,* vol. 188, pp. 135–140, Jan 5 2018, doi: 10.1016/j.saa.2017.06.055

[63] M. Brinkmann, A. Fast, T. Hellwig, I. Pence, C. L. Evans, and C. Fallnich, "Portable all-fiber dual-output widely tunable light source for coherent Raman imaging," *Biomedical Optics Express,* vol. 10, no. 9, pp. 4437–4449, Sep 1 2019, doi: 10.1364/BOE.10.004437.

[64] T. Würthwein, M. Brinkmann, T. Hellwig, K. Wallmeier, and C. Fallnich, "High-sensitivity frequency modulation CARS with a compact and fast tunable fiber-based light source," *Optics Letters,* vol. 46, no. 15, pp. 3544–3547, 2021/08/01 2021, doi: 10.1364/OL.425578.

[65] F. Crisafi, V. Kumar, T. Scopigno, M. Marangoni, G. Cerullo, and D. Polli, "In-line balanced detection stimulated Raman scattering microscopy," *Scientific Reports,* vol. 7, no. 1, p. 10745, Sep 6 2017, doi: 10.1038/s41598-017-09839-1.

[66] Y. Choi, S. Lim, J. W. Shim, B. Chon, J. M. Lim, and M. Cho, "Shot-Noise-Limited Two-Color Stimulated Raman Scattering Microscopy with a Balanced Detection Scheme," *Journal of Physical Chemistry. B,* vol. 124, no. 13, pp. 2591–2599, Apr 2 2020, doi: 10.1021/acs.jpcb.0c01065.

[67] X. Audier, S. Heuke, P. Volz, I. Rimke, and H. Rigneault, "Noise in stimulated Raman scattering measurement: From basics to practice," *APL Photonics,* vol. 5, no. 1, 2020, doi: 10.1063/1.5129212.

[68] D. Berry *et al.*, "Tracking heavy water (D2O) incorporation for identifying and sorting active microbial cells," *Proceedings of the National Academy of Sciences of the United States of America,* vol. 112, no. 2, pp. E194–203, Jan 13 2015, doi: 10.1073/pnas.1420406112.

[69] V. J. Valdes, A. Athie, L. S. Salinas, R. E. Navarro, and L. Vaca, "CUP-1 is a novel protein involved in dietary cholesterol uptake in Caenorhabditis elegans," *PLoS One,* vol. 7, no. 3, p. e33962, 2012, doi: 10.1371/journal.pone.0033962.

[70] Y. Kumamoto, Y. Harada, T. Takamatsu, and H. Tanaka, "Label-free Molecular Imaging and Analysis by Raman Spectroscopy," *Acta Histochemica et Cytochemica,* vol. 51, no. 3, pp. 101–110, 2018, doi: 10.1267/ahc.18019.

[71] C. H. Camp, Jr. *et al.*, "High-Speed Coherent Raman Fingerprint Imaging of Biological Tissues," *Nature Photonics,* vol. 8, pp. 627–634, 2014, doi: 10.1038/nphoton.2014.145.

[72] H. Lin, C. S. Liao, P. Wang, N. Kong, and J. X. Cheng, "Spectroscopic stimulated Raman scattering imaging of highly dynamic specimens through matrix completion," *Light, Science & Applications,* vol. 7, p. 17179, 2018, doi: 10.1038/lsa.2017.179.

[73] T. Würthwein *et al.*, "Multi-color stimulated Raman scattering with a frame-to-frame wavelength-tunable fiber-based light source," arXiv:2108.00782. [Online]. Available: https://ui.adsabs.harvard.edu/abs/2021arXiv210800782W

[74] H. Ni *et al.*, "High-content stimulated Raman histology of human breast cancer," *Theranostics,* vol. 14, no. 4, pp. 1361–1370, 2024, doi: 10.7150/thno.90336

[75] H. Sung *et al.*, "Global Cancer Statistics 2020: GLOBOCAN Estimates of Incidence and Mortality Worldwide for 36 Cancers in 185 Countries," *CA: A Cancer Journal for Clinicians,* vol. 71, no. 3, pp. 209–249, May 2021, doi: 10.3322/caac.21660

[76] A. N. Giaquinto *et al.*, "Breast Cancer Statistics, 2022," *CA: A Cancer Journal for Clinicians,* vol. 72, no. 6, pp. 524–541, Nov 2022, doi: 10.3322/caac.21754

[77] C. van Dooijeweert *et al.*, "Significant inter- and intra-laboratory variation in grading of invasive breast cancer: A nationwide study of 33,043 patients in the Netherlands," *International Journal of Cancer,* vol. 146, no. 3, pp. 769–780, Feb 1 2020, doi: 10.1002/ijc.32330

[78] I. Holzer, A. Farr, Y. Tan, C. Deutschmann, C. Leser, and C. F. Singer, "Receptor Discordance of Metastatic Breast Cancer Depending on the Molecular Subtype," *Breast Care (Basel),* vol. 15, no. 6, pp. 648–654, Dec 2020, doi: 10.1159/000506464

[79] D. Lazaro-Pacheco, A. M. Shaaban, S. Rehman, and I. Rehman, "Raman spectroscopy of breast cancer," *Applied Spectroscopy Reviews,* vol. 55, no. 6, pp. 439–475, 2020/07/02 2020, doi: 10.1080/05704928.2019.1601105

[80] S. Cui, S. Zhang, and S. Yue, "Raman Spectroscopy and Imaging for Cancer Diagnosis," *Journal of Healthcare Engineering,* vol. 2018, p. 8619342, 2018, doi: 10.1155/2018/8619342

[81] D. Zhang, P. Wang, M. N. Slipchenko, and J. X. Cheng, "Fast vibrational imaging of single cells and tissues by stimulated Raman scattering microscopy," *Accounts of Chemical Research,* vol. 47, no. 8, pp. 2282–90, Aug 19 2014, doi: 10.1021/ar400331q

[82] M. Ji *et al.*, "Rapid, label-free detection of brain tumors with stimulated Raman scattering microscopy," *Science Translational Medicine,* vol. 5, no. 201, p. 201ra119, Sep 4 2013, doi: 10.1126/scitranslmed.3005954

[83] Z. Liu *et al.*, "Instant diagnosis of gastroscopic biopsy via deep-learned single-shot femtosecond stimulated Raman histology," *Nature Communications,* vol. 13, no. 1, p. 4050, Jul 13 2022, doi: 10.1038/s41467-022-31339-8

[84] Y. Yang *et al.*, "Histological diagnosis of unprocessed breast core-needle biopsy via stimulated Raman scattering microscopy and multi-instance learning," *Theranostics,* vol. 13, no. 4, pp. 1342–1354, 2023, doi: 10.7150/thno.81784.

[85] J. Ao *et al.*, "Stimulated Raman Scattering Microscopy Enables Gleason Scoring of Prostate Core Needle Biopsy by a Convolutional Neural Network," *Cancer Research,* vol. 83, no. 4, pp. 641–651, Feb 15 2023, doi: 10.1158/0008-5472.CAN-22-2146.

[86] Y. Yang *et al.*, "Microcalcification-Based Tumor Malignancy Evaluation in Fresh Breast Biopsies with Hyperspectral Stimulated Raman Scattering," *Analytical Chemistry,* vol. 93, no. 15, pp. 6223–6231, Apr 20 2021, doi: 10.1021/acs.analchem.1c00522.

[87] D. Fu, G. Holtom, C. Freudiger, X. Zhang, and X. S. Xie, "Hyperspectral imaging with stimulated Raman scattering by chirped femtosecond lasers," *Journal of Physical Chemistry. B,* vol. 117, no. 16, pp. 4634–40, Apr 25 2013, doi: 10.1021/jp308938t.

[88] A. C. S. Talari, S. Rehman, and I. U. Rehman, "Advancing cancer diagnostics with artificial intelligence and spectroscopy: identifying chemical changes associated with breast cancer," *Expert Review of Molecular Diagnostics,* vol. 19, no. 10, pp. 929–940, Oct 2019, doi: 10.1080/14737159.2019.1659727.

[89] A. S. Melitto, V. E. A. Arias, J. Y. Shida, L. H. Gebrim, and L. Silveira, Jr., "Diagnosing molecular subtypes of breast cancer by means of Raman spectroscopy," *Lasers in Surgery and Medicine,* vol. 54, no. 8, pp. 1143–1156, Oct 2022, doi: 10.1002/lsm.23580.

[90] A. S. Haka, K. E. Shafer-Peltier, M. Fitzmaurice, J. Crowe, R. R. Dasari, and M. S. Feld, "Diagnosing breast cancer by using Raman spectroscopy," *Proceedings of the National Academy of Sciences of the United States of America,* vol. 102, no. 35, p. 12371, 2005, doi: 10.1073/pnas.0501390102.

[91] R. de Andrade Natal, J. Adur, C. L. Cesar, and J. Vassallo, "Tumor extracellular matrix: lessons from the second-harmonic generation microscopy," *Surgical and Experimental Pathology,* vol. 4, no. 1, 2021, doi: 10.1186/s42047-021-00089-0.

[92] H. Abramczyk and B. Brozek-Pluska, "New look inside human breast ducts with Raman imaging. Raman candidates as diagnostic markers for breast cancer prognosis: Mammaglobin, palmitic acid and sphingomyelin," *Analytica Chimica Acta,* vol. 909, pp. 91–100, Feb 25 2016, doi: 10.1016/j.aca.2015.12.038.

[93] M. P. M. Marques, A. L. M. Batista de Carvalho, A. P. Mamede, A. Dopplapudi, V. Garcia Sakai, and L. A. E. Batista de Carvalho, "Role of intracellular water in

the normal-to-cancer transition in human cells-insights from quasi-elastic neutron scattering," *Structural Dynamics,* vol. 7, no. 5, p. 054701, Sep 2020, doi: 10.1063/4.0000021.

[94] Y. Tan, H. Lin, and J.-X. Cheng, "Profiling single cancer cell metabolism via high-content SRS imaging with chemical sparsity," *Science Advances,* vol. 9, no. 33, p. eadg6061, doi: 10.1126/sciadv.adg6061.

[95] C. S. Liao, J. H. Choi, D. Zhang, S. H. Chan, and J. X. Cheng, "Denoising Stimulated Raman Spectroscopic Images by Total Variation Minimization," *Journal of Physical Chemistry. C, Nanomaterials and Interfaces,* vol. 119, no. 33, pp. 19397–19403, Aug 20 2015, doi: 10.1021/acs.jpcc.5b06980.

[96] A. M. Wright, A. A. Howard, J. C. Howard, G. S. Tschumper, and N. I. Hammer, "Charge transfer and blue shifting of vibrational frequencies in a hydrogen bond acceptor," *Journal of Physical Chemistry. A,* vol. 117, no. 26, pp. 5435–46, Jul 3 2013, doi: 10.1021/jp401642b.

[97] N. C. Maiti, M. M. Apetri, M. G. Zagorski, P. R. Carey, and V. E. Anderson, "Raman Spectroscopic Characterization of Secondary Structure in Natively Unfolded Proteins: α-Synuclein," *Journal of the American Chemical Society,* vol. 126, no. 8, pp. 2399–2408, 2004/03/03 2004, doi: 10.1021/ja0356176.

[98] V. Chajes, T. Niyongabo, M. Lanson, A. Fignon, C. Couet, and P. Bougnoux, "Fatty-acid composition of breast and iliac adipose tissue in breast-cancer patients," *International Journal of Cancer,* vol. 50, no. 3, pp. 405–8, Feb 1 1992, doi: 10.1002/ijc.2910500314.

[99] C. Nieva, M. Marro, N. Santana-Codina, S. Rao, D. Petrov, and A. Sierra, "The lipid phenotype of breast cancer cells characterized by Raman microspectroscopy: towards a stratification of malignancy," *PLoS One,* vol. 7, no. 10, p. e46456, 2012, doi: 10.1371/journal.pone.0046456.

[100] S. Ranjit *et al.*, "Imaging Fibrosis and Separating Collagens using Second Harmonic Generation and Phasor Approach to Fluorescence Lifetime Imaging," *Scientific Reports,* vol. 5, p. 13378, Aug 21 2015, doi: 10.1038/srep13378.

[101] T. T. Le, I. M. Langohr, M. J. Locker, M. Sturek, and J. X. Cheng, "Label-free molecular imaging of atherosclerotic lesions using multimodal nonlinear optical microscopy," *Journal of Biomedical Optics,* vol. 12, no. 5, p. 054007, Sep–Oct 2007, doi: 10.1117/1.2795437.

[102] Y. Vaidya, P. Vaidya, and T. Vaidya, "Ductal Carcinoma In Situ of the Breast," *Indian Journal of Surgery,* vol. 77, no. 2, pp. 141–6, Apr 2015, doi: 10.1007/s12262-013-0987-0.

[103] S. Bodis, K. P. Siziopikou, S. J. Schnitt, J. R. Harris, and D. E. Fisher, "Extensive apoptosis in ductal carcinoma in situ of the breast," *Cancer,* vol. 77, no. 9, pp. 1831–1835, 1996/05/01 https://doi.org/10.1002/(SICI)1097-0142(19960501)77:9<1831::AID-CNCR11>3.0.CO;2-0

[104] K. Czamara, K. Majzner, M. Z. Pacia, K. Kochan, A. Kaczor, and M. Baranska, "Raman spectroscopy of lipids: a review," *Journal of Raman Spectroscopy,* vol. 46, no. 1, pp. 4–20, 2015, doi: 10.1002/jrs.4607.

[105] H. Ni *et al.*, "Millimetre-deep micrometre-resolution vibrational imaging by shortwave infrared photothermal microscopy," *Nature Photonics,* 2024, doi: 10.1038/s41566-024-01463-6.

[106] J. Kim, B. K. Koo, and J. A. Knoblich, "Human organoids: model systems for human biology and medicine," *Nature Reviews. Molecular Cell Biology,* vol. 21, no. 10, pp. 571–584, Oct 2020, doi: 10.1038/s41580-020-0259-3.

[107] A. H. Hill, B. Manifold, and D. Fu, "Tissue imaging depth limit of stimulated Raman scattering microscopy," *Biomedical Optics Express,* vol. 11, no. 2, pp. 762–774, Feb 1 2020, doi: 10.1364/BOE.382396.

[108] R. Esposito, G. Scherillo, M. Pannico, P. Musto, S. De Nicola, and G. Mensitieri, "Depth profiles in confocal optical microscopy: a simulation approach based on the second Rayleigh-Sommerfeld diffraction integral," *Optics Express,* vol. 24, no. 12, pp. 12565–76, Jun 13 2016, doi: 10.1364/OE.24.012565.

[109] S. Mosca *et al.*, "Spatially Offset Raman Spectroscopy-How Deep?," *Analytical Chemistry,* vol. 93, no. 17, pp. 6755–6762, May 4 2021, doi: 10.1021/acs.analchem.1c00490.

[110] S. Mosca, C. Conti, N. Stone, and P. Matousek, "Spatially offset Raman spectroscopy," *Nature Reviews. Methods Primers,* vol. 1, no. 1, p. 21, 2021/03/11 2021, doi: 10.1038/s43586-021-00019-0.

[111] M. V. Schulmerich *et al.*, "Noninvasive Raman tomographic imaging of canine bone tissue," *Journal of Biomedical Optics,* vol. 13, no. 2, p. 020506, Mar–Apr 2008, doi: 10.1117/1.2904940.

[112] J.-L. H. Demers, S. C. Davis, B. W. Pogue, and M. D. Morris, "Multichannel diffuse optical Raman tomography for bone characterization in vivo: a phantom study," *Biomedical Optics Express,* vol. 3, no. 9, pp. 2299–2305, 2012/09/01 2012, doi: 10.1364/BOE.3.002299.

[113] J. L. Demers, F. W. Esmonde-White, K. A. Esmonde-White, M. D. Morris, and B. W. Pogue, "Next-generation Raman tomography instrument for non-invasive in

vivo bone imaging," *Biomedical Optics Express,* vol. 6, no. 3, pp. 793–806, Mar 1 2015, doi: 10.1364/BOE.6.000793

[114] R. H. Wilson, K. P. Nadeau, F. B. Jaworski, B. J. Tromberg, and A. J. Durkin, "Review of short-wave infrared spectroscopy and imaging methods for biological tissue characterization," *Journal of Biomedical Optics,* vol. 20, no. 3, p. 030901, Mar 2015, doi: 10.1117/1.JBO.20.3.030901.

[115] N. G. Horton *et al.*, "In vivo three-photon microscopy of subcortical structures within an intact mouse brain," *Nature Photonics,* vol. 7, no. 3, Mar 1 2013, doi: 10.1038/nphoton.2012.336.

[116] P. Wang, J. R. Rajian, and J. X. Cheng, "Spectroscopic Imaging of Deep Tissue through Photoacoustic Detection of Molecular Vibration," *Journal of Physical Chemistry Letters,* vol. 4, no. 13, pp. 2177–2185, Jul 3 2013, doi: 10.1021/jz400559a.

[117] Y. Zhao *et al.*, "Shortwave-infrared meso-patterned imaging enables label-free mapping of tissue water and lipid content," *Nature Communications,* vol. 11, no. 1, p. 5355, Oct 23 2020, doi: 10.1038/s41467-020-19128-7.

[118] L. V. Wang and J. Yao, "A practical guide to photoacoustic tomography in the life sciences," *Nature Methods,* vol. 13, no. 8, pp. 627–38, Jul 28 2016, doi: 10.1038/nmeth.3925.

[119] L. V. Wang, *Photoacoustic imaging and spectroscopy*. CRC press, 2017.

[120] P. Hajireza, W. Shi, K. Bell, R. J. Paproski, and R. J. Zemp, "Non-interferometric photoacoustic remote sensing microscopy," *Light, Science & Applications,* vol. 6, no. 6, p. e16278, Jun 2017, doi: 10.1038/lsa.2016.278.

[121] P. H. Reza, K. Bell, W. Shi, J. Shapiro, and R. J. Zemp, "Deep non-contact photoacoustic initial pressure imaging," *Optica,* vol. 5, no. 7, 2018, doi: 10.1364/optica.5.000814.

[122] K. Bell, L. Mukhangaliyeva, L. Khalili, and P. Haji Reza, "Hyperspectral absorption microscopy using photoacoustic remote sensing," *Optics Express,* vol. 29, no. 15, pp. 24338–24348, Jul 19 2021, doi: 10.1364/OE.430403.

[123] G. Hu *et al.*, "Noncontact photoacoustic lipid imaging by remote sensing on first overtone of the C-H bond," *Advanced Photonics Nexus,* vol. 2, no. 02, 2023, doi: 10.1117/1.Apn.2.2.026011

[124] P. Cias, C. Wang, and T. S. Dibble, "Absorption Cross-Sections of the C—H Overtone of Volatile Organic Compounds: 2 Methyl-1,3-Butadiene (Isoprene), 1,3-

Butadiene, and 2,3-Dimethyl-1,3-Butadiene," *Applied Spectroscopy,* vol. 61, no. 2, pp. 230–236, 2007/02/01 2007, doi: 10.1366/000370207779947440.

[125] J. Bai *et al.*, "Sensitivity Analysis of 1,3-Butadiene Monitoring Based on Space-Based Detection in the Infrared Band," *Remote Sensing,* vol. 14, no. 19, 2022, doi: 10.3390/rs14194788.

[126] J. E. Bertie and Z. Lan, "Infrared Intensities of Liquids XX: The Intensity of the OH Stretching Band of Liquid Water Revisited, and the Best Current Values of the Optical Constants of H2O(l) at 25°C between 15,000 and 1 cm−1," *Applied Spectroscopy,* vol. 50, no. 8, pp. 1047–1057, 1996/08/01 1996, doi: 10.1366/0003702963905385.

[127] P. Wang, H. W. Wang, M. Sturek, and J. X. Cheng, "Bond-selective imaging of deep tissue through the optical window between 1600 and 1850 nm," *Journal of Biophotonics,* vol. 5, no. 1, pp. 25–32, Jan 2012, doi: 10.1002/jbio.201100102.

[128] M. Selmke, M. Braun, and F. Cichos, "Photothermal Single-Particle Microscopy: Detection of a Nanolens," *ACS Nano,* vol. 6, no. 3, pp. 2741–2749, 2012/03/27 2012, doi: 10.1021/nn300181h.

[129] D. MacDougall, W. B. Crummett, and et al., "Guidelines for data acquisition and data quality evaluation in environmental chemistry," *Analytical Chemistry,* vol. 52, no. 14, pp. 2242–2249, 1980/12/01 1980, doi: 10.1021/ac50064a004.

[130] Y. Tan *et al.*, "Metabolic reprogramming from glycolysis to fatty acid uptake and beta-oxidation in platinum-resistant cancer cells," *Nature Communications,* vol. 13, no. 1, p. 4554, Aug 5 2022, doi: 10.1038/s41467-022-32101-w.

[131] A. Rose, G. J. Salamo, and R. Gupta, "Photoacoustic deflection spectroscopy: a new specie-specific method for combustion diagnostics," *Applied Optics,* vol. 23, no. 6, pp. 781–784, 1984/03/15 1984, doi: 10.1364/AO.23.000781.

[132] S. Berciaud, D. Lasne, G. A. Blab, L. Cognet, and B. Lounis, "Photothermal heterodyne imaging of individual metallic nanoparticles: Theory versus experiment," *Physical Review B,* vol. 73, no. 4, 2006, doi: 10.1103/PhysRevB.73.045424.

[133] S. Adhikari, P. Spaeth, A. Kar, M. D. Baaske, S. Khatua, and M. Orrit, "Photothermal Microscopy: Imaging the Optical Absorption of Single Nanoparticles and Single Molecules," *ACS Nano,* Nov 20 2020, doi: 10.1021/acsnano.0c07638.

[134] J. Y. Shin, M. A. Shaloski, F. F. Crim, and A. S. Case, "First Evidence of Vibrationally Driven Bimolecular Reactions in Solution: Reactions of Br Atoms

with Dimethylsulfoxide and Methanol," *Journal of Physical Chemistry. B,* vol. 121, no. 11, pp. 2486–2494, Mar 23 2017, doi: 10.1021/acs.jpcb.7b00035.

[135] M. Z. Vardaki and N. Kourkoumelis, "Tissue Phantoms for Biomedical Applications in Raman Spectroscopy: A Review," *Biomedical Engineering and Computational Biology,* vol. 11, p. 1179597220948100, 2020, doi: 10.1177/1179597220948100

[136] T. Ishiguro, H. Ohata, A. Sato, K. Yamawaki, T. Enomoto, and K. Okamoto, "Tumor-derived spheroids: Relevance to cancer stem cells and clinical applications," *Cancer Science,* vol. 108, no. 3, pp. 283–289, Mar 2017, doi: 10.1111/cas.13155

[137] X. Bian, R. Liu, Y. Meng, D. Xing, D. Xu, and Z. Lu, "Lipid metabolism and cancer," *Journal of Experimental Medicine,* vol. 218, no. 1, Jan 4 2021, doi: 10.1084/jem.20201606

[138] S. Kuriu, T. Kadonosono, S. Kizaka-Kondoh, and T. Ishida, "Slicing Spheroids in Microfluidic Devices for Morphological and Immunohistochemical Analysis," *Micromachines (Basel),* vol. 11, no. 5, May 6 2020, doi: 10.3390/mi11050480

[139] M. Wei *et al.*, "Volumetric chemical imaging by clearing-enhanced stimulated Raman scattering microscopy," *Proceedings of the National Academy of Sciences of the United States of America,* vol. 116, no. 14, pp. 6608–6617, Apr 2 2019, doi: 10.1073/pnas.1813044116

[140] S. J. Edwards *et al.*, "High-Resolution Imaging of Tumor Spheroids and Organoids Enabled by Expansion Microscopy," *Frontiers in Molecular Biosciences,* vol. 7, p. 208, 2020, doi: 10.3389/fmolb.2020.00208

[141] F. Pampaloni, N. Ansari, and E. H. Stelzer, "High-resolution deep imaging of live cellular spheroids with light-sheet-based fluorescence microscopy," *Cell and Tissue Research,* vol. 352, no. 1, pp. 161–77, Apr 2013, doi: 10.1007/s00441-013-1589-7

[142] K. Konig, A. Uchugonova, and E. Gorjup, "Multiphoton fluorescence lifetime imaging of 3D-stem cell spheroids during differentiation," *Microscopy Research and Technique,* vol. 74, no. 1, pp. 9–17, Jan 2011, doi: 10.1002/jemt.20866

[143] Y. Yu, P. V. Ramachandran, and M. C. Wang, "Shedding new light on lipid functions with CARS and SRS microscopy," *Biochimica et Biophysica Acta,* vol. 1841, no. 8, pp. 1120–9, Aug 2014, doi: 10.1016/j.bbalip.2014.02.003

[144] I. Pradas *et al.*, "Lipidomics Reveals a Tissue-Specific Fingerprint," *Frontiers in Physiology,* vol. 9, p. 1165, 2018, doi: 10.3389/fphys.2018.01165

[145] L. Shi, A. A. Fung, and A. Zhou, "Advances in stimulated Raman scattering imaging for tissues and animals," *Quantitative Imaging in Medicine and Surgery,* vol. 11, no. 3, pp. 1078–1101, Mar 2021, doi: 10.21037/qims-20-712.

[146] S. A. Taqi, S. A. Sami, L. B. Sami, and S. A. Zaki, "A review of artifacts in histopathology," *Journal of Oral and Maxillofacial Pathology,* vol. 22, no. 2, p. 279, May–Aug 2018, doi: 10.4103/jomfp.JOMFP_125_15.

[147] Y. Urasaki, C. Zhang, J. X. Cheng, and T. T. Le, "Quantitative Assessment of Liver Steatosis and Affected Pathways with Molecular Imaging and Proteomic Profiling," *Scientific Reports,* vol. 8, no. 1, p. 3606, Feb 26 2018, doi: 10.1038/s41598-018-22082-6.

[148] S. Hu and L. V. Wang, "Optical-resolution photoacoustic microscopy: auscultation of biological systems at the cellular level," *Biophysical Journal,* vol. 105, no. 4, pp. 841–7, Aug 20 2013, doi: 10.1016/j.bpj.2013.07.017.

[149] D. C. Sordillo, L. A. Sordillo, P. P. Sordillo, L. Shi, and R. R. Alfano, "Short wavelength infrared optical windows for evaluation of benign and malignant tissues," *Journal of Biomedical Optics,* vol. 22, no. 4, p. 45002, Apr 1 2017, doi: 10.1117/1.JBO.22.4.045002.

[150] H. J. van Staveren, C. J. M. Moes, J. van Marie, S. A. Prahl, and M. J. C. van Gemert, "Light scattering in lntralipid-10% in the wavelength range of 400–1100 nm," *Applied Optics,* vol. 30, no. 31, pp. 4507–4514, 1991/11/01 1991, doi: 10.1364/AO.30.004507.

[151] M. S. Singh and A. Thomas, "Photoacoustic elastography imaging: a review," *Journal of Biomedical Optics,* vol. 24, no. 4, pp. 1–15, Apr 2019, doi: 10.1117/1.JBO.24.4.040902.

[152] S. Oh *et al.*, "Protein and lipid mass concentration measurement in tissues by stimulated Raman scattering microscopy," *Proceedings of the National Academy of Sciences of the United States of America,* vol. 119, no. 17, p. e2117938119, Apr 26 2022, doi: 10.1073/pnas.2117938119.

[153] L. Streich *et al.*, "High-resolution structural and functional deep brain imaging using adaptive optics three-photon microscopy," *Nature Methods,* vol. 18, no. 10, pp. 1253–1258, Oct 2021, doi: 10.1038/s41592-021-01257-6.

CURRICULUM VITAE

[redacted]

[redacted]

[redacted]

[redacted]